ICFO-INSTITUT DE CIÈNCIES FOTÒNIQUES

&

UPC-UNIVERSITAT POLITÈCNICA DE CATALUNYA

Nanophotonics of ultrathin films and 2D periodic structures: a combined experimental and theoretical study

VAHAGN MKHITARYAN

Thesis Advisor: Prof. Valerio Pruneri
Co-Advisor: Prof. Javier García De Abajo

PhD Thesis - 2017

To my family

Abstract

Photonics is a key enabling technology for many applications ranging from communications to energy and medicine. Its success is largely relying on our capability to appropriately control light in optical devices. To this end, the understanding of light-matter interaction occurring in the devices is a crucial element for finding effective solutions to the challenges posed by the targeted applications.

This thesis is devoted to understand light-matter interaction in periodic nanostructures and ultrathin films and create modelling and design tools for functional optical devices, some of them demonstrated experimentally.

We start by investigating the needed theoretical methods for describing the interaction of light with surface periodic nanostructures. We carry out a comprehensive study of the transmission, reflection and dispersion properties of 2D periodic arrays and their stacks, including, the study of more complex structures as well, such as, defects in periodic lattices, random arrays of scatterers and multicomponent lattices, and the calculation of the local density of electromagnetic states in the array.

We then show how to use the developed theory to design and understand the behaviours of application-specific devices/structures, made of 2D periodic structures and multilayer stack of thin films.

A first device demonstrator consists in periodic arrays of nanoholes performated in a gold film covered with $Ge_2Sb_2Te_5$ (GST), a phase change material layer.We investigate the effect of GST's phase transitions on the transmission resonances of these structures. Wavelength shifts as large as 385 nm are demonstrated in configurations with broad resonances. Additionally, excitation of GST with short pulses allows ultrafast tuning of these resonances in the ps regime without producing any phase transition. Finally, tuning of narrower resonances with shifts of 13 nm is also demonstrated.

In a second device demonstrator, a perfect absorber, we show how interference effects, occurring in multilayer thin film structures, can be exploited to achieve nearly 100% absorption. Two perfect absorption regimes are identified: the first one broadband and in the visible; the second one resonant and in the near infrared (NIR) region of the wavelengths. We show that the proposed method enables conceptually simple devices that are easy to fabricate. Moreover, we show that GST constitutes an essential layer for a new class of optical absorbers that can be dynamically tuned. In contrast, previous structures required cumbersome fabrication steps and were not dynamically tunable.

In a third device demonstrator, a structure with multilayer thin films is used to design and fabricate an anti-reflective, highly transparent electrode, with world-record low sheet electrical resistance and high optical transmission.

In summary, the thesis capitalizes on modelling tools for light-matter interaction at the nano-scale, which are adapted to a general class of device structures and allow us to design optical surfaces based on thin films and nano-structuring with unprecedented performance. This is demonstrated through the design and experimental realization of resonant optical filters with very large tunability, perfect absorbers with very high dynamic range and transparent electrodes with record electro-optical performance.

Resum

La fotònica és una tecnologia que permetrà implementar noves tecnologies en àrees tan diverses com les comunicacions, l'energia o la medicina. El seu èxit dependrà en gran mesura de la capacitat de controlar la llum en els dispositius òptics. En aquest sentit, entendre com la llum i la matèria interaccionen en aquests dispositius és un dels requisits principals a l'hora de trobar solucions efectives als reptes que ofereixen les diferents àrees d'aplicació de la fotònica.

Aquesta tesi té com a objectiu entendre les interaccions entre llum i matèria en estructures periòdiques i capes ultra-primes així com crear eines de disseny i modelat de dispositius òptics, alguns dels quals són també demostrats experimentalment.

A la primera part de la tesi s'investiga la teoria necessària per descriure la interacció de la llum en superfícies periòdiques nano-estructurades. Això inclou un estudi detallat de la transmissió, reflexió i dispersió d'estructures periòdiques en 2D o combinacions d'elles, així com també l'estudi d'estructures més complexes, com ara defectes, estructures aleatòries, i finalment el càlcul de la densitat local d'estats electromagnètics en aquestes estructures.

A la segona part de la tesi s'aplica aquesta teoria per dissenyar i entendre el comportament de dispositiu fotònics basats en aquestes estructures 2D per a aplicacions específiques.

El primer dispositiu que es demostra consisteix en una estructura periòdica de nano-forats en una capa d'or coberta amb $Ge_2Sb_2Te_5$ (GST), un material de canvi de fase. S'investiga l'efecte que té 'un canvi de fase en la capa de GST en les ressonàncies de transmissió d'aquestes estructures i es demostren canvis en la longitud d'ona de ressonància de fins a 385 nm en el cas de ressonàncies amples. A més a més també es demostra com excitant la capa de GST amb polsos ultracurts aquestes ressonàncies també es poden modificar en una escala de temps de

ps sense la necessitat de tenir un canvi de fase. Per últim també es demostren canvis en la longitud d'ona de ressonàncies de fins a 13 nm en dispositius amb ressonàncies estretes.

En el segon dispositiu es demostra com els efectes d'interferència que tenen lloc en estructures compostes per vàries capes primes poden ser explotats per tal d'obtenir una absorció de gairebé el 100%. En particular es demostren dos règims d'absorció completa: banda ampla en el visible i absorció ressonant en l'infraroig. Aquest mètode permet fabricar dispositius de manera fàcil. A més a més es demostra com el GST permet crear una nova classe de dispositius amb aborció completa que poden ser sintonitzats dinàmicament, en contrast amb la majoria d'estructures proposades fins al dia d'avui. En la tercera aplicació es dissenya i demostra experimentalment una estructura de vàries capes per a ser usada com a elèctrode transparent amb propietats d'antireflexió, i amb una resistència molt baixa i alta transmissió òptica.

En resum, aquesta tesi descriu eines per modelar la interacció entre llum i matèria en l'escala dels nanòmetres per una classe general d'estructures que després són usades per dissenyar superfícies òptiques basades en capes primes i nano-estructuració. En particular això es demostra amb el disseny i realització experimental de filtres òptics ressonants, dispositius amb absorció completa i gran rang dinàmic així com elèctrodes transparents amb unes grans propietats electro-òptiques.

Acknowledgments

I would like to thank all the people who contributed in some way to the work described in this thesis.

First of all, I would like to thank Prof. Valerio Pruneri for giving me the opportunity to work in the Optoelectronics group at ICFO, and for his continuous support and guidance during the course of this thesis. For his effort to keep me focused, at the same time his encouragement for the self-determination. For me, he is a grate example of a scientist who has permanent intention to bring the science into industry, formulating and transforming the ideas into real life products. The work under his supervision allowed me to follow the whole process of this transformation, which in other circumstances would have been difficult to follow up.

I would like to say special thank to Prof. Javier García de Abajo, who had kindly agreed to be the co supervisor of the thesis. I was feeling his permanent support during the whole period of the research, specially on the theoretical aspects of the work. I have learned a lot from him during the substantive discussions and have become greatly influenced by his research and his personality.

I have been very fortunate to have them as my supervisors and both of them have set a high level in science, which I will try to reach for the rest of my research carrier.

I would also like to thank, Simon Wall, Timothy A Miller, Dhriti Sundar Ghosh, Tong Lai Chen, Davide Janner, Miquel Rudé, Josep Canet-Ferrer, Rinu Abraham Maniyara, Kavitha Kalavoor Gopalan, for fruitful collaborations and discussions that led to the work presented here. It has been a pleasure working with all of them. A special mention also to all the researchers, technicians, and staff who helped me during my stay at ICFO, and to Lisa Ruby, for carefully proofreading this manuscript.

Personally, I would like to thank all the OPTO members and ICFO colleagues for making my daily work much more pleasant. All my friends, specially Karen Hovhannisian who was always up to meet and discuss some physics, philosophy, life and with whom I shared a lot of fun moments during the PhD.

Finally, I would like to thank to my wife, Lilit, for her love, care and patience. My newborn son, Areg, who brought new meaning and maturity to my life and made it more colourful, energetic and full of happiness. To my parents, who gave me everything I needed in my life. This thesis is devoted to all of them.

Contents

List of Figures

List of Tables

List of Publications

Publications included in this thesis

A **V. K. Mkhitaryan**, D. S. Ghosh, M. Rudé, J. Canet- Ferrer, R. Abraham Maniyara, K. K. Gopalan, and V. Pruneri, "Tunable complete optical absorption in multilayer structures including $Ge_2Sb_2Te_5$ without lithographic patterns," *Adv. Opt. Mater. 5, 1600452, (2017).*

B M. Rudé*, **V. K. Mkhitaryan***, A. E. Cetin, T. A. Miller, A. Carrilero, S. Wall, F. J. García de Abajo, H. Altug, and V. Pruneri, "Ultrafast and broadband tuning of resonant optical nanostructures using phase-change materials," *Adv. Opt. Mater.4,7, 1060-1066, (2016)* .***equal contribution**

C R. A. Maniyara*, **V. K. Mkhitaryan***, T. L. Chen, D. S. Ghosh & V. Pruneri "An antireflection transparent conductor with ultralow optical loss ($< 2\%$) and electrical resistance ($< 6\ \Omega\ \mathrm{sq}^{-1}$)," *Nat. Commun. 7, 13771, (2016).***equal contribution**

D **V. K. Mkhitaryan**, V. Pruneri and F. J. García de Abajo, "Comprehensive study of 2D periodic array of dipole scatterers", *in preparation*.

Other relevant publications and conference contributions

E T. L. Chen, D. S. Ghosh, **V. K. Mkhitaryan** & V. Pruneri, "Hybrid transparent conductive film on flexible glass formed by hot-pressing graphene on a silver nanowire mesh," *ACS Appl. Mater. Interfaces 5, 11756–11761 (2013)*

F D. S. Ghosh, T. L. Chen,**V. K. Mkhitaryan**, N. Formica, & V. Pruneri, "Solution processed metallic nanowire based transparent electrode capped with a multifunctional layer, " *Appl. Phys. Lett. 102(22), 221111, (2013).*

G D. S. Ghosh, T. L. Chen,**V. K. Mkhitaryan**, & V. Pruneri, "Ultrathin transparent conductive polyimide foil embedding silver nanowires," *ACS Appl. Mater. Interfaces 6, 20943–20948 (2014).*

H D. S. Ghosh, Q. Liu, P. Mantilla-Perez,T. L. Chen, **V. K. Mkhitaryan**, M. Huang, S. Garner, J. Martorell & V. Pruneri "Highly flexible transparent electrodes containing ultrathin silver for efficient polymer solar cells," *Adv. Funct. Mater. 25, 7309–7316 (2015).*

I **V. K. Mkhitaryan** D. S. Ghosh, M. Rude. J. Canet- Ferrer. R. Abraham Maniyara. K. K. Gopalan. & V. Pruneri, "Tunable complete optical absorption in multilayer structures including Ge_2 Sb_2 Te_5 without lithographic patterns". *in CLEO/Europe-EQEC 2017, Munich, Germany (2017).*

J **V. K. Mkhitaryan**, M. Rude and V. Pruneri,"Tunable Micro- and Nano-Structured Optical Devices Using Phase-Cange Materials" *invited MRS Spring Meeting (2017).*

K M. A. Noyan, K. K. Gopalan, R. A. Maniyara, M. M. Martin-Frances, **V. K. Mkhitaryan**, J. Rombaut Segarra, M. Rude, R. Sibilo, I. Mannelli, J. Canet-Ferrer, V. Pruneri, "Multifunctional nano-structured optical surfaces for industrial applications." *invited in 6th International Topical Meeting on Nanophotonics and Metamaterials, 4-7 January Seefeld (Tirol), Austria (2017).*

Chapter 1

Introduction

Light scattering, absorption, reflection and interference permeate our daily experience. We see an object and its colours because of the light being scattered, reflected or absorbed by that object into our eyes. Besides, light has been essential in many groundbreaking discoveries since the times of Galileo Galilei, who used the first telescope to see planets that are too far from us, and Robert Hooke, who used the first microscope to look at objects that are too small to be observed by the naked eye.

Due to its remarkable properties and capabilities, light still remains one of the most powerful tools in many areas of modern science. Its applications range from observing, tracking and imaging the behaviour of molecules to testing the fundamental laws of quantum mechanics and physics in general. A recent example is the enormous sensitivity of light interference effects, which was exploited to detect gravitational waves, predicted by Einstein and for a long time thought to be unmeasurable, beyond the reach of human technology.

On the micron- and nano-scale modern optics, the use of optical interference to enhance the performance of devices is one of the most important and efficient tools. In particular, interference effects in periodic structures have found important applications in photonic crystals, laser action in distributed feedback resonators, anomalous transmission through perforated metal films with subwavelength aperture arrays, image reconstruction, metamaterials, etc.

From a practical implementation perspective, the steady progress over the last ten years on the fabrication of photonic micro- and nano-structures has led to a rich variety of different one-, two-, and three-dimensional dielectric and/or

metallic structures. These systems exhibit novel and fascinating optical properties, providing an unprecedented control over light propagation and light–matter interaction.

For example, the interference effects occurring in thin film dielectric layers have been used in numerous applications, including optical coatings, photovoltaics, light emitting diodes, colour filtering and highly reflective broadband mirrors. Historically, thin films made of dielectric materials were the main focus of consideration for the applications. More recently, growing interest in the interference effects occurring in absorbing semiconductor and metallic films has developed, as those materials offer new types of interaction with light, including much stronger interference.

Another example of controlled light-matter interaction is the enhanced field confinement due to plasmons when thin metallic films are properly patterned. A well-known example is provided by enhanced optical transmission (EOT) through periodic hole patterned in noble metal thin films.

The main aim of this thesis is to understand light scattering and interference effects at the nanoscale level in order to enable the design of optical and optoelectronic devices for practical applications.

In Chapter 2, we develop a comprehensive theory to study light scattering by 2D periodic arrays of dipoles. This includes the study of reflection, transmission and dispersion properties of the arrays. In addition, we provide genuine extension of the theory, which enable the calculations of optical properties of defective lattices, random arrays, multicomponent lattices, etc. We also study the emission properties of an emitter sitting close to these kinds of 2D periodic arrays. The developed modelling and design tools are then applied to realize the demonstrators presented in the following chapters.

In Chapter 3, we investigate, both theoretically and experimentally, the optical response of a hybrid structure consisting of 2D arrays of holes drilled in a thin gold film combined with GST thin films. We demonstrate that one can tune the resonance of a hole array by triggering phase transitions in the GST film, in a dynamic, ultrafast regime.

In Chapter 4, we demonstrate a new design of perfect absorbers utilizing strong interference effects occurring in multilayer thin film structures. In addition to this we show how one can realize a tunable perfect absorber using a GST layer as a substantial layer in these structures.

Finally, in Chapter 5 we show how a careful choice of a multilayer thin film

structure enables the demonstration of a highly transparent, antireflective electrode design, with a world-record performance in terms of the trade-off between low electrical sheet resistance and high optical transmission.

Chapter 2

Scattering theory of 2D array of dipolar scatterers

2.1 Introduction

Periodic structures have been widely studied over the course of history both for practical purposes and out of pure theoretical interest. They were used in the context of diffraction gratings [1] and photonic crystals [2–4]. When the fields of plasmonics and metamaterials first emerged, periodic arrays were considered to be the key elements and building blocks for demonstrating various physical phenomena associated with those fields. In plasmonics, periodic arrays of small metal particles were suggested as candidates for subwavelength waveguiding [5, 6] due to the extreme localisation of visible light around nanoparticles. Two-dimensional periodic arrays of holes drilled in thick metal films were experimentally [7] demonstrated to support the so called extraordinary optical transmission (EOT) of light. Initially this was surprising because the transmitted intensities were much higher than the predictions for isolated holes [8]. Later this effect was explained theoretically [9, 10] to be the result of the coupling of external light into the diffraction modes of the periodic array. Alongside the theoretical interest, periodic plasmonic structures have been widely studied for various applications such as sensing [11–14], colour filtering [15], structural colouring [16], etc. Another important range of applications of periodic nanostructures lies within the field of metamaterials. Metamaterials have fascinating optical properties demonstrating negative refraction and subdiffraction focusing

among other things. It has been shown that perioidc arrays of scatterers with simultaneous electric and magnetic polarisabilites can serve as building blocks for such materials. Historically, arrays of subwavelength metallic structures, like wires [17] or split-ring resonators [18], which demonstrate strong electric and magnetic polarisabilities, have been used as building blocks for metamaterials. However, metallic structures suffer from ohmic losses, which limit the functionality of such metamaterials. More recently, researchers have started to look at all-dielectric structures [19, 20] to avoid ohmic losses, with great potential for large scale metamaterials. To realise such metamaterials, it is suggested that one uses dielectric particles with high refractive indices, which can support so-called Mie resonances (i.e., light confined within the dielectric structures, which play the role of a cavity). In particular, nanoparticles made of Si [21] or Ge [22] can have strong electric and magnetic dipolar Mie resonances in the NIR region, have been confirmed experimentally [23]. The simultaneous existence of electric and magnetic resonances leads to stronger dispersion, which suggest greater flexibility in the design of engineered metamaterial properties.

In many applications, including the ones mentioned above, the scatterers have sizes smaller than the light wavelength, which means that the optical response is dominated by induced dipoles. For this reason, one could consider only induced electric and magnetic dipole moments in describing the scattering of these particles. Dipole-scatterers models have already been successfully applied to explain experimental observations such as the EOT effect [24], as well as light guiding in arrays of small particles [6, 25], and also to describe the optical properties of metamaterials [26–28].

In this chapter we also adopt the point-dipole approximation for the scatterers and develop a general theoretical framework to describe the scattering by periodic arrays of such particles. Despite the simplicity of the suggested model, the theory is shown to adequately capture the main physics behind the observations. Additionally, the simple form of the resulting analytical expressions allows one to gain deeper insight into the mechanisms of scattering and their relation to scatterer and lattice properties.

2.2 General theoretical framework

Classical electromagnetic phenomena are governed by Maxwell's equations. Assuming an $e^{-i\omega t}$ time harmonic evolution for the fields, Maxwell's equations can

be written:

$$\nabla \times \mathbf{E} = i\omega\mu\mathbf{H}, \qquad \nabla \cdot \mathbf{E} = \frac{\rho}{\varepsilon}, \tag{2.1a}$$

$$\nabla \times \mathbf{H} = -i\omega\varepsilon\mathbf{E} + \mathbf{J}, \qquad \nabla \cdot \mathbf{H} = 0\,. \tag{2.1b}$$

where we assume that the current $\mathbf{J}$ and charge ρ distributions are in a homogeneous medium of dielectric constant $\varepsilon = \varepsilon_r\varepsilon_0$ and magnetic permeability $\mu = \mu_r\mu_0$, where the subscripts "r" and "0" correspond to relative and free-space quantities. Using the fact that $\mathbf{B} = \mu\mathbf{H}$ is divergenceless, we express the fields in terms of a vector $\mathbf{A}$ and scalar Φ potentials

$$\mu\mathbf{H} = \nabla \times \mathbf{A}, \qquad \mathbf{E} = i\omega\mathbf{A} - \nabla\Phi\,. \tag{2.2}$$

Adopting the Lorenz gauge for the potentials

$$\frac{1}{\mu}\nabla \cdot \mathbf{A} - i\omega\varepsilon\Phi = 0, \tag{2.3}$$

allows us to leave out the scalar potential and express the fields only in terms of the vector potential as:

$$\mathbf{E} = i\omega\mathbf{A} - \frac{1}{i\omega\varepsilon\mu}\nabla\left(\nabla \cdot \mathbf{A}\right), \qquad \mathbf{H} = \frac{1}{\mu}\nabla \times \mathbf{A}\,. \tag{2.4}$$

The vector potential satisfies the Helmholtz equation, as it can be readily verified by substituting the Eqs. (2.4) into Maxwell's equations

$$\nabla^2\mathbf{A} + k^2\mathbf{A} = -\mu\mathbf{J}\,, \tag{2.5}$$

where $k = \omega\sqrt{\mu\varepsilon}$. The formal solution of this equation can be expressed in terms of the scalar Green function defined by the equation:

$$\nabla^2 g(\mathbf{r} - \mathbf{r}') + k^2 g(\mathbf{r} - \mathbf{r}') = -\delta(\mathbf{r} - \mathbf{r}')\,, \tag{2.6}$$

which has the explicit form:

$$g(\mathbf{r} - \mathbf{r}') = \frac{e^{\pm ik|\mathbf{r}-\mathbf{r}'|}}{4\pi\,|\mathbf{r} - \mathbf{r}'|}\,. \tag{2.7}$$

Using this, the formal solutions of (2.5) reduces to

$$\mathbf{A}(\mathbf{r}) = \mu \int d^3r' g(\mathbf{r} - \mathbf{r}')\mathbf{J}(\mathbf{r}')\,. \tag{2.8}$$

The electric and magnetic fields outside the source region(i.e. when $\mathbf{r} \neq \mathbf{r}'$) can be obtained if we take the appropriate derivatives. By doing so, the fields can be expressed as

$$\mathbf{E}(\mathbf{r}) = i\omega\mu \int d^3r' G_e(\mathbf{r}-\mathbf{r}')\mathbf{J}(\mathbf{r}'), \tag{2.9a}$$

$$\mathbf{H}(\mathbf{r}) = ik \int d^3r' G_m(\mathbf{r}-\mathbf{r}')\mathbf{J}(\mathbf{r}')\,, \tag{2.9b}$$

where G_e and G_m are the so called electric and magnetic dyadic Green functions (DGF), which take the form

$$G_e(\mathbf{r}-\mathbf{r}') = \left(I - \frac{1}{k^2}\nabla\otimes\nabla\right) g(\mathbf{r}-\mathbf{r}'), \quad \mathbf{r}\neq\mathbf{r}', \tag{2.10a}$$

$$G_m(\mathbf{r}-\mathbf{r}') = \frac{1}{ik}\nabla\times G_e(\mathbf{r}-\mathbf{r}') = \frac{1}{ik}\left(I\times\nabla\right) g(\mathbf{r}-\mathbf{r}'), \quad \mathbf{r}\neq\mathbf{r}'\,. \tag{2.10b}$$

Here, I is the unit dyadic, which is a simple 3×3 unit matrix. It should be noted that these relations are valid only outside the source region because only in this situation we can bring the derivatives inside the integral and define the dyadic Green functions. The correct expression for the fields also in the source region can be written [29, 30]

$$\mathbf{E}(\mathbf{r}) = i\omega\mu \lim_{\delta\to 0}\int_{V'-V_\delta} d^3r' G_e(\mathbf{r}-\mathbf{r}')\mathbf{J}(\mathbf{r}') + \frac{\overleftrightarrow{L}\cdot\mathbf{J}(\mathbf{r})}{i\omega\varepsilon}\,, \tag{2.11}$$

where $\overleftrightarrow{L}$ is the so called depolarisation dyadic and its actual form depends on the geometry of the principal value volume V_δ [29]. In free space one can take a spherical volume around the point source for which $\overleftrightarrow{L} = I/3$.

The dyadic Green's functions can be found as solutions to the following differential equations [31]:

$$\mathcal{L}(\nabla;\omega)G_e(\mathbf{r}-\mathbf{r}';\omega) = -\delta(\mathbf{r}-\mathbf{r}')I, \tag{2.12a}$$

$$\mathcal{L}(\nabla;\omega)[ikG_m(\mathbf{r}-\mathbf{r}';\omega)] = -I\times\nabla\delta(\mathbf{r}-\mathbf{r}')\,, \tag{2.12b}$$

where $\mathcal{L}$ is the following linear dyadic differential operator

$$\mathcal{L}(\nabla;\omega) = I(\nabla^2+k^2) - \nabla\otimes\nabla\,. \tag{2.13}$$

These equations can be directly reduced from the wave equations for electric and magnetic fields, which follow from the Maxwell's equations as:

$$\mathcal{L}(\nabla;\omega)\mathbf{E} = -i\omega\mu\mathbf{J}, \tag{2.14a}$$
$$\mathcal{L}(\nabla;\omega)\mathbf{H} = -\nabla\times\mathbf{J}\,. \tag{2.14b}$$

We are now ready to calculate the electric and magnetic fields of any source distribution. In general one can expand any current distribution into a sum of point multipoles [32]. Usually the lowest order multipoles produce a dominant contributions in these expansions. The two lowest order moments correspond to electric and magnetic dipole distributions, which can be written as [32, 33]:

$$\mathbf{J}^{ED}(\mathbf{r},\omega) = -i\omega\mathbf{p}(\omega)\delta(\mathbf{r}-\mathbf{r}_0), \tag{2.15a}$$
$$\mathbf{J}^{MD} = -I\times\mathbf{m}(\omega)\cdot\nabla\delta(\mathbf{r}-\mathbf{r}_0)\,, \tag{2.15b}$$

where $\mathbf{p}(\omega)$ and $\mathbf{m}(\omega)$ are the electric and magnetic dipole moments of that current distribution expanded around the point $\mathbf{r}_0$. If we substitute these sources into Eqs. (2.9), we can immediately find the fields produced by these source as:

$$\mathbf{E}^{ED} = \frac{k^2}{\varepsilon}G_e(\mathbf{r},\omega)\mathbf{p}(\omega), \qquad \mathbf{H}^{ED} = \frac{k^2}{\sqrt{\varepsilon\mu}}G_m(\mathbf{r},\omega)\mathbf{p}(\omega), \tag{2.16a}$$
$$\mathbf{E}^{MD} = -k^2\sqrt{\frac{\mu}{\varepsilon}}G_M(\mathbf{r},\omega)\mathbf{m}(\omega), \qquad \mathbf{H}^{MD} = k^2G_e(\mathbf{r},\omega)\mathbf{m}(\omega)\,. \tag{2.16b}$$

If both electric and magnetic dipole moments are nonvanishing, the fields produced by them can be written in the matrix form as:

$$\begin{bmatrix}\mathbf{E}\\ \mathbf{H}\end{bmatrix} = \begin{bmatrix}\frac{k^2}{\varepsilon}G_e(\mathbf{r},\omega) & \frac{k^2}{\sqrt{\varepsilon\mu}}G_m(\mathbf{r},\omega)\\ -k^2\sqrt{\frac{\mu}{\varepsilon}}G_M(\mathbf{r},\omega) & k^2G_e(\mathbf{r},\omega)\end{bmatrix}\begin{bmatrix}\mathbf{p}\\ \mathbf{m}\end{bmatrix}. \tag{2.17}$$

Note that all the expressions for the fields and sources are given in the SI units system. Below, in the text and throughout the whole thesis, we will adopt a normalised units system where electric and magnetic fields have comparable magnitudes. This will allow us to cast the equations in a more symmetric form (2.17)

$$\begin{bmatrix}\mathbf{E}\\ \mathbf{H}\end{bmatrix} = \begin{bmatrix}(\hat{\mathbf{I}}k^2+\nabla\otimes\nabla)g & ik(\hat{\mathbf{I}}\times\nabla g)\\ -ik(\hat{\mathbf{I}}\times\nabla g) & (\hat{\mathbf{I}}k^2+\nabla\otimes\nabla)g\end{bmatrix}\begin{bmatrix}\mathbf{p}\\ \mathbf{m}\end{bmatrix}, \tag{2.18}$$

where $g(r)$ is now given as $g = \exp(ik\,|\mathbf{r}-\mathbf{r}_0|)/\,|\mathbf{r}-\mathbf{r}_0|$ and the comparison of the vectors $\mathbf{E}, \mathbf{H}, \mathbf{p}$ and $\mathbf{m}$ in these unit systems are summarized in the table below

$\mathbf{E} = \mathbf{E}^{SI}$	$\mathbf{p} = \dfrac{\mathbf{p}^{SI}}{4\pi\varepsilon\varepsilon_0}$
$\mathbf{H} = \sqrt{\dfrac{\mu\mu_0}{\varepsilon\varepsilon_0}}\mathbf{H}^{SI}$	$\mathbf{m} = \sqrt{\dfrac{\mu\mu_0}{\varepsilon\varepsilon_0}}\dfrac{\mathbf{m}^{SI}}{4\pi}$

Table 2.1: Comparison of units adopted in the thesis with those in the SI system

We now assume that we are given a scatterer that can be characterised through its dipolar polarisability tensor $\overleftrightarrow{\alpha}$, which is assumed to have the following general form:

$$\overleftrightarrow{\alpha} = \begin{bmatrix} \alpha_{ee} & \alpha_{em} \\ \alpha_{me} & \alpha_{mm} \end{bmatrix} . \tag{2.19}$$

The diagonal terms of the polarisability tensor represent the response of the scatterer to the local electric and magnetic fields, while the non-diagonal terms characterise its chirality. In the presence of local electric $\mathbf{E}_{loc}$ and magnetic $\mathbf{H}_{loc}$ fields, the induced electric $\mathbf{p}$ and magnetic $\mathbf{m}$ dipole moments can be written as [24, 26]:

$$\begin{bmatrix} \mathbf{p} \\ \mathbf{m} \end{bmatrix} = \overleftrightarrow{\alpha} \begin{bmatrix} \mathbf{E}_{\text{loc}} \\ \mathbf{H}_{\text{loc}} \end{bmatrix} . \tag{2.20}$$

If a dipolar scatterer sits at the position $\mathbf{r}_0 = (x_0, y_0, z_0) = (\mathbf{R}_0, z_0)$ then the fields produced at any other point $\mathbf{r}$ can be calculated as

$$\begin{bmatrix} \mathbf{E}_{\text{sc}} \\ \mathbf{H}_{\text{sc}} \end{bmatrix} = \overleftrightarrow{\mathcal{G}}^0(\mathbf{r}-\mathbf{r}_0) \begin{bmatrix} \mathbf{p} \\ \mathbf{m} \end{bmatrix} , \tag{2.21}$$

where by $\overleftrightarrow{\mathcal{G}}^0(\mathbf{r}-\mathbf{r}')$ we denote

$$\overleftrightarrow{\mathcal{G}}^0(\mathbf{r}-\mathbf{r}') = \begin{bmatrix} \overleftrightarrow{\mathcal{G}}^0_E(\mathbf{r}-\mathbf{r}') & \overleftrightarrow{\mathcal{G}}^0_H(\mathbf{r}-\mathbf{r}') \\ -\overleftrightarrow{\mathcal{G}}^0_H(\mathbf{r}-\mathbf{r}') & \overleftrightarrow{\mathcal{G}}^0_E(\mathbf{r}-\mathbf{r}') \end{bmatrix} , \tag{2.22}$$

with

$$\overleftrightarrow{\mathcal{G}}^0_E(\mathbf{r}-\mathbf{r}') = (\hat{\mathbf{I}}k^2 + \nabla\otimes\nabla)g, \qquad \overleftrightarrow{\mathcal{G}}^0_H(\mathbf{r}-\mathbf{r}') = ik(\hat{\mathbf{I}}\times\nabla g)\,. \tag{2.23}$$

For the sake of compactness, we will adopt the following notations hereafter

$$\boldsymbol{\mu} = [\mathbf{p},\ \mathbf{m}]^T, \quad \mathbf{F} = [\mathbf{E},\ \mathbf{H}]^T, \tag{2.24}$$

where the superscript T stands for transpose. With these notations the equations (2.20) and (2.21) take the forms

$$\boldsymbol{\mu} = \overleftrightarrow{\alpha}\mathbf{F}_{\text{loc}}, \qquad \mathbf{F}_{\text{sc}} = \overleftrightarrow{\mathcal{G}}^0(\mathbf{r}-\mathbf{r}_0)\boldsymbol{\mu}\,. \tag{2.25}$$

Now, suppose one is given a 2D array of such scatterers as schematically represented in Figure 2.1. In this case, the local external field at the position of each individual dipole is a superposition of the incidence field and the fields produced by all the other dipoles in the array. Thus, we can write the following set of equations describing the induced dipole moments of the particles:

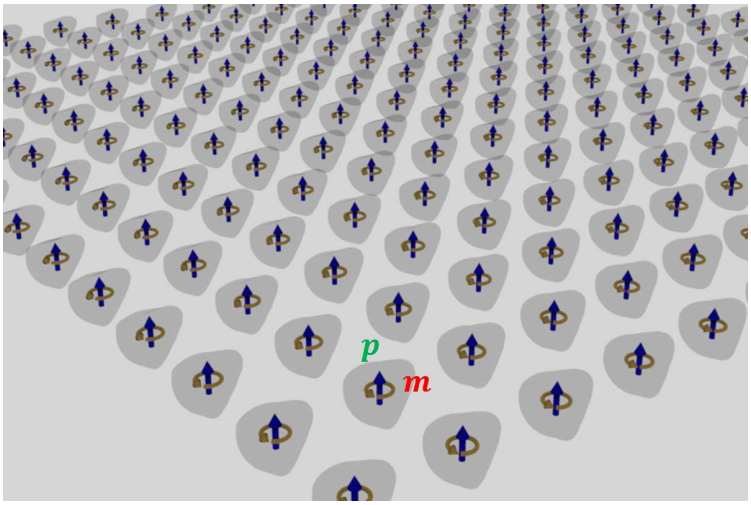

Figure 2.1: Schematic of 2D array of scatterers, with both electric and magnetic polaisabilities.

$$\boldsymbol{\mu}_{\boldsymbol{l}} = \overleftrightarrow{\alpha}\left(\mathbf{F}^{\text{inc}}_{\boldsymbol{l}} + \sum_{\boldsymbol{l}\neq\boldsymbol{l}'} \overleftrightarrow{\mathcal{G}}^0(\mathbf{r}_{\boldsymbol{l}}-\mathbf{r}_{\boldsymbol{l}'})\boldsymbol{\mu}_{\boldsymbol{l}'}\right), \tag{2.26}$$

where $\boldsymbol{l} = (m,n)$ is a pair of integers $(m,n = 0,\pm1,\pm2,...)$ that numerate the lattice sites with position vectors $\mathbf{r}_{\boldsymbol{l}} = (\mathbf{R}_{\boldsymbol{l}}, z_0)$. Here $\mathbf{R}_{\boldsymbol{l}} \equiv \mathbf{R}_{mn} = m\mathbf{a}_1 + n\mathbf{a}_2$

and $\mathbf{a}_1$, $\mathbf{a}_2$ are the primitive vectors of the direct lattice. This infinite set of equations can be reduced to a single vector equation using the lattice in-plane translational invariance

$$(\boldsymbol{\mu}_{\boldsymbol{l}},\ \mathbf{F}_{\boldsymbol{l}}^{\text{inc}}) = (\boldsymbol{\mu},\ \mathbf{F}_0^{\text{inc}})e^{i\mathbf{k}_\parallel \mathbf{R}_{\boldsymbol{l}}}\,. \tag{2.27}$$

Using this, we reduce equation (2.26) to

$$\boldsymbol{\mu} = \boldsymbol{\Omega}\mathbf{F}_0^{\text{inc}}\,, \tag{2.28}$$

where we have defined

$$\boldsymbol{\Omega} = \left[\overleftrightarrow{\alpha}^{-1} - \mathbf{G}^{\neq}(\mathbf{k}_\parallel,\omega)\right]^{-1} = \begin{bmatrix} \boldsymbol{\Omega}_{ee} & \boldsymbol{\Omega}_{em} \\ \boldsymbol{\Omega}_{me} & \boldsymbol{\Omega}_{mm} \end{bmatrix}\,, \tag{2.29}$$

and $\mathbf{G}^{\neq}(\mathbf{k}_\parallel,\omega)$ is the so called lattice sums matrix generalised for the 6x6 DGF [34]:

$$\mathbf{G}^{\neq}(\mathbf{k}_\parallel,\omega) = \sum_{\boldsymbol{l}\neq\boldsymbol{l}'} \overleftrightarrow{\mathcal{G}}^0(\mathbf{r}_{\boldsymbol{l}} - \mathbf{r}_{\boldsymbol{l}'})e^{i\mathbf{k}_\parallel(\mathbf{R}_{\boldsymbol{l}'}-\mathbf{R}_{\boldsymbol{l}})}\,. \tag{2.30}$$

Taking into account the definitions in (2.22), we can write the lattice sums as a combined matrix

$$\mathbf{G}^{\neq}(\mathbf{k}_\parallel,\omega) = \begin{bmatrix} G(\mathbf{k}_\parallel,\omega) & H(\mathbf{k}_\parallel,\omega) \\ -H(\mathbf{k}_\parallel,\omega) & G(\mathbf{k}_\parallel,\omega) \end{bmatrix}\,, \tag{2.31}$$

with previously known [24] 3×3 dyadic lattice sums

$$G = \sum_{\boldsymbol{l}\neq\boldsymbol{l}'} \overleftrightarrow{\mathcal{G}}{}^0_E(\mathbf{r}_{\boldsymbol{l}} - \mathbf{r}_{\boldsymbol{l}'})e^{i\mathbf{k}_\parallel(\mathbf{R}_{\boldsymbol{l}'}-\mathbf{R}_{\boldsymbol{l}})}\,, \tag{2.32a}$$

$$H = \sum_{\boldsymbol{l}\neq\boldsymbol{l}'} \overleftrightarrow{\mathcal{G}}{}^0_H(\mathbf{r}_{\boldsymbol{l}} - \mathbf{r}_{\boldsymbol{l}'})e^{i\mathbf{k}_\parallel(\mathbf{R}_{\boldsymbol{l}'}-\mathbf{R}_{\boldsymbol{l}})}\,. \tag{2.32b}$$

These sums are slowly convergent and a special treatment is required for their calculation. A widely known method to accelerate these kinds of sums was introduced by Ewald [35, 36] in the context of electron scattering theory in solid state physics. Readers can find an excellent review on the methods and details of these calculations in the reference papers [37, 38]. We Briefly summarise the method in Appendix A.

For completeness, we also give here the explicit forms for the response function Ω, since this will be very useful when we start discussing dispersion effects in the lattice. The explicit forms can be obtained using the definitions (2.30), (2.32) combined with block matrix inversion formulas from matrix algebra, given by:

$$\Omega_{ee} = \left[(\alpha_{ee}^{-1} - G) + H(\alpha_{mm}^{-1} - G)^{-1}H\right]^{-1}, \tag{2.33a}$$

$$\Omega_{em} = \left[-H - (\alpha_{mm}^{-1} - G)H^{-1}(\alpha_{ee}^{-1} - G)\right]^{-1}, \tag{2.33b}$$

$$\Omega_{me} = \left[H + (\alpha_{ee}^{-1} - G)H^{-1}(\alpha_{mm}^{-1} - G)\right]^{-1}, \tag{2.33c}$$

$$\Omega_{mm} = \left[(\alpha_{mm}^{-1} - G) + H(\alpha_{ee}^{-1} - G)^{-1}H\right]^{-1}. \tag{2.33d}$$

Once we find the dipole moments, we are able to calculate the scattered field of the array simply as a superposition of the fields radiated by all dipoles in the array:

$$\mathbf{F}_{\text{sc}}^{\text{tot}}(\mathbf{r}) = \sum_{\boldsymbol{l}} \overleftrightarrow{\mathcal{G}}^{0}(\mathbf{r} - \mathbf{r}_{\boldsymbol{l}})e^{i\mathbf{k}_{\parallel}\mathbf{R}_{\boldsymbol{l}}}\boldsymbol{\mu}\,. \tag{2.34}$$

This gives the total fields produced by the array. A simpler form for the field expressions can be obtained in the far-field limit. For far-field calculations, it is useful to introduce the following spectral decomposition of the scalar Green function [39]:

$$\frac{e^{ik|\mathbf{r}-\mathbf{r}_0|}}{|\mathbf{r}-\mathbf{r}_0|} = \frac{i}{2\pi}\int \frac{d^2\mathbf{Q}}{k_{zQ}} e^{i\mathbf{Q}\cdot(\mathbf{R}-\mathbf{R}_0)\pm ik_{zQ}|z-z_0|}\,, \tag{2.35}$$

where the integration extends over $\mathbf{Q} = (Q_x, Q_y)$ 2D wave vectors and $k_{zQ} = \sqrt{k^2 - Q^2}$ with $\mathcal{I}m\{k_{zQ}\} > 0$. The sign in front of k_{zQ} is taken as that of $(z - z_0)$ [31]. Using this we can express the dyadic Green functions in the spectral form

$$\overleftrightarrow{\mathcal{G}}^{0}(\mathbf{r} - \mathbf{r}_0) = \frac{i}{2\pi}\int \frac{d^2\mathbf{Q}}{k_{zQ}} \mathbf{M}^{\pm}(\mathbf{Q}) e^{i\mathbf{Q}\cdot(\mathbf{R}-\mathbf{R}_0)\pm ik_{zQ}|z-z_0|}\,, \tag{2.36}$$

with the $\mathbf{M}^{\pm}(\mathbf{Q})$ matrices given by

$$\mathbf{M}^{\pm}(\mathbf{Q}) = \begin{bmatrix} (\hat{\mathbf{I}}k^2 - \mathbf{K}_{\mathbf{Q}}^{\pm} \otimes \mathbf{K}_{\mathbf{Q}}^{\pm}) & -k(\hat{\mathbf{I}} \times \mathbf{K}_{\mathbf{Q}}^{\pm}) \\ k(\hat{\mathbf{I}} \times \mathbf{K}_{\mathbf{Q}}^{\pm}) & (\hat{\mathbf{I}}k^2 - \mathbf{K}_{\mathbf{Q}}^{\pm} \otimes \mathbf{K}_{\mathbf{Q}}^{\pm}) \end{bmatrix}, \tag{2.37}$$

where $\mathbf{K}_{\mathbf{Q}}^{\pm} = (\mathbf{Q}, \pm k_{zQ})$. Substituting expression (2.36) into equation (2.34) and changing the order of summation and integration, we find

$$\mathbf{F}_{\text{sc}}^{\text{tot}} = \frac{i}{2\pi} \int \frac{d^2\mathbf{Q}}{k_{zQ}} \mathbf{M}^{\pm}(\mathbf{Q}) \boldsymbol{\mu} e^{i\mathbf{Q}\mathbf{R} \pm i k_{zQ}|z - z_0|} \sum_{\boldsymbol{l}} e^{-i(\mathbf{Q} - \mathbf{k}_{\parallel})\mathbf{R}_{\boldsymbol{l}}}. \tag{2.38}$$

This integral can be carried out directly if we use the Poisson summation formula [37]

$$\sum_{\boldsymbol{l}} e^{-i(\mathbf{Q} - \mathbf{k}_{\parallel})\mathbf{R}_{\boldsymbol{l}}} = \frac{(2\pi)^2}{A} \sum_{\mathbf{g}} \delta(\mathbf{Q} - \mathbf{k}_{\parallel} - \mathbf{g}), \tag{2.39}$$

where $\mathbf{g} = q\mathbf{g}_1 + q\mathbf{g}_2$ is the reciprocal lattice vector defined through its primitive vectors $\mathbf{g}_1$ and $\mathbf{g}_2$, with (p, q) being a pair of integers representing different diffraction modes $(p, q) = 0, \pm 1, \pm 2, ...)$. After carrying out the integration we obtain

$$\mathbf{F}_{sc}^{\text{tot}}(\mathbf{R}, z) = \frac{2\pi i}{A} \sum_{\mathbf{g}} \mathbf{M}^{\pm}(\mathbf{k}_{\parallel} + \mathbf{g}) \boldsymbol{\mu} \frac{e^{i(\mathbf{k}_{\parallel} + \mathbf{g})\mathbf{R} \pm i k_{z\mathbf{g}}|z - z_0|}}{k_{z\mathbf{g}}}, \tag{2.40}$$

where $\mathbf{M}^{\pm}(\mathbf{k}_{\parallel} + \mathbf{g})$ is again given by (2.37) with $\mathbf{Q}$ replaced by $\mathbf{g} + \mathbf{k}_{\parallel}$ and k_{zQ} by $k_{z\mathbf{g}} = \sqrt{k^2 - \left|\mathbf{k}_{\parallel} + \mathbf{g}\right|^2}$. Note that, when $\left|\mathbf{k}_{\parallel} + \mathbf{g}\right| > |k|$, $k_{z\mathbf{g}}$ becomes purely imaginary, so the waves are not radiative and do not contribute to the far field. Moreover, when the incident light wavelength is larger than the lattice spacing, we can keep only the $(p, q) = (0, 0)$ normal propagating beam. In this situation, we find a simple analytical formula for scattered far fields:

$$\mathbf{F}^{\pm}(\mathbf{R}, z) = \frac{2\pi i}{A} \mathbf{M}^{\pm}(\mathbf{k}_{\parallel}) \boldsymbol{\mu} \frac{e^{i\mathbf{k}_{\parallel}\mathbf{R} \pm i k_z |z - z_0|}}{k_{z\mathbf{k}_{\parallel}}}. \tag{2.41}$$

To summarise, we see that the point dipole description gives a transparent and intuitive way of calculating the scattering characteristics of the array. Having established the main ingredients of the calculations, we are ready to discuss various physical properties of the 2D periodic arrays and consider many problems involving such arrays.

2.3 Array Reflection

2.3.1 Suspended array

As a first step, we use equation (2.41) to calculate the reflection of the array and compare the results with those calculated using a more rigorous theory beyond the dipole-scatterer approximation. As an example, we consider a 2D lattice of spherical particles for which both the polarisabilities (Mie theory [40]) and the reflection of the array [41] can be calculated analytically. A rigorous solution of Maxwell's equations involve the use of spherical harmonic expansions and incorporate an arbitrary number of multipole source distributions for individual spheres, in contrast to the dipole model that we consider here. It is known [21] that the electric and magnetic dipole polarisabilities of a spherical particle can be expressed in terms of the Mie scattering coefficients a_1 and b_1 as

$$\alpha_{ee} = \frac{3}{2} i k^3 a_1, \qquad \alpha_{mm} = \frac{3}{2} i k^3 b_1 \,, \tag{2.42}$$

where the explicit forms of the scattering coefficients a_1 and b_1 are given in Appendix B. Note that the form we give here is different from that given in reference [21] due to our normalised unit system (see Table 2.1). Furthermore, in our calculations we use spherical particles with dipole polarisabilities given by (2.42) unless it is stated otherwise.

Let us now consider a free-standing periodic array of spherical scatterers with their centres located on the $xy-$plane. We assume $\varepsilon_h = 1$ and $\varepsilon_{sp} = 16.0$ to be the dielectric constants of the host medium and the sphere, respectively. A light plane wave is incident on the array from the upper halfspace towards the negative direction of the z-axis. To begin with, let the electric field of this wave be s-polarised: $\mathbf{E}^-_{\text{in}} = \hat{\mathbf{e}}_s E_{0s} e^{i\mathbf{k}\cdot\mathbf{r}}$, with $\mathbf{k} = (\mathbf{k}_\parallel, -k_z)$ and $k_z = (k^2 - k_\parallel^2)^{1/2}$. So that the magnetic field will be $\mathbf{H}^-_{\text{in}} = -\hat{\mathbf{e}}^-_p E_{os} e^{i\mathbf{k}\cdot\mathbf{r}}$, where the unit vectors of the polarization directions are defined as $\hat{\mathbf{e}}_s = (-k_y/k_\parallel, k_x/k_\parallel, 0)$ and $\hat{\mathbf{e}}^\pm_p = (\pm k_x k_z/k k_\parallel, \pm k_y k_z/k k_\parallel, -k_\parallel/k)$. Substituting these expression into equation (2.28), we can relate the induced dipole moments to the incident field amplitudes as follows:

$$\mathbf{p} = (\boldsymbol{\Omega}_{ee}\hat{\mathbf{e}}_s - \boldsymbol{\Omega}_{me}\hat{\mathbf{e}}^-_p)E_{0s}, \qquad \mathbf{m} = (\boldsymbol{\Omega}_{me}\hat{\mathbf{e}}_s - \boldsymbol{\Omega}_{mm}\hat{\mathbf{e}}^-_p)E_{0s}\,. \tag{2.43a}$$

Substituting this into the expression (2.41) for the scattered far field, and using

the tensor identities

$$\mathbf{I}k^2 - (\mathbf{K}^{\pm} \otimes \mathbf{K}^{\pm}) = k^2\big[(\hat{\mathbf{e}}_s \otimes \hat{\mathbf{e}}_s) + (\hat{\mathbf{e}}_p^{\pm} \otimes \hat{\mathbf{e}}_p^{\pm})\big], \tag{2.44a}$$

$$\hat{\mathbf{I}} \times \mathbf{K}^{\pm} = k\big[(\hat{\mathbf{e}}_s \otimes \hat{\mathbf{e}}_p^{\pm}) - (\hat{\mathbf{e}}_p^{\pm} \otimes \hat{\mathbf{e}}_s)\big], \tag{2.44b}$$

$$(\mathbf{a} \otimes \mathbf{b})\mathbf{c} = (\mathbf{b} \cdot \mathbf{c})\mathbf{a}\,, \tag{2.44c}$$

we can write the scattered electric far-field component as

$$\mathbf{E}_{\text{sc}}^{\pm} = \frac{2\pi i k^2}{A k_z}\big(\gamma_s^{\pm}\hat{\mathbf{e}}_s + \gamma_p^{\pm}\hat{\mathbf{e}}_p^{\pm}\big) = E_s^{\text{sc}}\hat{\mathbf{e}}_s + E_p^{\text{sc}}\hat{\mathbf{e}}_p^{+}\,, \tag{2.45}$$

with $\gamma_{s,p}^{\pm}$ defined as

$$\gamma_s^{\pm} = (\hat{\mathbf{e}}_s \cdot \mathbf{p}) - (\hat{\mathbf{e}}_p^{\pm} \cdot \mathbf{m}), \qquad \gamma_p^{\pm} = (\hat{\mathbf{e}}_p^{\pm} \cdot \mathbf{p}) + (\hat{\mathbf{e}}_s \cdot \mathbf{m})\,. \tag{2.46}$$

We note that, although the incidence electric field is s-polarised, the scattered field can have both polarisations due to anisotropy of the scattered field of a dipole and the simultaneous presence of the electric and magnetic responses of the scatterer. However, the amplitude of the cross-polarised field for isotropic particles is usually much smaller than the same polarisation component because the cross coupling terms of the interaction tensor are comparatively small. In particular, they are exactly zero for square lattices at normal incidences due to symmetry considerations.

Knowing the scattered far fields, we can find the reflection coefficients of the array:

$$r_{ss} = \frac{2\pi i k^2}{A k_z E_{0s}}\gamma_s^{+}, \qquad r_{sp} = \frac{2\pi i k^2}{A k_z E_{0s}}\gamma_p^{+}\,, \tag{2.47}$$

where r_{ss} and r_{sp} relate the s-polarised and p-polarised scattered fields to the s-polarised incident field. Similar considerations for the case of p-polarised incidence lead to:

$$r_{ps} = \frac{2\pi i k^2}{A k_z E_{0p}}\gamma_s^{+}, \qquad r_{pp} = \frac{2\pi i k^2}{A k_z E_{0p}}\gamma_p^{+}\,. \tag{2.48}$$

Now we can calculate the reflectance of the array defined as $R = |r_{ss}|^2$ and compare it with rigorous calculations including higher-order multipoles. In these rigorous calculations we have included multipoles with a maximum angular momentum number l_{max} in the range from 4 to 8, with a basis of up to g_{max} = 8

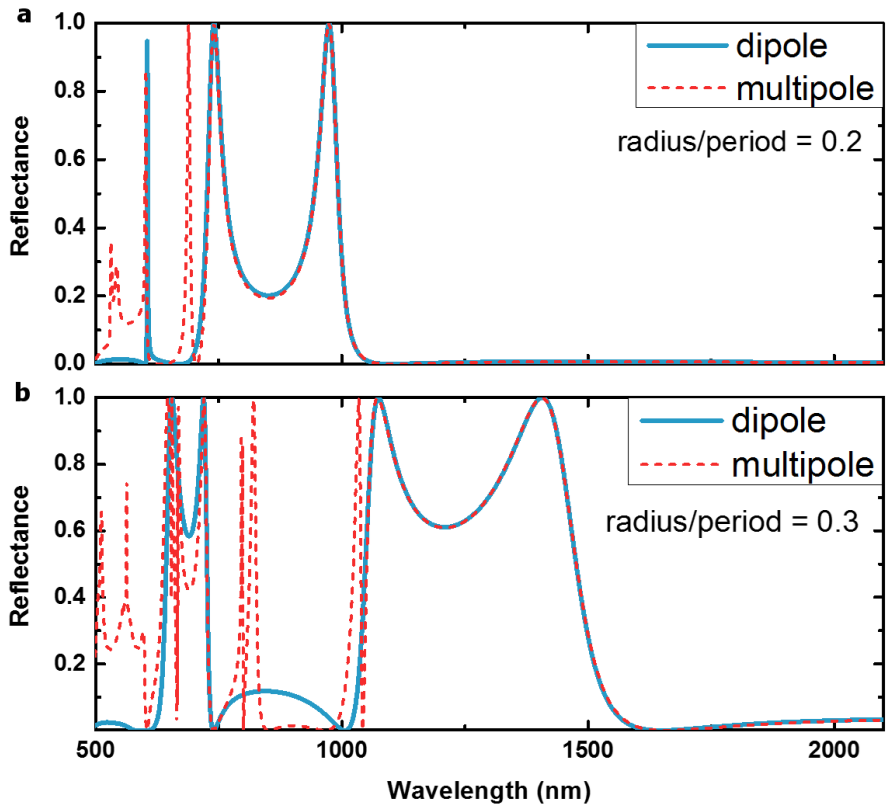

Figure 2.2: Calculated reflectance of 2D lattice of spherical particles with $\varepsilon_{sp} = 16$ dielectric constant in air. The dashed curves correspond to multipole simulations and the solid curves to dipole-model calculations. The multipole calculations were carried out with l_{max} = 4, g_{max} = 4 . Parts (a) and (b) are obtained for different ratios of the sphere radius to the period (see labels).

diffracted beams (see the Ref [41] for the meaning of these parameters). However, the calculations were already convergent with the values: l_{max} = 4, g_{max} = 4, for the parameter set (i.e. lattice spacing , particle size and dielectric constants) under consideration. The results of these calculations are given in Figure 2.2 for two different values for the sphere-radius to lattice-spacing ratio: 0.2 in Figure 2.2(a). and 0.3 for (b). The calculations were performed for a square lattice with fixed lattice spacing. We can see that the reflection calculations with

both methods match in the long wavelength region, while for the low wavelength region the dipole model fails to predict other resonances caused by higher-order multipoles (e.g, electric and magnetic quadrupole, etc.). This behaviour was expected because the dipole approximation is only valid for wavelengths that are much larger than the size of the scatterers. However, for many applications the particle dimensions are in the nanometre range, so that the electric and magnetic dipole moments have dominant contributions. This means that theory can be in good agreement with experiment when excitation wavelengths are in the visible or longer wavelength range.

Having the above limitation in mind, we can now proceed to discuss various optical properties of 2D arrays of such scatterers. Firstly, we note that distinct resonances show up in the reflection spectra. These resonances are due to the diffraction of light on the array and coherent superposition of the scattered fields in the far-field region. We can explore the origins of these resonances using the explicit form (2.33) for the induced dipole moments. They demonstrate that resonances show up whenever the tensor Ω diverges (i.e, when $\Omega^{-1} \to 0$). To simplify this condition, we first assume that the particles demonstrate only non-vanishing electric dipole polarisability. This allows us to reduce the resonance condition to

$$\alpha_{ee}^{-1} - G = 0\,. \tag{2.49}$$

Alternatively, if only the magnetic dipole polatisability is non-vanishing, the magnetic dipole (or magnetic field) resonance condition reduces to

$$\alpha_{mm}^{-1} - G = 0\,. \tag{2.50}$$

We can now cross-check these conditions with the reflection resonance peaks to distinguish the different origins of each observed resonance. To do so, we note that for normal incidence both the electric and magnetic fields are in the plane perpendicular to the z-axis. In particular, for s-polarised incidence we have $\mathbf{E} = (0, E_y, 0)$ and $H = (-H_x, 0, 0)$. This means that the induced electric dipole is preferentially oriented along the y-axis, while the magnetic dipole is mainly along the x-axis. Taking into account that the anisotropic components of the lattice sums (2.32a) are small compare with the diagonal ones, we can consider only the G_{xx} component for the electric dipole resonance condition and only G_{yy} for the magnetic dipole resonance condition. Moreover, since $G_{xx} = G_{yy}$ as follows from the definition, we need to consider only the first diagonal element

G_{xx} of the lattice sum matrix. This greatly simplifies the resonance conditions, reducing them to the scalar relations:

$$\mathcal{R}e\left\{\alpha_{ee}^{-1}\right\} = \mathcal{R}e\left\{G_{xx}\right\}, \quad \text{for the electric field resonance,} \tag{2.51a}$$

$$\mathcal{R}e\left\{\alpha_{mm}^{-1}\right\} = \mathcal{R}e\left\{G_{xx}\right\}, \quad \text{for the magnetic field resonance.} \tag{2.51b}$$

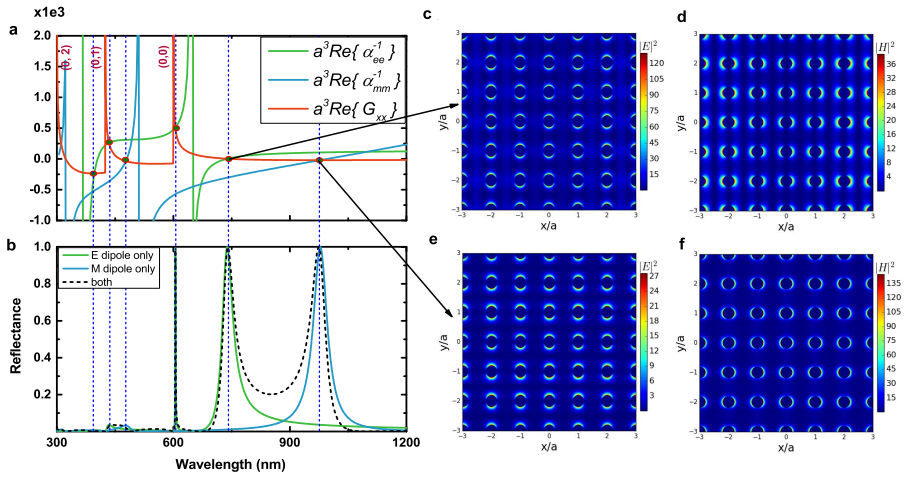

Figure 2.3: (a) Plots of the real parts of electric dipole (solid green curve) and magnetic dipole (solid blue curve) polarisabilities as well as the xx-component of the interaction tensor G (solid red curve) as a function of light wavelength. (a) shares the x axis scale and labelling of the (b) axis. (b) Reflectance of the array when only electric dipoles are taken into account (solid green curve), only magnetic dipoles are taken into account (solid blue curve) and both electric and magnetic dipoles are taken into account (dashed black curve). (c), (d) Electric and magnetic near field distributions at electric resonance wavelengths, (e), (f) same as (c) and (d) but for the magnetic resonance wavelength.

In Figure 2.3(a) we have plotted the wavelength dependence of the real parts of the electric (solid green curve) and magnetic (solid blue curve) dipole polarisabilities along with the real parts of the lattice sum G_{xx} (solid red curve). According to equations (2.51), the crossing point of the polarisability curve with the lattice sums curve corresponds to the resonance wavelength. In order to see this, we also plotted the reflectance of the array for three separate cases: when only the electric polarisability is non-vanishing (solid green curve), when only the magnetic polarisability is non-vanishing (solid blue curve) and, finally, when

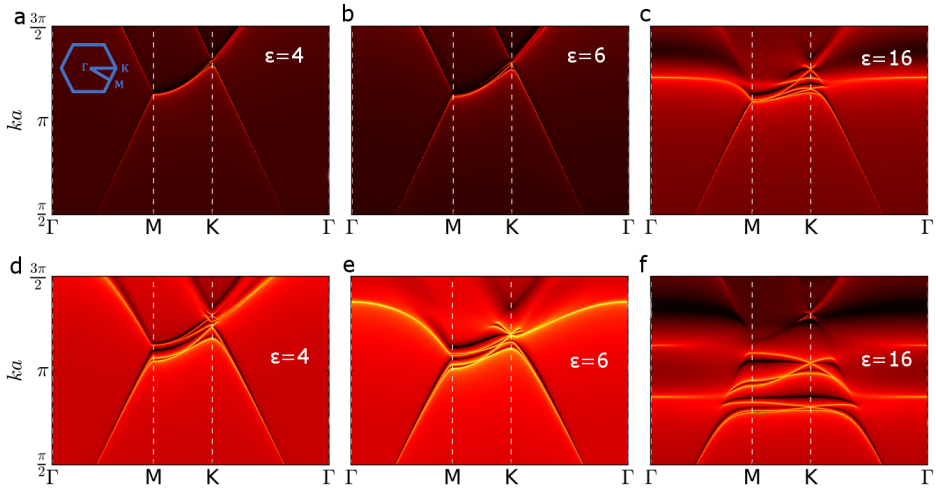

Figure 2.4: Dispersion maps for arrays of spherical particles. The plots represent the sum of imaginary parts of eigenvalues of the lattice polarisability tensor Ω for hexagonal arrays of spherical particles with sphere-radius to lattice-period ratio equal to 0.2 in (a)-(c) and 0.3 in (e)-(f). The dielectric function of the sphere is marked on teach maps.

both electric and magnetic polarisabilities are simultaneously present (dashed black curve). We can see that whenever the polarisability curve crosses the lattice sum curve a resonance clearly pops up in the reflection spectrum. In this way, one can track whether the resonance in the reflection spectrum has electric or magnetic origin. This can be further highlighted by the electric and magnetic near-field distribution plots. The respective values for these are shown in Figure 2.3(c) and (d) for electric resonance wavelengths and in Figure 2.3(e) and (f) for magnetic resonance wavelengths. We see that for the electric field resonance, the local electric field is an order of magnitude stronger than the magnetic field at the same wavelength. This is in contrast to the magnetic field resonance, in which the magnetic field is one order stronger than the corresponding electric field. In a general case, in order to find the nontrivial solutions of the system (2.28), we need to solve the equation

$$\det\left[\Omega(\omega, \mathbf{k}_{\|})\right] = 0\,. \tag{2.52}$$

This is the so-called characteristic equation of the system, which allows one to

find the general mode dispersion $\omega = \omega(\mathbf{k}_{\|})$ of the array. Because, in this case both $\overleftrightarrow{\alpha}$ and $\mathbf{G}^{\neq}(\omega, \mathbf{k}_{\|})$ depend on ω, this equation is highly nonlinear and one has to use numerical root searching algorithms to find the solutions. Historically, two approaches have been adopted in the literature for this task: either looking for real ω and complex $\mathbf{k}_{\|}$ pairs or vice versa. However, finding these solutions is a time consuming task, so we have followed the route suggested in reference [28] and have simply mapped the eigenvalues of the Ω matrix, which characterise the effective polarisability of the scatterers in the lattice. Moreover, since the extinction spectrum of the scatterer is proportional to the imaginary part of its polarisability, we have mapped the imaginary parts of the eigenvalues of Ω on the mesh-grid of real $\mathbf{k}_{\|}$ and ω, thereby mapping the extinction spectrum of the array. We have carried out this mapping for a hexagonal array of spherical particles with different dielectric constants for real ω, and $\mathbf{k}_{\|}$'s along the high symmetry excursion $\Gamma - M - K - \Gamma$ in the 1st Brillouin zone of the hexagonal lattice. The dielectric constants for the spheres were taken to be $\varepsilon = 4,\ 6,\ 16$. For each value of the dielectric constant, the calculations were carried out for two values of the sphere-radius to period ratio equal to 0.2 in Figures 2.4(a)-(c) and 0.3 in Figures 2.4(d)-(f), respectively. After mapping the eigenvalues, distinct dispersion curves show up, each corresponding to a particular mode of the array. We see that the number of dispersion lines increases both when increasing the dielectric constant of the spheres, whilst keeping the radius fixed, and for the fixed dielectric constant when the ratio of sphere radius to lattice constant is increasing. The reason for this behaviour is that the number of Mie resonances of the individual sphere in both cases is increasing. These modes then form bands through collective interaction of the particles in the lattice.

2.3.2 Supported array

In a more common situation, when the lattice is supported on a substrate or it is embedded in a sandwiched structure, we use a scattering matrix to describe the scattering of the structure, which is an approach similar to that developed in [42, 43] for sphere arrays. This allows us to calculate complex structures like the one schematically depicted in Figure 2.5, where instead of having a single layer of scatterers one has multiple layers of scatters which are restricted to have the same lattice structure but can have any dipole scatterer in a unit cell. As long as the polarisabilities are specified one can calculate the optical response of the complete system using analytical methods similar to the ones described above.

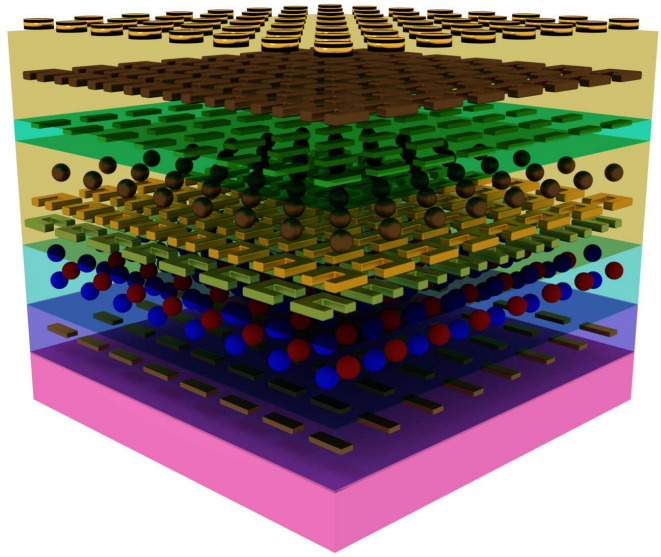

Figure 2.5: Schematic representation of the stack of dipole-scatterer periodic arrays.

To show this, we depart from the equation (2.40) and use the identities (2.44) to express the scattered electric field in the following form:

$$\left[\mathbf{E}_{\mathrm{sc}}\right]^{\nu} = \sum_{\mathbf{g}} \sum_{\substack{\sigma=1,2 \\ \sigma'' \neq \sigma'}} \left[\mathbf{E}_{sc}\right]^{\nu}_{\mathbf{g}\sigma} \hat{\mathbf{e}}^{\nu}_{\mathbf{g}\sigma} e^{i\mathbf{K}^{\nu}_{g}\cdot\mathbf{r}}\,, \tag{2.53}$$

with

$$\left[\mathbf{E}_{\mathrm{sc}}\right]^{\nu}_{\mathbf{g}\sigma} = \frac{2\pi i k^2}{k_{z\mathbf{g}} A}\left[\left(\hat{\mathbf{e}}^{\nu}_{\mathbf{g}\sigma}\cdot\mathbf{p}\right) + (-1)^{\sigma}\left(\hat{\mathbf{e}}^{\nu}_{\mathbf{g}\sigma''}\cdot\mathbf{m}\right)\right], \tag{2.54}$$

where σ numerates the polarisation state of the wave, with $\sigma = 1$ corresponding to s-polarisation and $\sigma = 2$ to p - polarisation. For the prescribed incidence field

$$\mathbf{E}_{\mathrm{in}} = \mathbf{E}_0 e^{i\mathbf{K}\cdot\mathbf{r}}\,, \tag{2.55}$$

with $\mathbf{K} = (\mathbf{k}_{\parallel}, k_z)$, $k_z = \sqrt{k^2 - k_{\parallel}^2}$, we can always represent the parallel component of the incidence wave vector $\mathbf{k}_{\parallel}$ as $\mathbf{k}_{\parallel} = \mathbf{q} + \mathbf{g}'$, where $\mathbf{q}$ lies in the 1st

Brillouin zone and $\mathbf{g}'$ is one of the reciprocal lattice vectors. We can also deal with a general plane wave by projecting it on s- and p-polarisation components, writing it as

$$\mathbf{E}_{\text{in}} = \left[\mathbf{E}_{\text{in}}\right]_{\mathbf{g}'}^{\nu'} = \sum_{\sigma'=1,2} \left[\mathbf{E}_{\text{in}}\right]_{\mathbf{g}'\sigma'}^{\nu'} e^{\mathbf{K}_{\mathbf{g}'}^{\nu'}\cdot\mathbf{r}} \hat{\mathbf{e}}_{\mathbf{g}'\sigma'}^{\nu'} , \tag{2.56}$$

where σ' again labels the polarisation states. Using equation (2.28), and after some algebraic manipulations, we find the induced dipole moments to be given

$$\begin{aligned} \mathbf{p}_{\mathbf{g}'}^{\nu'} &= \sum_{\substack{\sigma=1,2 \\ \sigma'''\neq\sigma'}} \left[\boldsymbol{\Omega}_{ee}\hat{\mathbf{e}}_{\mathbf{g}'\sigma'}^{\nu'} + (-1)^{\sigma'}\boldsymbol{\Omega}_{me}\hat{\mathbf{e}}_{\mathbf{g}'\sigma'''}^{\nu'}\right]\left[\mathbf{E}_{in}\right]_{\mathbf{g}'\sigma'}^{\nu'}, \\ \mathbf{m}_{\mathbf{g}'}^{\nu'} &= \sum_{\substack{\sigma=1,2 \\ \sigma'''\neq\sigma'}} \left[\boldsymbol{\Omega}_{em}\hat{\mathbf{e}}_{\mathbf{g}'\sigma'}^{\nu'} + (-1)^{\sigma'}\boldsymbol{\Omega}_{mm}\hat{\mathbf{e}}_{\mathbf{g}'\sigma'''}^{\nu'}\right]\left[\mathbf{E}_{in}\right]_{\mathbf{g}'\sigma'}^{\nu'} . \end{aligned} \tag{2.57}$$

Substituting these expressions into equation (2.54), it reduces to

$$\left[\mathbf{E}_{\text{sc}}\right]_{\mathbf{g}\sigma}^{\nu} = \sum_{\sigma'} T_{\mathbf{g}\sigma,\mathbf{g}'\sigma'}^{\nu\nu'} \left[\mathbf{E}_{\text{in}}\right]_{\mathbf{g}'\sigma'}^{\nu'} , \tag{2.58}$$

where

$$\begin{aligned} T_{\mathbf{g}\sigma,\mathbf{g}'\sigma'}^{\nu\nu'} = \frac{2\pi i k^2}{k_{z\mathbf{g}} A} \Bigg[&\left[\boldsymbol{\Omega}_{ee}\hat{\mathbf{e}}_{\mathbf{g}'\sigma'}^{\nu'} + (-1)^{\sigma'}\boldsymbol{\Omega}_{me}\hat{\mathbf{e}}_{\mathbf{g}'\sigma'''}^{\nu'}\right]\cdot\hat{\mathbf{e}}_{\mathbf{g}\sigma}^{\nu} \\ &+ (-1)^{\sigma}\left[\boldsymbol{\Omega}_{em}\hat{\mathbf{e}}_{\mathbf{g}'\sigma'}^{\nu'} + (-1)^{\sigma'}\boldsymbol{\Omega}_{mm}\hat{\mathbf{e}}_{\mathbf{g}'\sigma'''}^{\nu'}\right]\cdot\hat{\mathbf{e}}_{\mathbf{g}\sigma''}^{\nu}\Bigg] . \end{aligned} \tag{2.59}$$

From here, we can repeat the procedure used in [43] to construct the reflection and transmission matrices, which in our case, take the form

$$M_{\mathbf{g}\sigma,\mathbf{g}'\sigma'}^{\nu\nu'} = \delta_{\nu\nu'}\delta_{\mathbf{g}\mathbf{g}'}\delta_{\sigma\sigma'} + T_{\mathbf{g}\sigma,\mathbf{g}'\sigma'}^{\nu\nu'} . \tag{2.60}$$

Now we can construct the generalised scattering matrices with respect to new origins $\mathbf{d}_l$ and $\mathbf{d}_r$ from the left and right of the array centre, respectively,

$$\begin{aligned} S^{I} &= M_{\mathbf{g}\sigma,\mathbf{g}'\sigma'}^{++} e^{i(\mathbf{K}_{\mathbf{g}}^{+}\cdot\mathbf{d}_r + \mathbf{K}_{\mathbf{g}'}^{+}\cdot\mathbf{d}_l)}, \\ S^{II} &= M_{\mathbf{g}\sigma,\mathbf{g}'\sigma'}^{+-} e^{i(\mathbf{K}_{\mathbf{g}}^{+}\cdot\mathbf{d}_r - \mathbf{K}_{\mathbf{g}'}^{-}\cdot\mathbf{d}_r)}, \\ S^{III} &= M_{\mathbf{g}\sigma,\mathbf{g}'\sigma'}^{-+} e^{-i(\mathbf{K}_{\mathbf{g}}^{-}\cdot\mathbf{d}_l - \mathbf{K}_{\mathbf{g}'}^{+}\cdot\mathbf{d}_l)}, \\ S^{IV} &= M_{\mathbf{g}\sigma,\mathbf{g}'\sigma'}^{--} e^{-i(\mathbf{K}_{\mathbf{g}}^{-}\cdot\mathbf{d}_l + \mathbf{K}_{\mathbf{g}'}^{-}\cdot\mathbf{d}_r)} . \end{aligned} \tag{2.61}$$

If we also construct the scattering matrices for a dielectric slab sandwiched between two half-spaces in exactly the same way as was done in Ref. [43], we can build the global scattering matrices for any combined structures. The total scattering matrix of the layered structure allows to calculate the reflected and transmitted field amplitudes as

$$[\mathbf{E}_{\text{tr}}]^{+}_{\mathbf{g},\sigma} = \sum_{\sigma,\mathbf{g}} M^{++}_{\mathbf{g}\sigma,\mathbf{g}'\sigma'}[\mathbf{E}_{\text{in}}]^{+}_{\mathbf{g}',\sigma'}, \quad [\mathbf{E}_{\text{rf}}]^{-}_{\mathbf{g},\sigma} = \sum_{\sigma,\mathbf{g}} M^{-+}_{\mathbf{g}\sigma,\mathbf{g}'\sigma'}[\mathbf{E}_{\text{in}}]^{+}_{\mathbf{g}',\sigma'}\,. \quad (2.62)$$

Then, the total reflection and transmission can be calculated as the ratio of the fluxes of the respective reflected and transmitted waves to the flux of the incident wave, that is,

$$R = \frac{\sum_{\mathbf{g},\sigma}\left|[\mathbf{E}_{\text{rf}}]^{-}_{\mathbf{g},\sigma}\right|^2 k^{+}_{z\mathbf{g}}}{\sum_{\sigma'}\left|[\mathbf{E}_{\text{in}}]^{+}_{\mathbf{g}',\sigma'}\right|^2 k^{+}_{z\mathbf{g}'}}, \qquad T = \frac{\sum_{\mathbf{g},\sigma}\left|[\mathbf{E}_{\text{tr}}]^{+}_{\mathbf{g},\sigma}\right|^2 k^{+}_{z\mathbf{g}}}{\sum_{\sigma'}\left|[\mathbf{E}_{\text{in}}]^{+}_{\mathbf{g}',\sigma'}\right|^2 k^{+}_{z\mathbf{g}'}}\,. \quad (2.63)$$

We now proceed with calculations for specific cases to demonstrate how the theory can be applied to study the properties of supported arrays. To begin with, we again take a 2D periodic array of spherical scatterers, but this time with their centres located at some distance above the semi-infinite substrate extended from $z = 0$ towards the negative z-*axis*. The presence of the substrate will contribute to the local field acting on individual scatterer. This is because both the incident field and the scattered fields from other particles in the array will be reflected from the substrate and act back on scatterers. Moreover, the reflected fields will contribute in the far field by interfering with the upwards scattered fields. These are the two main mechanisms for how the presence of the substrate modifies the scattering characteristics of the array. To explore these effects, we have calculated the reflection of a square array of spheres with a radius to period ratio $r/a = 0.2$ and a dielectric constant $\varepsilon = 16.0$ for different values of the particle-substrate distance z_0. For comparison purposes, we took two different types of substrates, one made of dielectric with a dielectric constant $\varepsilon_{sub} = 2.25$, while the other is assumed to be made of gold. The superstrate medium is fixed for both cases and simply taken to be air. The results of these calculations are given in the Figure 2.6(a), for z_0 distances taken in the range of 1 nm to $3a$, where a is the lattice constant. Note that z_0 is measured from the bottom of the spheres. From previous calculations (see Figure 2.3), we saw that the free-standing array with the same geometric parameters supports distinct reflection resonances attributed to diffraction orders in the array. In the presence of the substrate some

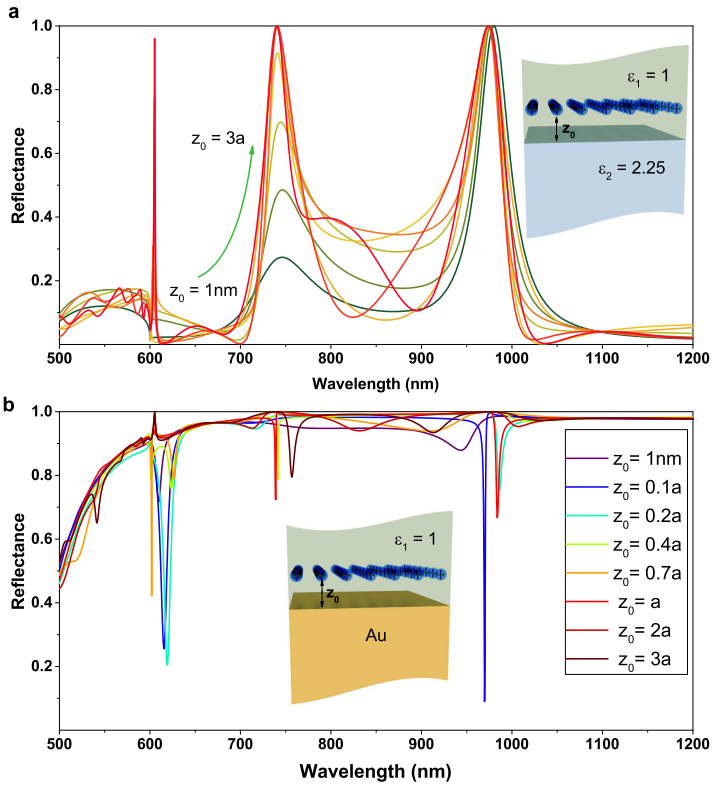

Figure 2.6: Reflectance plots for 2D square lattice of spheres with dielectric function $\varepsilon_{sp} = 16$ placed above a substrate (a) with fixed dielectric constant equal to $\varepsilon_2 = 2.25$ for different values of the distance z_0 from the surface of the substrate, and (b) the same as in (a) but for a gold substrate.

of these resonances start to decrease in magnitude, while others are completely suppressed. In particular, one can look at the purple curve in Figure 2.6(a), which corresponds to the case in which the sphere nearly touches the substrate. In this situation, all the electric field resonances are greatly affected by the substrate. The electric field resonance corresponding to the (1,1) diffraction beam is completely suppressed and the magnitude of the electric resonance corresponding to the (0, 1) diffraction beam is notably reduced. This effect of diffraction sup-

pression for electric resonances has been noted in previous works [44], where the electric resonance cancellations were attributed to multiple scattering effects of the diffracted beams from the substrate, and subsequent destructive interference of the fields. In contrast to the electric field resonances, the magnitude of the magnetic field resonance is barely affected and only shifted slightly towards longer wavelengths. To explain this, we note, that in the presence of a substrate one can describe the system with modified Green's functions by representing it as a sum of free-space and reflection GFs:

$$\overleftrightarrow{\mathcal{G}}(\mathbf{r},\mathbf{r}') = \overleftrightarrow{\mathcal{G}}_0(\mathbf{r}-\mathbf{r}') + \overleftrightarrow{\mathcal{G}}_R(\mathbf{r},\mathbf{r}')\,, \tag{2.64}$$

where the $\overleftrightarrow{\mathcal{G}}_0(\mathbf{r}-\mathbf{r}')$ is the free space DGF defined in (2.36), while the second term $\overleftrightarrow{\mathcal{G}}_R(\mathbf{r},\mathbf{r}')$ is the contribution due to the substrate which in the spectral form can be easily shown to reduce to

$$\overleftrightarrow{\mathcal{G}}_R(\mathbf{r},\mathbf{r}') = \frac{ik^2}{2\pi}\int \frac{d^2\mathbf{Q}}{k_{zQ}} \begin{bmatrix} M^R_{ee} & M^R_{em} \\ M^R_{me} & M^R_{mm} \end{bmatrix} e^{i\mathbf{Q}(\mathbf{R}-\mathbf{R}')+ik_{zQ}|z-z'|}\,, \tag{2.65}$$

with the M-matrices defined as

$$M^R_{ee} = \tilde{r}_{sQ}(\hat{\mathbf{e}}_{sQ}\otimes\hat{\mathbf{e}}_{sQ}) + \tilde{r}_{pQ}(\hat{\mathbf{e}}^+_{pQ}\otimes\hat{\mathbf{e}}^-_{pQ}), \tag{2.66a}$$

$$M^R_{ee} = -\tilde{r}_{sQ}(\hat{\mathbf{e}}_{sQ}\otimes\hat{\mathbf{e}}^-_{pQ}) + \tilde{r}_{pQ}(\hat{\mathbf{e}}^+_{pQ}\otimes\hat{\mathbf{e}}_{sQ}), \tag{2.66b}$$

$$M^R_{ee} = -\tilde{r}_{sQ}(\hat{\mathbf{e}}^+_{pQ}\otimes\hat{\mathbf{e}}_{sQ}) + \tilde{r}_{pQ}(\hat{\mathbf{e}}_{sQ}\otimes\hat{\mathbf{e}}^-_{pQ}), \tag{2.66c}$$

$$M^R_{ee} = \tilde{r}_{sQ}(\hat{\mathbf{e}}^+_{pQ}\otimes\hat{\mathbf{e}}^-_{pQ}) + \tilde{r}_{p}(\hat{\mathbf{e}}_{sQ}\otimes\hat{\mathbf{e}}_{sQ})\,. \tag{2.66d}$$

Here, $[\tilde{r}_{s,Q},\tilde{r}_{p,Q}] = [r_{sQ},r_{pQ}]e^{2ik_{zQ}z_0}$ and r_{sQ}, r_{pQ} are the Fresnel reflection coefficients of the substrate for s-polarised and p-polarised waves with parallel wavevector $\mathbf{Q}$. Following similar discussions as for the suspended array, the induced dipole moments for this case can be written as

$$\boldsymbol{\mu} = \tilde{\boldsymbol{\Omega}}\mathbf{F}_0^{\text{ext}}\,, \tag{2.67}$$

with

$$\mathbf{F}_0^{\text{ext}} = \mathbf{F}_0^{\text{inc}} + \mathbf{F}_0^{\text{R}},$$
$$\tilde{\boldsymbol{\Omega}} = \left(\overleftrightarrow{\alpha}^{-1} - \mathbf{G}^{\neq}(\mathbf{k}_\parallel,\omega) - \mathbf{G}^{R}(\mathbf{k}_\parallel,\omega)\right)^{-1},$$

where $\mathbf{F}_0^{\mathrm{R}}$ represents the reflected fields from the substrate, and

$$\mathbf{G}^R(\mathbf{k}_\parallel,\omega) = \sum_{l'} \overleftrightarrow{\mathcal{G}}_R(-\mathbf{r}_{l'}) e^{i\mathbf{k}_\parallel\cdot\mathbf{R}_{l'}} \,. \tag{2.68}$$

Hence, similarly to the suspended array, the resonance conditions for the supported arrays reduce to

$$\mathcal{R}e\left\{\alpha_{ee}^{-1}\right\} = \mathcal{R}e\left\{G_{xx}\right\} + \mathcal{R}e\left\{G_{xx}^R\right\}, \tag{2.69a}$$

$$\mathcal{R}e\left\{\alpha_{mm}^{-1}\right\} = \mathcal{R}e\left\{G_{xx}\right\} + \mathcal{R}e\left\{G_{xx}^R\right\} \,. \tag{2.69b}$$

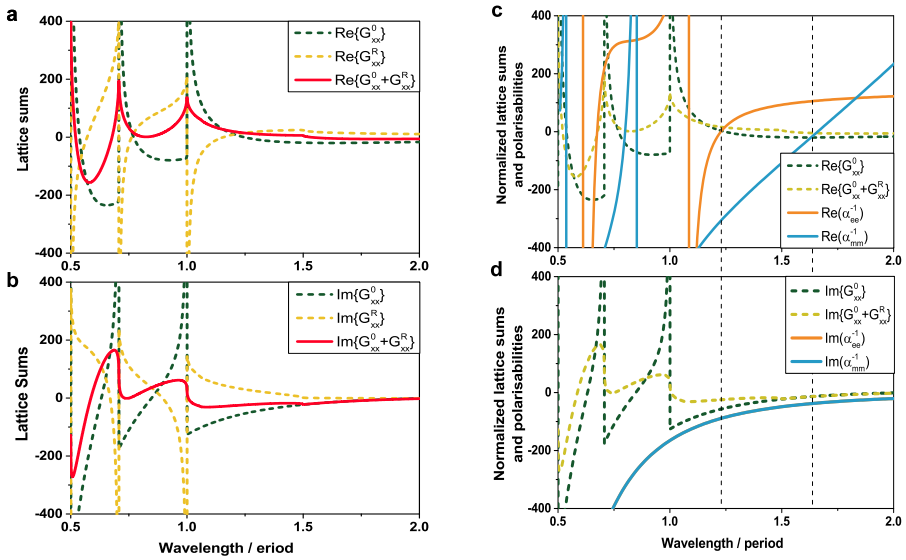

Figure 2.7: Lattice sums and resonance condition for a supported array. (a) Real and (d) imaginary parts of free-space (dashed green curve), reflection (dashed orange curve) and total (solid red curve) lattice sums for a square lattice. The substrate is assumed to have dielectric constant equal to 2.25 (glass) and the distance z_0 is taken to be 1 nm. (b) Real and (d) imaginary parts of the polarisabilities and lattice sums versus wavelength.

In order to study the effect of the substrate on the resonances, we have plotted the real and imaginary parts of the lattice sums and polarisabilities in Figure 2.7. In particular, in Figures 2.7(a) and (c) we plotted the real and imaginary parts

of the lattice sums for the free-space GF, the reflection GF and their sum. We see that the reflected lattice sum is out of phase with respect to the free-space sum and tends to cancel it out, thus removing the singularities. In particular, we note that the total lattice sums experience bigger changes close to the regions of stronger dispersion. This explains why all the electric field resonances are strongly affected by the presence of the substrate, while the magnetic field resonances are altered much less.

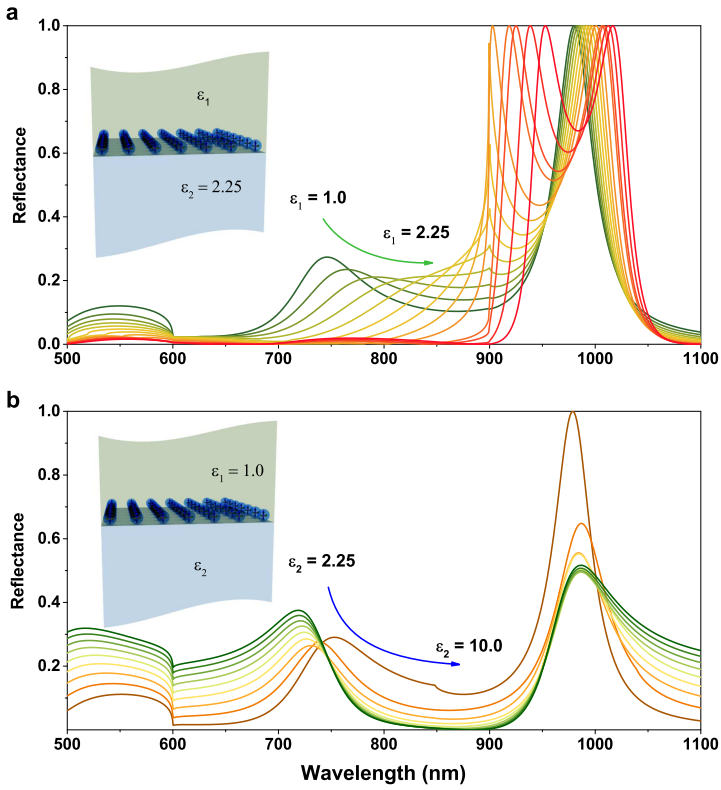

Figure 2.8: Reflection calculation for 2D array of spheres on a dielectric substrate. In (a) the dielectric constant of the superstrate is swept from $\varepsilon_1 = 1$ to $\varepsilon_1 = 2.25$ for a fixed value $\varepsilon_2 = 2.25$ of the substrate dielectric constant. In (b) the dielectric constant of the substrate is swept from $\varepsilon_2 = 1.0$ to $\varepsilon_2 = 10.0$ for a fixed value $\varepsilon_1 = 1$ of the superstrate dielectric constant.

This is because, for this particular choice of geometrical parameters and dielectric constants, the resonance conditions for the electric resonances are met at the wavelengths that are close to the strongly modified regions, whereas the magnetic resonance conditions are met at longer wavelengths where the changes in the lattice sums are smaller. Indeed, from Figure 2.7(d) it is clear that at the electric resonance wavelength, the changes in both the real and the imaginary parts of the lattice sums are stronger than at the magnetic resonance wavelength. We also note that both the electric and the magnetic field resonance conditions for this case are met at longer wavelengths compared to free space (see Figure 2.7(b)) which explains the observed red shifts in the resonances. For a gold substrate (Figure 2.6(b)) both the electric and magnetic resonances are strongly affected by the presence of the substrate. Since the substrate is highly reflective, we do not see significant reflection resonances in this case, and instead we see narrow dips when the resonance conditions are met. In contrast to dielectric substrates, for metal substrates, when a resonance is excited, the electromagnetic field becomes trapped between the substrate and the array just like in Fabry-Pérot cavities. Consequently, after multiple reflection it eventually gets absorbed by the metal substrate, resulting in resonant absorption, which shows up as dips in the reflection spectrum. We further analyse the effects of the substrate by now fixing the distance z_0 and changing its dielectric constant. For these calculations we fix $z_0 = 1$nm (where the spheres are nearly touching the substrate), and change the dielectric functions of either the superstrate (Figure 2.8(a)) or the substrate (Figure 2.8(b)). In Figure 2.8(a), for all values of the superstrate dielectric constant we see that the electric resonances due to (1,1)-order diffraction are completely suppressed. The magnitude of the electric resonance corresponding to (0,1) diffraction is also decreased. However, when the dielectric constant of the superstrate becomes closer to that of the substrate, accompanying the disappearance of the initial resonance, another resonance emerges corresponding to the free standing array suspended in the host medium with the dielectric constant of the substrate. While the electric field resonances experience dramatic changes, the magnitudes of the magnetic resonances remain constant and the resonances are redshifted. If, instead of the superstrate we change the dielectric constant of the substrate making it more reflective, both electric and magnetic resonances experience bigger changes. All of these effects can be explained with an analysis similar to that carried out above. For completeness, we also examine another configuration commonly used in experimental studies, where an array of scatter-

ers is placed on top of a dielectric or a metallic waveguide. The results of some of the calculations are presented in Figure 2.9(a) for the dielectric waveguide and Figure 2.9(b) for the metallic waveguide. In both cases, we assume the same 2D square lattice of spherical scatterers with a dielectric constant equal to 16.0. The dielectric constant is $\varepsilon_w = 4.0$ for the dielectric waveguide and the calculations are carried out for two different thicknesses t_w of the waveguide, as indicated in the legend of Figure 2.9(a).

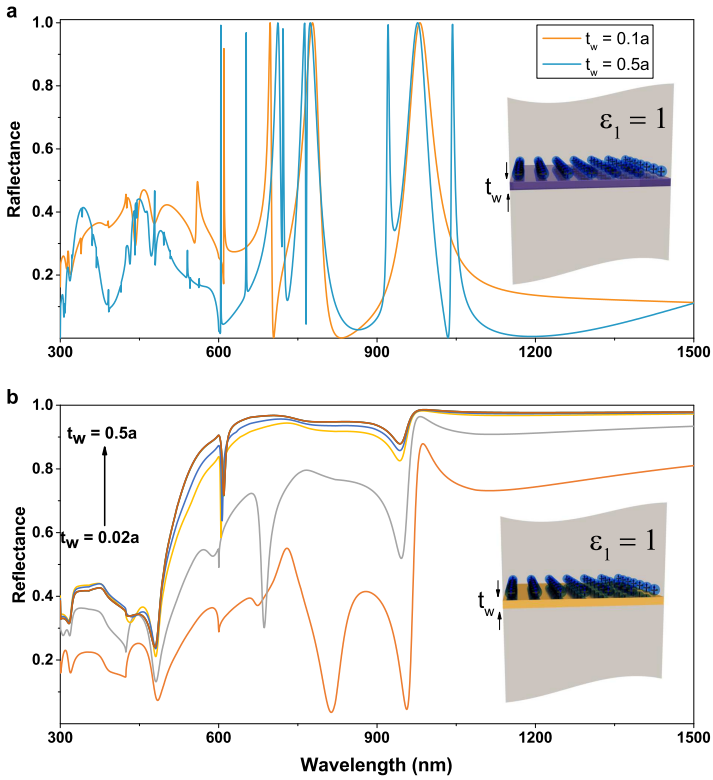

Figure 2.9: Reflectance plots of a 2D square lattice of sphere with dielectric constant $\varepsilon_{sp} = 16.0$ placed above a thin waveguide. (a) Reflectance for a dielectric waveguide of dielectric constant $\varepsilon_w = 4.0$ and for two different thicknesses of the waveguide t_w. (b) Same as for (a), but with a metal waveguide made of gold.

Similar calculations for a waveguide made of a thin gold layer of different thicknesses are given in Figure 2.9(b). In both cases, besides the reflection resonances of the corresponding free-standing array, we see additional peaks and dips appearing in the spectrum. In the dielectric waveguide, the number of these peaks increases with increasing waveguide thickness.

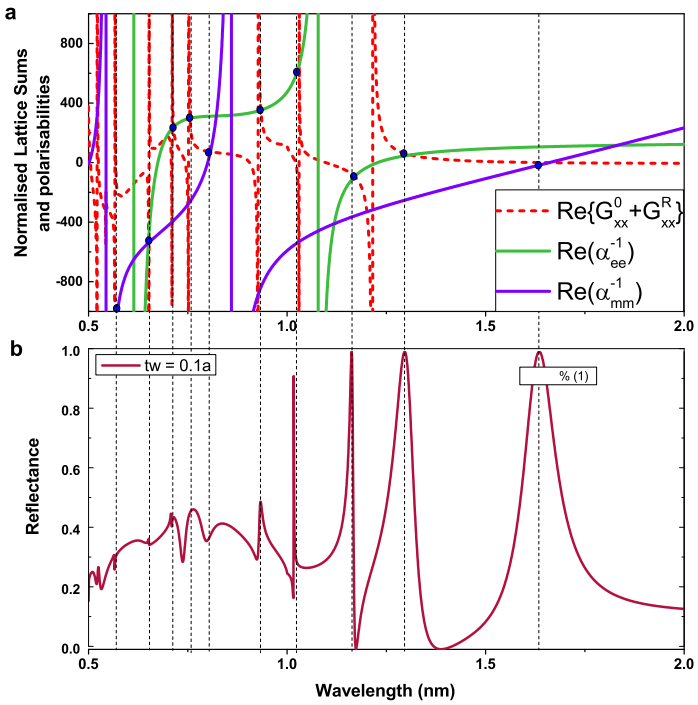

Figure 2.10: Reflection resonances and lattice sums of a thin dielectric waveguide. (a) Normalised lattice sums and polarisabilities for an array of spheres with dielectric constants $\varepsilon_{sp} = 16.0$. The dielectric constant of the waveguide is 4.0 and the ratio of the thickness to lattice period is 0.1. (b) Reflectance of array with specified parameters.

These resonances can be attributed to the hybridisation of the waveguide modes with lattice modes. To demonstrate this, we again recall the spectral form

of the reflection lattice sum (2.68),

$$\mathbf{G}^R(\mathbf{k}_\parallel,\omega) = \frac{2\pi i k^2}{A}\sum_{\mathbf{g}}\frac{e^{2ik_{zg}z_0}}{k_{zg}} \times \begin{bmatrix} r_s(\hat{\mathbf{e}}_{sg}\otimes\hat{\mathbf{e}}_{sg}) + r_p(\hat{\mathbf{e}}^+_{pg}\otimes\hat{\mathbf{e}}^-_{pg}) & -r_s(\hat{\mathbf{e}}_{sg}\otimes\hat{\mathbf{e}}^-_{pg}) + r_p(\hat{\mathbf{e}}^+_{pg}\otimes\hat{\mathbf{e}}_{sg}) \\ -r_s(\hat{\mathbf{e}}^+_{pg}\otimes\hat{\mathbf{e}}_{s}) + r_p(\hat{\mathbf{e}}_{sg}\otimes\hat{\mathbf{e}}^-_{pg}) & r_s(\hat{\mathbf{e}}^+_{pg}\otimes\hat{\mathbf{e}}^-_{pg}) + r_p(\hat{\mathbf{e}}_{sg}\otimes\hat{\mathbf{e}}_{sg}) \end{bmatrix}, \tag{2.70}$$

where both the reflection coefficients and polarisation vectors are now defined for plane waves with $\mathbf{k}_\parallel$ replaced by $\mathbf{k}_\parallel + \mathbf{g}$. The spectral form (2.70) shows the explicit dependence of the reflection lattice sums on the Fresnel reflection coefficients. As we know, the waveguide modes are signalled by the poles of the reflection coefficients of the waveguide layer. Hence, along with diffraction divergences, the reflection lattice sum exhibit a new form of divergences that come from these poles. This means that it is now possible to satisfy the resonance conditions (2.69), not only by diffraction divergences but also with the waveguide resonances. This can be clearly seen in Figure 2.10, where the total lattice sum has a richer structure and contains divergences due to the waveguide resonances and diffraction. The observed resonances indeed appear whenever the inverse polarisabilities become equal to the lattice sums.

2.4 Multicomponent lattices

Here, we briefly demonstrate how the scattering theory for a simple lattice can be generalised to describe multicomponent lattices that have more than one type of scatterer in each unit cell. Suppose we have n dipolar scatterer in the unit cell at the positions (relative to an arbitrarily chosen centre in the unit cell) $\mathbf{r}_\nu, \nu = 1, 2, ...n$. In a similar manner to that discussed for a simple lattice, we can write the induced dipole moment of the particle of type ν with polarisability α_ν as

$$\boldsymbol{\mu}_{\nu\boldsymbol{l}} = \overleftrightarrow{\alpha}_\nu\left[\mathbf{F}^{\text{inc}}(\mathbf{r}_{\nu\boldsymbol{l}}) + \sum_{\boldsymbol{l}'\neq\boldsymbol{l}}\overleftrightarrow{\mathcal{G}}^0(\mathbf{r}_{\nu\boldsymbol{l}}-\mathbf{r}_{\nu\boldsymbol{l}'})\boldsymbol{\mu}_{\nu\boldsymbol{l}'} + \sum_{\nu'\neq\nu}\sum_{\boldsymbol{l}'}\overleftrightarrow{\mathcal{G}}^0(\mathbf{r}_{\nu\boldsymbol{l}}-\mathbf{r}_{\nu'\boldsymbol{l}'})\boldsymbol{\mu}_{\nu\boldsymbol{l}'}\right]. \tag{2.71}$$

Using the translational invariance of the lattice, $\boldsymbol{\mu}_{\nu\boldsymbol{l}} = \boldsymbol{\mu}_\nu e^{i\mathbf{k}_\parallel \mathbf{R}_\nu}$, $\mathbf{F}^{\text{inc}}(\mathbf{r}_{\nu\boldsymbol{l}}) = \mathbf{F}^{\text{inc}}_\nu e^{i\mathbf{k}_\parallel \mathbf{R}_\nu}$ and the fact that

$$\mathbf{r}_{\nu\boldsymbol{l}} = \mathbf{R}_{\boldsymbol{l}} + \mathbf{r}_\nu, \quad \mathbf{r}_{\nu\boldsymbol{l}} - \mathbf{r}_{\nu\boldsymbol{l}'} = \mathbf{R}_{\boldsymbol{l}} - \mathbf{R}_{\boldsymbol{l}'}, \tag{2.72a}$$

$$\mathbf{r}_{\nu\boldsymbol{l}} - \mathbf{r}_{\nu'\boldsymbol{l}'} = \mathbf{R}_{\boldsymbol{l}} - \mathbf{R}_{\boldsymbol{l}'} + \mathbf{r}_\nu - \mathbf{r}_{\nu'} = \mathbf{R}_{\boldsymbol{l}} - \mathbf{R}_{\boldsymbol{l}'} + \mathbf{d}_{\nu\nu'}\,, \tag{2.72b}$$

where $\mathbf{R}_{\boldsymbol{l}} = l_1\mathbf{a}_1 + l_2\mathbf{a}_2$ is a lattice vector, with l_1 and l_2 being a pair of integers enumerating the sites of the lattice with primitive vectors $\mathbf{a}_1$ and $\mathbf{a}_2$, we can reduce equation (2.71) to the following form:

$$\boldsymbol{\mu}_\nu = \overleftrightarrow{\alpha}_\nu \left[\mathbf{F}^{\text{inc}}_\nu + \mathbf{G}^{\neq}(\mathbf{k}_\parallel)\boldsymbol{\mu}_\nu + \sum_{\nu'\neq\nu} \mathbf{G}(\mathbf{k}_\parallel, \mathbf{d}_{\nu\nu'})\boldsymbol{\mu}_{\nu'} \right], \tag{2.73}$$

where

$$\mathbf{G}^{\neq}(\mathbf{k}_\parallel) = \sum_{\boldsymbol{l}'\neq\boldsymbol{l}} \overleftrightarrow{\mathcal{G}}^0(\mathbf{R}_{\boldsymbol{l}} - \mathbf{R}_{\boldsymbol{l}'}) e^{i\mathbf{k}_\parallel(\mathbf{R}_{\boldsymbol{l}'} - \mathbf{R}_{\boldsymbol{l}})}, \tag{2.74a}$$

$$\mathbf{G}(\mathbf{k}_\parallel, \mathbf{d}_{\nu\nu'}) = \sum_{\boldsymbol{l}'} \overleftrightarrow{\mathcal{G}}^0(\mathbf{R}_{\boldsymbol{l}} - \mathbf{R}_{\boldsymbol{l}'} + \mathbf{d}_{\nu\nu'}) e^{i\mathbf{k}_\parallel(\mathbf{R}_{\boldsymbol{l}'} - \mathbf{R}_{\boldsymbol{l}})}\,. \tag{2.74b}$$

We can group and rewrite this equation in the following more compact form:

$$\sum_{\nu'} M_{\nu\nu'}\boldsymbol{\mu}_{\nu'} = \mathbf{F}^{\text{inc}}_\nu\,, \tag{2.75}$$

where the matrices $M_{\nu\nu'}$ are defined as

$$M_{\nu\nu'} = \begin{cases} \overleftrightarrow{\alpha}_\nu^{-1} - \mathbf{G}^{\neq}(\mathbf{k}_\parallel), & \nu = \nu' \\ -\mathbf{G}(\mathbf{k}_\parallel, \mathbf{d}_{\nu\nu'}), & \nu \neq \nu'\,. \end{cases} \tag{2.76}$$

Equation (2.75) can be recast in matrix form if we define a big matrix $\mathbf{M}$ with elements $M_{\nu\nu'}$, a column vector $\boldsymbol{\Pi} = \boldsymbol{\mu}_1, \boldsymbol{\mu}_2, ...\boldsymbol{\mu}_n$ and a column vector $\boldsymbol{\Phi}$ with elements $\mathbf{F}_\nu$, so that

$$\mathbf{M}\boldsymbol{\Pi} = \boldsymbol{\Phi}\,. \tag{2.77}$$

After calculating the induced dipole moments we can obtain the scattered field in a similar manner to that discussed for simple lattices

$$\mathbf{F}(\mathbf{r}) = \sum_\nu \sum_{\boldsymbol{l}} \overleftrightarrow{\mathcal{G}}^0(\mathbf{r} - \mathbf{r}_\nu - \mathbf{R}_{\boldsymbol{l}}) e^{i\mathbf{k}_\parallel \mathbf{R}_{\boldsymbol{l}}} \boldsymbol{\mu}_\nu\,. \tag{2.78}$$

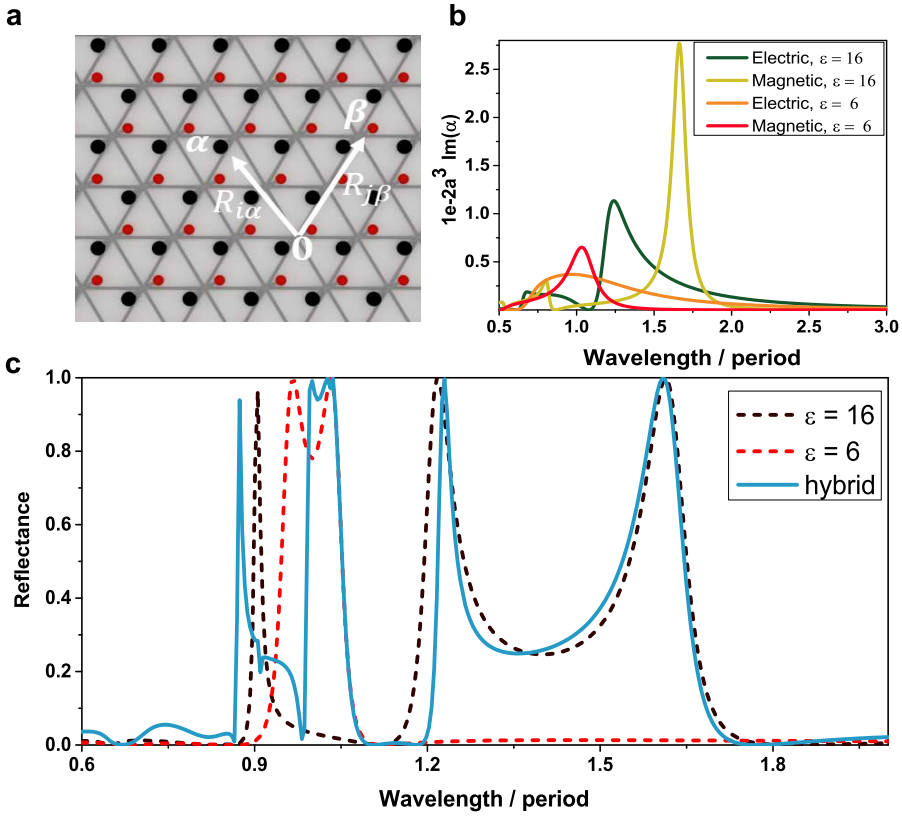

Figure 2.11: Reflection resonances and resonance hybridization in multicomponent lattices. (a) Schematic representation of multicomponent lattice with a single cell containing two distinct scatterers with polarisabilities α and β. (b) Wavelength dependence of the imaginary parts of the polarisabilites for the constituent particles. Both scatterers are spherical particles with dielectric constants equal to 6 and 16, respectively. (c) Reflectance plots for 2D square lattice of spheres with dielectric constant $\varepsilon_{sp} = 6.0$ (dashed red curve), and $\varepsilon_{sp} = 16.0$ (dashed black curve) and hybrid structure with both of these particles and the same lattice structure (solid blue curve).

Following similar steps as the ones we discussed for simple lattices, we can represent the field as a sum over diffracted plane waves:

$$\mathbf{F}(\mathbf{R}, z) = \frac{2\pi i}{A} \sum_{\nu} \sum_{\mathbf{g}} \frac{1}{k_{z\mathbf{g}}} \mathbf{f}^{\pm}_{\nu\mathbf{g}} e^{i(\mathbf{k}_{\parallel}+\mathbf{g})(\mathbf{R}-\mathbf{R}_{\nu}) \pm i k_{z\mathbf{g}} |z - z_{\nu} - z_0|}, \qquad (2.79)$$

which in the far-field limit reduces to

$$\mathbf{F}(\mathbf{R},z)=\frac{2\pi i}{A}\sum_{\nu}\frac{1}{k_z}\mathbf{f}^{\pm}_{\nu\mathbf{k}_\parallel}e^{\mathbf{k}_\parallel(\mathbf{R}-\mathbf{R}_\nu)\pm ik_z|z-z_\nu-z_0|}\,. \tag{2.80}$$

This allows us to write, for the reflection coefficient,

$$r^a_s=\frac{2\pi i}{Ak_z}\sum_{\nu}\gamma^+_{s\nu}e^{i(\mathbf{k}\mathbf{R}_\nu+k_z|z_\nu|)}, \tag{2.81a}$$

$$r^a_p=\frac{2\pi i}{Ak_z}\sum_{\nu}\gamma^+_{p\nu}e^{i(\mathbf{k}\mathbf{R}_\nu+k_z|z_\nu|)}\,. \tag{2.81b}$$

In order to illustrate this model, we have calculated the reflectance of a lattice with just two distinct scatterers per unit cell. In this situation, equation (2.77) reduces to

$$\begin{bmatrix}\overleftrightarrow{\alpha}^{-1}-\mathbf{G}^{\neq}(\mathbf{k}_\parallel) & -\mathbf{G}(\mathbf{k}_\parallel,\mathbf{d}_{\alpha\beta})\\ -\mathbf{G}(\mathbf{k}_\parallel,-\mathbf{d}_{\alpha\beta}) & \overleftrightarrow{\beta}^{-1}-\mathbf{G}^{\neq}(\mathbf{k}_\parallel)\end{bmatrix}\begin{bmatrix}\boldsymbol{\mu}^{\alpha}\\ \boldsymbol{\mu}^{\beta}\end{bmatrix}=\begin{bmatrix}\mathbf{F}^{inc}_{\alpha}\\ \mathbf{F}^{inc}_{\beta}\end{bmatrix}\,, \tag{2.82}$$

which is a simple system of equations with 12 components of induced dipole moments and can be solved by means of direct matrix inversion. Using the resulting dipole moments, we can calculate the reflectance of the array from equations (2.81). We have calculated the reflectance of free-standing square lattices of spherical particles with dielectric constants $\varepsilon_{sp}=6.0$ and $\varepsilon_{sp}=16.0$ and a hybrid lattice with these particles in the unit cell as shown in Figure 2.11(c). We see that the hybrid lattice inherits reflection features of both lattices. The resonances are slightly shifted as compared to the initial lattice resonances. The reason for this is the interaction between the sub lattices.

2.5 Defect modes and random array scattering

In this section, we extend the dipolar scatterer model to study a lattice defect and its effect on the scattering properties of the lattice. The simplest defect that we discuss is when one of the lattice sites is occupied by a particle that has a different polarisability to the other particles in the lattice. In this case we again start from the self-consistent equations for the dipole moments in the array, which in this situation take the form

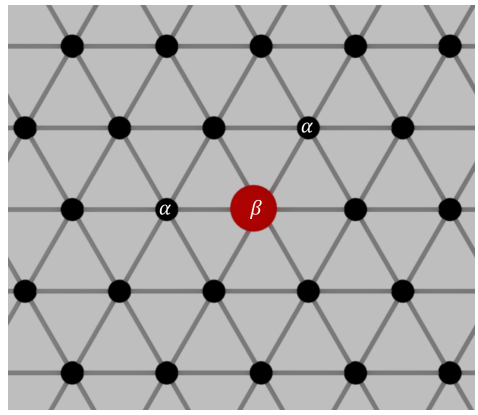

Figure 2.12: Schematic representation of a 2D lattice with a single defect in the centre.

$$\overleftrightarrow{\alpha}^{-1}\boldsymbol{\mu}_\mu - \sum_{\mu'\neq\mu} \overleftrightarrow{\mathcal{G}}^0_{\mu\mu'}\boldsymbol{\mu}_{\mu'} = \mathbf{F}^{inc}_\mu + \Delta_{\alpha,\beta}\mu_0\delta_{\mu,0}\,, \tag{2.83}$$

where $\Delta_{\alpha,\beta} = \overleftrightarrow{\alpha}^{-1} - \overleftrightarrow{\beta}^{-1}$. We can now use a Bloch mode expansion for the dipole moments of the array representing them as

$$\boldsymbol{\mu}_\mu = \sum_{\mathbf{q}} \boldsymbol{\mu}_q e^{i\mathbf{q}\cdot\mathbf{R}_\mu} = \frac{A}{(2\pi)^2}\int_{BZ} \boldsymbol{\mu}_q e^{i\mathbf{q}\cdot\mathbf{R}_\mu} d^2\mathbf{q}\,, \tag{2.84}$$

Using this and the fact that

$$\delta_{\mu,\nu} = \frac{A}{(2\pi)^2}\int_{BZ} e^{i\mathbf{q}\cdot(\mathbf{R}_\mu-\mathbf{R}_\nu)} d^2\mathbf{q}\,, \tag{2.85}$$

and also representing $\mathbf{F}^{inc}_\mu$ as

$$\mathbf{F}^{inc}_\mu = \sum_\nu \delta_{\mu,\nu}\mathbf{F}^{inc}_\nu = \frac{A}{(2\pi)^2}\int_{BZ}\sum_\nu \mathbf{F}_0 e^{i\mathbf{k}_\parallel\cdot\mathbf{R}_\nu} e^{i\mathbf{q}\cdot(\mathbf{R}_\mu-\mathbf{R}_\nu)} d^2\mathbf{q}\,, \tag{2.86}$$

we obtain

$$\big(I - \overleftrightarrow{\alpha}\mathbf{G}^{\neq}(\omega,\mathbf{q})\big)\boldsymbol{\mu}_\mathbf{q} = (I - \overleftrightarrow{\alpha}\overleftrightarrow{\beta}^{-1})\mu_0 + \overleftrightarrow{\alpha}\mathbf{F}^{inc}_0\sum_\nu e^{i(\mathbf{k}_\parallel+\mathbf{q})\cdot\mathbf{R}_\nu}\,. \tag{2.87}$$

This allows us to obtain the induced dipole moment at any site with position vector $\mathbf{R}_\mu$ as

$$\boldsymbol{\mu}_\mu = \frac{A}{(2\pi)^2}\int_{BZ} d^2\mathbf{q}\big[I - \overleftrightarrow{\alpha}\mathbf{G}^{\neq}(\omega,\mathbf{q})\big]^{-1}(I - \overleftrightarrow{\alpha}\overleftrightarrow{\beta}^{-1})e^{i\mathbf{q}\cdot\mathbf{R}_\mu}\mu_0 + \frac{A}{(2\pi)^2}\int_{BZ} d^2\mathbf{q}\big[I - \overleftrightarrow{\alpha}\mathbf{G}^{\neq}(\omega,\mathbf{q})\big]^{-1}\overleftrightarrow{\alpha}\mathbf{F}_0^{inc}e^{i\mathbf{q}\cdot\mathbf{R}_\mu}\sum_\nu e^{i(\mathbf{k}_\parallel-\mathbf{q})\cdot\mathbf{R}_\nu}\,. \quad (2.88)$$

Using the Poisson summation formula (2.39), we can express the sum over ν via a sum over reciprocal lattice vectors. If we also take into account the fact that $\mathbf{G}^{\neq}(\omega,\mathbf{q})$ is a periodic function of $\mathbf{q}$,

$$\mathbf{G}^{\neq}(\omega,\mathbf{q}+\mathbf{g}) = \mathbf{G}^{\neq}(\omega,\mathbf{q})\,, \quad (2.89)$$

we can extend the integration over the Brillouin zone to an integration over the whole 2D $\mathbf{q}$ space, which allows us to perform the integration analytically, resulting in

$$\frac{A}{(2\pi)^2}\int_{BZ} d^2\mathbf{q}\big[I - \overleftrightarrow{\alpha}\mathbf{G}^{\neq}(\omega,\mathbf{q})\big]^{-1}\overleftrightarrow{\alpha}\mathbf{F}_0^{inc}e^{i\mathbf{q}\cdot\mathbf{R}_\mu}\sum_\nu e^{i(\mathbf{k}_\parallel-\mathbf{q})\cdot\mathbf{R}_\nu} = \\ = \big[I - \overleftrightarrow{\alpha}\mathbf{G}^{\neq}(\omega,\mathbf{k}_\parallel)\big]^{-1}\overleftrightarrow{\alpha}\mathbf{F}_0^{inc}e^{i\mathbf{k}_\parallel\cdot\mathbf{R}_\mu}\,. \quad (2.90)$$

Using this, we finally have

$$\boldsymbol{\mu}_\mu = \frac{A}{(2\pi)^2}\int_{BZ} d^2\mathbf{q}\big[I - \overleftrightarrow{\alpha}\mathbf{G}^{\neq}(\omega,\mathbf{q})\big]^{-1}(I - \overleftrightarrow{\alpha}\overleftrightarrow{\beta}^{-1})e^{i\mathbf{q}\cdot\mathbf{R}_\mu}\mu_0 + \\ + \big[I - \overleftrightarrow{\alpha}\mathbf{G}^{\neq}(\omega,\mathbf{k}_\parallel)\big]^{-1}\overleftrightarrow{\alpha}\mathbf{F}_0^{inc}e^{i\mathbf{k}_\parallel\cdot\mathbf{R}_\mu}\,, \quad (2.91)$$

which can be written in a more compact way as

$$\boldsymbol{\mu}_\mu = \mathcal{L}(\mathbf{R}_\mu;\omega)(I - \overleftrightarrow{\alpha}\overleftrightarrow{\beta}^{-1})\mu_0 + \big[I - \overleftrightarrow{\alpha}\mathbf{G}^{\neq}(\omega,\mathbf{k}_\parallel)\big]^{-1}\overleftrightarrow{\alpha}\mathbf{F}_0^{inc}e^{i\mathbf{k}_\parallel\cdot\mathbf{R}_\mu}\,, \quad (2.92)$$

with

$$\mathcal{L}(\mathbf{R}_\mu;\omega) = \frac{A}{(2\pi)^2}\int_{BZ} d^2\mathbf{q}\big[I - \overleftrightarrow{\alpha}\mathbf{G}^{\neq}(\omega,\mathbf{q})\big]^{-1}e^{i\mathbf{q}\cdot\mathbf{R}_\mu}\,. \quad (2.93)$$

By taking $\mathbf{R}_\mu = \mathbf{R}_0$, we obtain for the defect particle

$$\mu_0 = \big[I - \mathcal{L}(0;\omega)(I - \overleftrightarrow{\alpha}\overleftrightarrow{\beta}^{-1})\big]^{-1}\big[I - \overleftrightarrow{\alpha}\mathbf{G}^{\neq}(\omega,\mathbf{k}_\parallel)\big]^{-1}\overleftrightarrow{\alpha}\mathbf{F}_0^{inc}\,. \quad (2.94)$$

Obviously, the existence of a defect resonance mode is given by the condition

$$\det\left[I - \mathcal{L}(0;\omega)(I - \overleftrightarrow{\alpha}\overleftrightarrow{\beta}^{-1})\right] = 0\,. \tag{2.95}$$

Note that, when the defect particles becomes identical to that of the perfect lattice, the multiplier to the right of the $\overleftrightarrow{\mathcal{L}}$ vanishes and we recover the correct form of the defect-free lattice dispersion. We can calculate the near fields in the array using the expressions (2.92) and (2.93),

$$\mathbf{F}(\mathbf{r}) = \frac{A}{(2\pi)^2}\int_{BZ} d^2\mathbf{q}\frac{\mathbf{G}(\omega,\mathbf{q};\mathbf{r})}{I - \overleftrightarrow{\alpha}\mathbf{G}^{\neq}(\omega,\mathbf{q})}(I-\overleftrightarrow{\alpha}\overleftrightarrow{\beta}^{-1})\mu_0+\frac{\mathbf{G}(\omega,\mathbf{k}_{\|};\mathbf{r})}{I - \overleftrightarrow{\alpha}\mathbf{G}^{\neq}(\omega,\mathbf{k}_{\|})}\overleftrightarrow{\alpha}\mathbf{F}_0^{inc}\,. \tag{2.96}$$

We used the formula (2.92) to calculate the dipole moments, which are represented in Figure 2.13. Having at our disposal a method for calculating the scattering by a defect in the perfect lattice, one can use the so-called coherent potential approximation (CPA) to calculate the scattering of a random array. This is a well-known technique in the theory of solid state physics of alloys [45], which was used in the context of electrodynamic scattering theory in Ref. [46, 47] and was later developed further by several authors to include various effects such as substrate [48, 49] and particle distribution [50–52]. In essence, this method replaces the true, partially filled lattice by an equivalent, fully occupied, array of identical particles, which are characterised by a new effective polarisability $\overleftrightarrow{\alpha}$ [53]. In order to find this polarisability, one proceeds in two stages. Firstly, an exact expression is found for the induced dipole moment of a single particle with polarisability $\overleftrightarrow{\alpha}_0$ and surrounded by the 2D array of particles with polarisability $\overleftrightarrow{\alpha}$. We have already solved this problem and the induced dipole moment is given via equation (2.94). In the second step, the dipole moment $\boldsymbol{\mu}_0$ obtained above, multiplied by the concentration n_ρ of particles in the lattice, is made equal to the induced dipole moment of the particle in a fully occupied array of effective particles. Having in mind that an induced dipole moment in a fully occupied lattice is given by (2.28) and using the equation (2.92) for $\boldsymbol{\mu}_0$, the following self-consistent equation for the effective polarisability $\overleftrightarrow{\alpha}$ can be obtained:

$$\overleftrightarrow{\alpha} = \overleftrightarrow{\alpha}_0 - (1-n_\rho)\mathcal{L}^{-1}(0;\omega)\overleftrightarrow{\alpha}_0\,. \tag{2.97}$$

This equation cannot be solved analytically, but rather one has to adopt an iterative scheme to solve it [54]. This can be achieved as follows: as a first step, one can use $n_\rho\overleftrightarrow{\alpha}_0$ instead of α in the integral over BZ to find $\overleftrightarrow{\alpha}$. This step is then

repeated in order to find new successive values of $\overleftrightarrow{\alpha}$ using the previous estimates in the integral until the process converges.

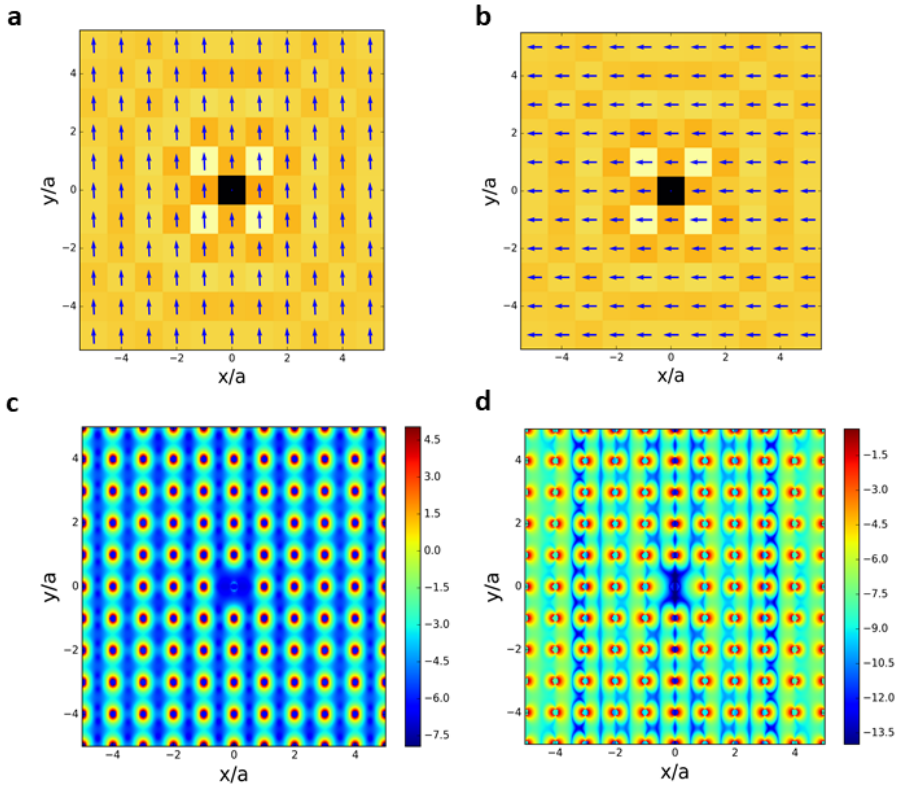

Figure 2.13: (a) Electric dipole moments at different sites of a square lattice .Arrows indicate the dipoles associated with a defect more, while the colour map represents the size of the dipoles. The dielectric function of the scatterers is taken to be equal to 16, while that of the defect particle is equal to 2. (b) Same as (a), but for magnetic dipole moments. (c) and (d) Electric and magnetic near-field distributions, respectively.

2.6 Decay and Emission

In the past few decades, single quantum emitters have become a useful tool for the development of new light sources, such as lasers, LEDs, and single-photon

sources for nano-electronic devices, as well as serving as nanoscopic probes and labels in chemistry and life sciences. The dynamical properties of emitters are correlated with their surrounding environment. In particular, the decay rates and the intrinsic transition frequencies depend on the LDOS associated with the electromagnetic environment. Since the latter is strongly dependent on the geometry and the optical properties of the objects surrounding the emitter, it is clear that appropriate choices for these two characteristics can lead to the enhancement or the suppression of the decay rates, as well as to frequency shifts of the transition energies with respect to their free-space values. In recent years, there has been a growing interest in emission-controlling designs exploiting plasmonic nanostructures [55, 56]. These designs are typically relying on a strongly localised EM field, which promotes strong field-emitter interaction. The surrounding environment can modify not only the temporal characteristic of the emitter, but also the spacial distribution. In particular, the directionality of the emission can be controlled by proper design of the surrounding structure [57]. In this context, periodic arrays of plasmonic nanoantennas are ideal candidates to realize such control over both the temporal (through the LDOS) and spatial (because incident light can only couple with certain diffraction modes) proprieties of the emitter.

In this section we briefly review a general approach for computing the decay rates and frequency shifts of emitters that are near a 2D array of dipole scatters. The emission of a dipole close to a 2D array of magnetoelectric scatterers have previously been discussed in Ref. [58] using the so-called phase-array approach [18]. However, we use another approach to derive an expression for the decay rate, which of course, yields identical results to those obtained in the paper by Lunnemann and Koenderink. We start by assuming that we have a 2D array of magnetoelectric scatterers with polarisabilities $\overleftrightarrow{\alpha}$ and a dipole emitter sitting at a point $\mathbf{r}_0$ near the lattice (see Figure 2.14(a)). The total fields produced by the emitter with dipole moments $\boldsymbol{\mu}_0 = [\mathbf{p}_0, \mathbf{m}_0]^T$ and the dipoles of the array are related by

$$\mathbf{F}(\mathbf{r}) = \overleftrightarrow{\mathcal{G}}^0(\mathbf{r} - \mathbf{r}_0)\boldsymbol{\mu}_0 + \sum_j \overleftrightarrow{\mathcal{G}}^0(\mathbf{r} - \mathbf{r}_j)\boldsymbol{\mu}_j \,, \tag{2.98}$$

where the induced dipole moments $\boldsymbol{\mu}_i$ at lattice site $\mathbf{r}_i$ can be given through the local fields,

$$\boldsymbol{\mu}_i = \overleftrightarrow{\alpha}\mathbf{F}(\mathbf{r}_i) \,. \tag{2.99}$$

Substituting this into the Eq. 2.98 gives a self-consistent equation for the fields,

$$\mathbf{F}(\mathbf{r}) = \overleftrightarrow{\mathcal{G}}^0(\mathbf{r}-\mathbf{r}_0)\boldsymbol{\mu}_0 + \sum_j \overleftrightarrow{\mathcal{G}}^0(\mathbf{r}-\mathbf{r}_j)\overleftrightarrow{\alpha}\mathbf{F}(\mathbf{r}_j)\,. \tag{2.100}$$

Specifying this equation for $\mathbf{r} = \mathbf{r}_1$, multiplying it by $e^{-i\mathbf{k}_\parallel\cdot\mathbf{R}_i}$ and summing it over i, we can obtain

$$\begin{aligned}\sum_i \mathbf{F}(\mathbf{r}_i)e^{-i\mathbf{k}_\parallel\cdot\mathbf{R}_i} = \sum_i \overleftrightarrow{\mathcal{G}}^0(\mathbf{r}_i-\mathbf{r}_0)e^{-i\mathbf{k}_\parallel\cdot\mathbf{R}_i}\boldsymbol{\mu}_0 + \\ + \sum_i\sum_j \overleftrightarrow{\mathcal{G}}^0(\mathbf{r}_i-\mathbf{r}_j)e^{-i\mathbf{k}_\parallel\cdot(\mathbf{R}_i-\mathbf{R}_j)}\overleftrightarrow{\alpha}\mathbf{F}(\mathbf{r}_j)e^{-i\mathbf{k}_\parallel\cdot\mathbf{R}_j}\,.\end{aligned} \tag{2.101}$$

If we now represent $\mathbf{F}(\mathbf{r}_i)$ as a sum over Bloch waves

$$\mathbf{F}(\mathbf{r}_i) = \sum_{\mathbf{q}} \mathbf{F}_{\mathbf{q}} e^{i\mathbf{q}\cdot\mathbf{R}_i} = \frac{A}{(2\pi)^2}\int_{BZ}\mathbf{F}_{\mathbf{q}}e^{i\mathbf{q}\cdot\mathbf{R}_i}\,, \tag{2.102}$$

with inverse transform given by

$$\mathbf{F}_{\mathbf{q}} = \sum_i \mathbf{F}(\mathbf{r}_i)e^{-i\mathbf{q}\cdot\mathbf{R}_i}\,, \tag{2.103}$$

then, from equation(2.101) and the lattice sums definitions we find

$$\mathbf{F}_{\mathbf{k}_\parallel} = \left[I - \mathbf{G}_0^{\neq}(\mathbf{k}_\parallel,\omega)\overleftrightarrow{\alpha}\right]^{-1}\mathbf{G}_0(\mathbf{k}_\parallel,\omega;-\mathbf{r}_0)\boldsymbol{\mu}_0\,, \tag{2.104}$$

where the radiation reaction term $i = j$ is absorbed into the $\overleftrightarrow{\alpha}$. The induced dipole moments follow from here directly as

$$\boldsymbol{\mu}_i = \frac{A}{(2\pi)^2}\int_{BZ}\frac{\overleftrightarrow{\alpha}e^{i\mathbf{q}\cdot\mathbf{R}_i}}{I-\mathbf{G}_0^{\neq}(\mathbf{q},\omega)\overleftrightarrow{\alpha}}\mathbf{G}_0(\mathbf{q},\omega;-\mathbf{r}_0)\boldsymbol{\mu}_0\,. \tag{2.105}$$

Thus, the fields become

$$\mathbf{F}(\mathbf{r}) = \overleftrightarrow{\mathcal{G}}^0(\mathbf{r}-\mathbf{r}_0)\boldsymbol{\mu}_0 + \frac{A}{(2\pi)^2}\int_{BZ}\mathbf{G}_0(\mathbf{q},\omega;\mathbf{r})\frac{\overleftrightarrow{\alpha}}{I-\mathbf{G}_0^{\neq}(\mathbf{q},\omega)\overleftrightarrow{\alpha}}\mathbf{G}_0(\mathbf{q},\omega;-\mathbf{r}_0)\boldsymbol{\mu}_0\,. \tag{2.106}$$

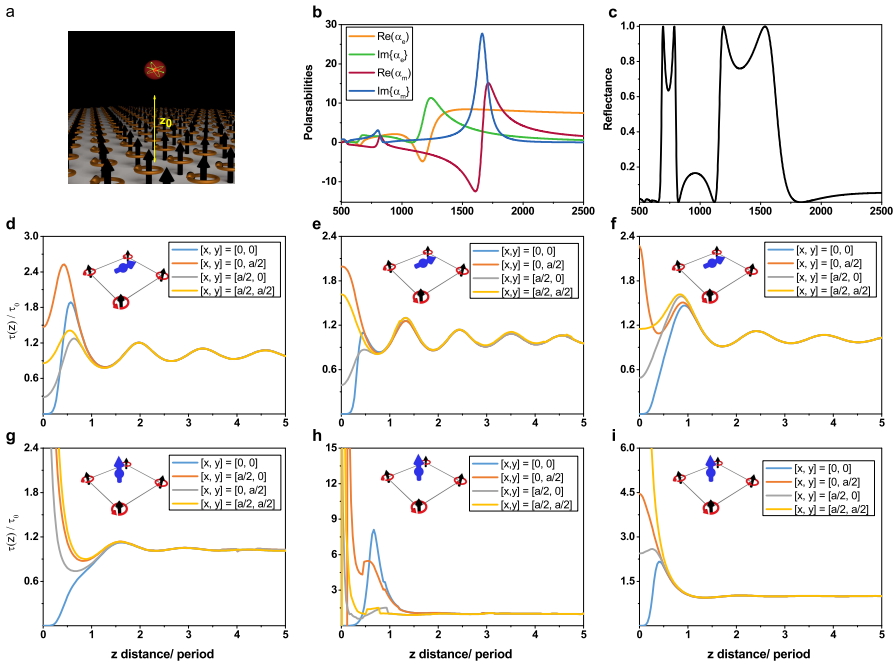

Figure 2.14: (a) Schematic representation of the emitter above a 2D array of magnetoelectric scatterers. (b) Real and imaginary parts of the electric and magnetic polarisabilities of the spheres. (c) Reflection spectrum of the array. (d), (e) and (f) Normalised lifetime of emitter with dipole moment pointing along x-*axis*. (g), (h) and (i) Same, but for a dipole moment pointing along the z-*axis*. (d) and (g) are calculated at a local electric field resonance wavelength, (e) and (h) at a magnetic field resonance wavelength, and (f) and (i) at the electric reflection resonance wavelength.

This equation gives in fact the dyadic Green function for the point source near the 2D lattice of magnetoelectric scatterers:

$$\overleftrightarrow{\mathcal{G}}(\mathbf{r}-\mathbf{r}_0) = \overleftrightarrow{\mathcal{G}}^0(\mathbf{r}-\mathbf{r}_0) + \overleftrightarrow{\mathcal{G}}^{sc}(\mathbf{r},\mathbf{r}_0)\,, \tag{2.107}$$

with the scattering or inhomogeneous part given by

$$\overleftrightarrow{\mathcal{G}}^{sc}(\mathbf{r},\mathbf{r}_0) = \frac{A}{(2\pi)^2}\int_{BZ}\mathbf{G}_0(\mathbf{q},\omega;\mathbf{r})\frac{\overleftrightarrow{\alpha}}{I-\mathbf{G}_0^{\neq}(\mathbf{q},\omega)\overleftrightarrow{\alpha}}\mathbf{G}_0(\mathbf{q},\omega;-\mathbf{r}_0)\,. \tag{2.108}$$

One can now readily obtain the decay rate of the emitter as in Ref. [59]:

$$\frac{\gamma(\mathbf{r}_0)}{\gamma_0} = 1 + \frac{3}{2k^3}\mathcal{I}m\left\{\boldsymbol{\mu}_0^{\dagger}\overleftrightarrow{\mathcal{G}}^{sc}(\mathbf{r}_0,\mathbf{r}_0)\boldsymbol{\mu}_0\right\}. \tag{2.109}$$

We have used this expression to calculate the decay rate of an emitter sitting above a 2D square array of spherical particles with a dielectric constant equal to $\varepsilon_{sp} = 16$. We normalize the decay rate to the value in free space. The sphere-radius to lattice period ratio is fixed at 0.2. We have carried out the calculations for two orientations of the emitter dipole moment, firstly assuming that it is pointing along the x-*axis* (parallel to the lattice plane), and secondly, along the z-*axis* (perpendicular to the lattice plane), and for three different wavelengths (see Figure 2.14). For each of these directions and wavelengths, we present calculations for four in-plane positions for the emitter in the unit cell, while sweeping the distance z from the lattice.

2.7 Conclusions

To summarise, we have presented a comprehensive theory for the scattering of a 2D array of magnetoelectric scatterers based on the point-dipole model. We have shown that despite its simplicity, it can capture the main optical properties of the array, giving a transparent connection between the observed results and its physical origins.

We discussed the scattering properties of a suspended array. Studied its reflection and dispersion characteristics. Furthermore, we demonstrated how the theory can be extended to also include arrays that are supported by a substrate or form a complex sandwiched structure.

Next, we demonstrated how multicomponent lattices can be described within the developed framework and how the resonances hybridise when one has more than one type of scatterer in the unit cell.

We discussed the properties of a lattice containing a point defect and showed how the method can be used to map the scattering properties of a 2D random array into an equivalent 2D periodic array with effective polarisabilities. We also showed the CPA to be an efficient way of finding these effective polarisabilities. Finally, we have discussed the emission characteristics of a dipolar emitter close to a 2D lattice of electromagnetic scatterers. In particular, we have demonstrated that the decay rate of the emitter can be calculated using the theoretical methods

developed at the beginning of this section. With all of these calculations we highlighted how useful such a theory can be, allowing one to describe various optical properties of 2D arrays in a very intuitive and physically transparent manner.

Bibliography

[1] R. W. Wood, "On a remarkable case of uneven distribution of light in a diffraction grating spectrum," *Proceedings of the Physical Society of London*, vol. 18, no. 1, p. 269, 1902.

[2] P. Yeh, A. Yariv, and C.-S. Hong, "Electromagnetic propagation in periodic stratified media. i. general theory," *JOSA*, vol. 67, no. 4, pp. 423–438, 1977.

[3] E. Yablonovitch and T. Gmitter, "Photonic band structure: The face-centered-cubic case," *Physical Review Letters*, vol. 63, no. 18, p. 1950, 1989.

[4] J. Joannopoulos, P. R. Villeneuve, and S. Fan, "Photonic crystals," *Solid State Communications*, vol. 102, no. 2, pp. 165–173, 1997.

[5] S. A. Maier, P. G. Kik, and H. A. Atwater, "Observation of coupled plasmon-polariton modes in au nanoparticle chain waveguides of different lengths: Estimation of waveguide loss," *Applied Physics Letters*, vol. 81, no. 9, pp. 1714–1716, 2002.

[6] A. F. Koenderink and A. Polman, "Complex response and polariton-like dispersion splitting in periodic metal nanoparticle chains," *Physical Review B*, vol. 74, no. 3, p. 033402, 2006.

[7] T. W. Ebbesen, H. J. Lezec, H. Ghaemi, T. Thio, and P. Wolff, "Extraordinary optical transmission through sub-wavelength hole arrays," *Nature*, vol. 391, no. 6668, pp. 667–669, 1998.

[8] H. Bethe, "Theory of diffraction by small holes," *Physical Review*, vol. 66, no. 7-8, p. 163, 1944.

[9] L. Martin-Moreno, F. Garcia-Vidal, H. Lezec, K. Pellerin, T. Thio, J. Pendry, and T. Ebbesen, "Theory of extraordinary optical transmission through subwavelength hole arrays," *Physical review letters*, vol. 86, no. 6, p. 1114, 2001.

[10] F. J. García de Abajo, J. Sáenz, I. Campillo, and J. Dolado, "Site and lattice resonances in metallic hole arrays," *Optics express*, vol. 14, no. 1, pp. 7–18, 2006.

[11] S. Enoch, R. Quidant, and G. Badenes, "Optical sensing based on plasmon coupling in nanoparticle arrays," *Optics express*, vol. 12, no. 15, pp. 3422–3427, 2004.

[12] A. Ameen, M. R. Gartia, A. Hsiao, T.-W. Chang, Z. Xu, and G. L. Liu, "Ultra-sensitive colorimetric plasmonic sensing and microfluidics for biofluid diagnostics using nanohole array," *Journal of Nanomaterials*, vol. 16, no. 1, p. 35, 2015.

[13] V. Flauraud, R. Regmi, P. M. Winkler, D. T. Alexander, H. Rigneault, N. F. v. Hulst, M. F. García-Parajo, J. Wenger, and J. Brugger, "In-plane plasmonic antenna arrays with surface nanogaps for giant fluorescence enhancement," *Nano Letters*, 2017.

[14] J. De Torres, M. Mivelle, S. B. Moparthi, H. Rigneault, N. F. Van Hulst, M. F. García-Parajó, E. Margeat, and J. Wenger, "Plasmonic nanoantennas enable forbidden fo?rster dipole–dipole energy transfer and enhance the fret efficiency," *Nano Letters*, vol. 16, no. 10, pp. 6222–6230, 2016.

[15] S. Yokogawa, S. P. Burgos, and H. A. Atwater, "Plasmonic color filters for cmos image sensor applications," *Nano Letters*, vol. 12, no. 8, pp. 4349–4354, 2012.

[16] Y. Gu, L. Zhang, J. K. Yang, S. P. Yeo, and C.-W. Qiu, "Color generation via subwavelength plasmonic nanostructures," *Nanoscale*, vol. 7, no. 15, pp. 6409–6419, 2015.

[17] J. Pendry, A. Holden, D. Robbins, and W. Stewart, "Low frequency plasmons in thin-wire structures," *Journal of Physics: Condensed Matter*, vol. 10, no. 22, p. 4785, 1998.

[18] F. Capolino, *Theory and phenomena of metamaterials*. CRC press, 2009.

[19] A. Krasnok, S. Makarov, M. Petrov, R. Savelev, P. Belov, and Y. Kivshar, "Towards all-dielectric metamaterials and nanophotonics," in *SPIE Optics+ Optoelectronics*. International Society for Optics and Photonics, 2015, pp. 950 203–950 203.

[20] S. Jahani and Z. Jacob, "All-dielectric metamaterials," *Nature nanotechnology*, vol. 11, no. 1, pp. 23–36, 2016.

[21] A. García-Etxarri, R. Gómez-Medina, L. S. Froufe-Pérez, C. López, L. Chantada, F. Scheffold, J. Aizpurua, M. Nieto-Vesperinas, and J. J. Sáenz, "Strong magnetic response of submicron silicon particles in the infrared," *Optics express*, vol. 19, no. 6, pp. 4815–4826, 2011.

[22] R. Gomez-Medina, B. García-Cámara, I. Suárez-Lacalle, F. González, F. Moreno, M. Nieto-Vesperinas, and J. J. Sáenz, "Electric and magnetic dipolar response of germanium nanospheres: interference effects, scattering anisotropy, and optical forces," *Journal of Nanophotonics*, vol. 5, no. 1, pp. 053 512–053 512, 2011.

[23] A. B. Evlyukhin, S. M. Novikov, U. Zywietz, R. L. Eriksen, C. Reinhardt, S. I. Bozhevolnyi, and B. N. Chichkov, "Demonstration of magnetic dipole resonances of dielectric nanospheres in the visible region," *Nano letters*, vol. 12, no. 7, pp. 3749–3755, 2012.

[24] F. J. García de Abajo, "Colloquium: Light scattering by particle and hole arrays," *Reviews of Modern Physics*, vol. 79, no. 4, p. 1267, 2007.

[25] A. L. Fructos, S. Campione, F. Capolino, and F. Mesa, "Characterization of complex plasmonic modes in two-dimensional periodic arrays of metal nanospheres," *JOSA B*, vol. 28, no. 6, pp. 1446–1458, 2011.

[26] I. Sersic, M. Frimmer, E. Verhagen, and A. F. Koenderink, "Electric and magnetic dipole coupling in near-infrared split-ring metamaterial arrays," *Physical review letters*, vol. 103, no. 21, p. 213902, 2009.

[27] I. Sersic, C. Tuambilangana, T. Kampfrath, and A. F. Koenderink, "Magnetoelectric point scattering theory for metamaterial scatterers," *Physical Review B*, vol. 83, no. 24, p. 245102, 2011.

[28] P. Lunnemann and A. F. Koenderink, "Dispersion of guided modes in two-dimensional split ring lattices," *Physical Review B*, vol. 90, no. 24, p. 245416, 2014.

[29] A. D. Yaghjian, "Electric dyadic green's functions in the source region," *Proceedings of the IEEE*, vol. 68, no. 2, pp. 248–263, 1980.

[30] C.-T. Tai, *Dyadic Green functions in electromagnetic theory*. Institute of Electrical & Electronics Engineers (IEEE), 1994.

[31] O. Keller, *Quantum theory of near-field electrodynamics*. Springer Science & Business Media, 2012.

[32] ——, "Local fields in the electrodynamics of mesoscopic media," *Physics Reports*, vol. 268, no. 2, pp. 85–262, 1996.

[33] L. B. Felsen and N. Marcuvitz, *Radiation and scattering of waves*. John Wiley & Sons, 1994, vol. 31.

[34] P. Lunnemann, I. Sersic, and A. F. Koenderink, "Optical properties of two-dimensional magnetoelectric point scattering lattices," *Physical Review B*, vol. 88, no. 24, p. 245109, 2013.

[35] P. P. Ewald, "Ewald summation," *Ann. Phys.*, vol. 64, pp. 253–371, 1921.

[36] ——, "Die berechnung optischer und elektrostatischer gitterpotentiale," *Annalen der Physik*, vol. 369, no. 3, pp. 253–287, 1921.

[37] C. M. Linton, "Lattice sums for the helmholtz equation," *SIAM review*, vol. 52, no. 4, pp. 630–674, 2010.

[38] A. Moroz, "Quasi-periodic green's functions of the helmholtz and laplace equations," *Journal of Physics A: Mathematical and General*, vol. 39, no. 36, p. 11247, 2006.

[39] H. Weyl *et al.*, "The propagation of electromagnetic waves over a plane conductor," *Ann. der Phys*, vol. 60, pp. 481–500, 1919.

[40] G. Mie, "Beiträge zur optik trüber medien, speziell kolloidaler metallösungen," *Annalen der physik*, vol. 330, no. 3, pp. 377–445, 1908.

[41] A. Modinos, "Scattering of electromagnetic waves by a plane of spheres-formalism," *Physica A: Statistical Mechanics and its Applications*, vol. 141, no. 2-3, pp. 575–588, 1987.

[42] N. Stefanou and A. Modinos, "Impurity bands in photonic insulators," *Physical Review B*, vol. 57, no. 19, p. 12127, 1998.

[43] N. Stefanou, V. Yannopapas, and A. Modinos, "Multem 2: A new version of the program for transmission and band-structure calculations of photonic crystals," *Computer physics communications*, vol. 132, no. 1, pp. 189–196, 2000.

[44] B. Auguié, X. M. Bendana, W. L. Barnes, and F. J. García de Abajo, "Diffractive arrays of gold nanoparticles near an interface: Critical role of the substrate," *Physical Review B*, vol. 82, no. 15, p. 155447, 2010.

[45] P. Soven, "Coherent-potential model of substitutional disordered alloys," *Physical Review*, vol. 156, no. 3, p. 809, 1967.

[46] B. Persson and R. Ryberg, "Vibrational interaction between molecules adsorbed on a metal surface: The dipole-dipole interaction," *Physical Review B*, vol. 24, no. 12, p. 6954, 1981.

[47] B. Persson and A. Liebsch, "Optical properties of two-dimensional systems of randomly distributed particles," *Physical Review B*, vol. 28, no. 8, p. 4247, 1983.

[48] A. Bagchi, R. G. Barrera, and B. B. Dasgupta, "Classical local-field effect in reflectance from adsorbed overlayers," *Physical Review Letters*, vol. 44, no. 22, p. 1475, 1980.

[49] A. Bagchi, R. G. Barrera, and R. Fuchs, "Local-field effect in optical reflectance from adsorbed overlayers," *Physical Review B*, vol. 25, no. 12, p. 7086, 1982.

[50] R. G. Barrera, G. Monsivais, and W. L. Mochán, "Renormalized polarizability in the maxwell garnett theory," *Physical Review B*, vol. 38, no. 8, p. 5371, 1988.

[51] R. G. Barrera, P. Villasenor-Gonzalez, W. L. Mochán, and G. Monsivais, "Effective dielectric response of polydispersed composites," *Physical Review B*, vol. 41, no. 11, p. 7370, 1990.

[52] R. G. Barrera, M. del Castillo-Mussot, G. Monsivais, P. Villaseor, and W. L. Mochán, "Optical properties of two-dimensional disordered systems on a substrate," *Physical Review B*, vol. 43, no. 17, p. 13819, 1991.

[53] A. Modinos, V. Yannopapas, and N. Stefanou, "Scattering of electromagnetic waves by nearly periodic structures," *Physical Review B*, vol. 61, no. 12, p. 8099, 2000.

[54] P. Johansson, "Light scattering from disordered overlayers of metallic nanoparticles," *Physical Review B*, vol. 64, no. 16, p. 165405, 2001.

[55] R. Carminati, J.-J. Greffet, C. Henkel, and J. Vigoureux, "Radiative and non-radiative decay of a single molecule close to a metallic nanoparticle," *Optics Communications*, vol. 261, no. 2, pp. 368–375, 2006.

[56] L. Blanco and F. J. García de Abajo, "Spontaneous light emission in complex nanostructures," *Physical Review B*, vol. 69, no. 20, p. 205414, 2004.

[57] T. H. Taminiau, F. D. Stefani, and N. F. van Hulst, "Enhanced directional excitation and emission of single emitters by a nano-optical yagi-uda antenna," *Optics express*, vol. 16, no. 14, pp. 10 858–10 866, 2008.

[58] P. Lunnemann and A. F. Koenderink, "The local density of optical states of a metasurface," *Scientific reports*, vol. 6, 2016.

[59] L. Novotny and B. Hecht, *Principles of nano-optics*. Cambridge university press, 2012.

Chapter 3

Ultrafast and broadband tuning of resonant optical nanostructures

As we mention previously, plasmons have been shown to play an important role in the phenomenon of extraordinary optical transmission (EOT) through periodic arrays of nanoholes (NH) patterned in metallic films. Resonances in the transmitted spectrum have been attributed to resonant interactions between holes mediated by surface plasmons [1], and can be easily explained in terms of collective interactions in the periodic lattice [2–4] using dipole scatterer models.

One of the main challenges in the design of these plasmonic nanostructures is the precise control of their optical properties. This can be achieved by an appropriate choice of the materials and geometries. However, this approach is static and limited by material inhomogeneities and fabrication tolerances. Due to the high sensitivity of surface plasmons to local variations in the refractive index, other approaches have been based on the use of active materials whose refractive indices can be changed using an external stimulus, for instance using quantum dots [5] or liquid crystals [6].

In this chapter, we introduce different designs combining thin films of $Ge_2Sb_2Te_5$ (GST) with arrays of NHs patterned in Au films and demonstrate their capability to obtain broadband and ultrafast tuning of transmission resonances both in the visible and near-infrared (NIR) spectral regions. Specifically the purpose of this chapter is twofold. On the one hand, we show large wavelength and amplitude

tuning of the EOT resonances based on a GST phase transition. This effect is explored for three different geometries, obtaining resonance wavelength shifts as large as 385 nm, an order of magnitude higher than previously reported [6]. On the other hand, we demonstrate ultrafast tuning of the EOT resonances in the ps regime based on changes in the resonant bond polarisability of GST [7]. This is achieved without the need of a phase transition, thus making the process reversible and overcoming the limit imposed by the cycleability of the GST.

3.1 Optical properties of GST

Phase change materials (PCMs) are solids characterised by an unconventional combination of properties. The amorphous and crystalline phases of these materials possess significantly different optical properties. GST is an example of a phase change material and is simply a ternary semiconductor alloy that can have more than one stable phase with very large contrast in its optical and electrical properties [8]. In Figure 3.1 we plotted the refractive indices and extinction coefficients of amorphous and crystalline GST in the visible and NIR wavelength ranges. The data were fitted from experimental reflection and transmission spectra for a GST thin film deposited on glass substrate. We can see that there is, indeed, a huge contrast in the optical properties between these phases. In the visible, both phases are absorptive, whereas in the NIR the amorphous phase become transparent while the crystalline phase still remains absorptive, although the absorption is significantly decreased.

When PCMs and metallic nanostructures supporting SPPs are properly coupled, the large changes in the optical constants associated with the metal–insulator transition can be used to efficiently tune resonances. Phase transitions in PCMs can be externally driven by varying the temperature or by applying electrical or optical pulses. Importantly, these transitions can occur on the nanosecond timescale [7, 9], while the resulting phase is remarkably stable for several years [9]. Besides the widespread use of PCMs in optical storage media [10] and phase-change random access memories [11], these properties also make them suitable for nanophotonics, where several applications have already been demonstrated [12–15]. Additionally, their capability to retain their state after a phase transition offers an opportunity to design novel reconfigurable optical elements.

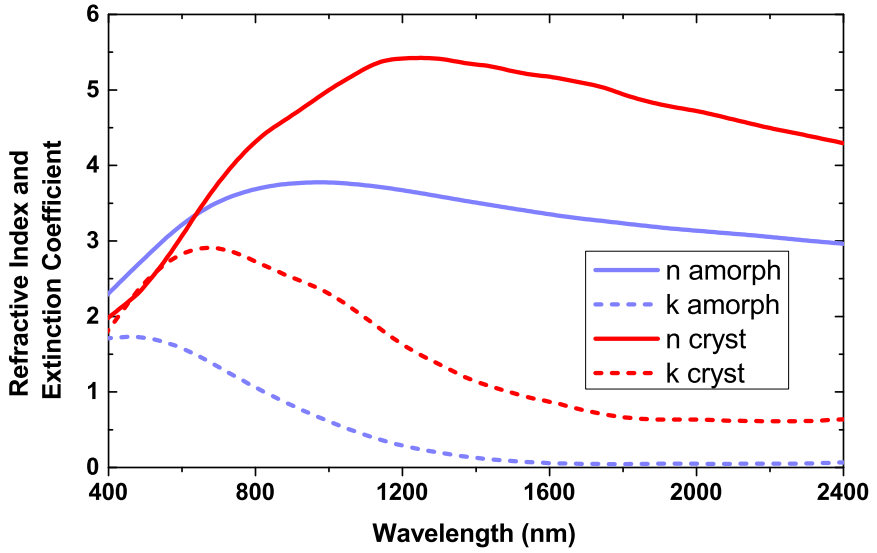

Figure 3.1: The refractive indices (n, solid curves) and extinction coefficients (k, dashed curves) for amorphous (blue) and crystalline (red) phases of GST.

3.2 Au NH array with GST inside the holes

The first device consists of a hexagonal NH array patterned on top of a 40 nm thick Au film. A 20 nm GST film is deposited both on top of the Au film and inside the NH, as shown in Figure 3.3a). The hole diameter (d) is 250 nm and the period of the hexagonal lattice (a) is 470 nm.

3.2.1 Device fabrication

The device was fabricated on top of a fused SiO_2 substrate using colloidal lithography. A 50 μL solution of polystyrene (PS) beads (10 % concentration), with a nominal diameter of 470 nm, was mixed in ethanol at a 1:1 volume ratio, and placed in an ultrasonic bath for 30 minutes. A laminar flow of the prepared solution was then created on the surface of distilled water using a curved pipette with its tip placed just above the water surface.

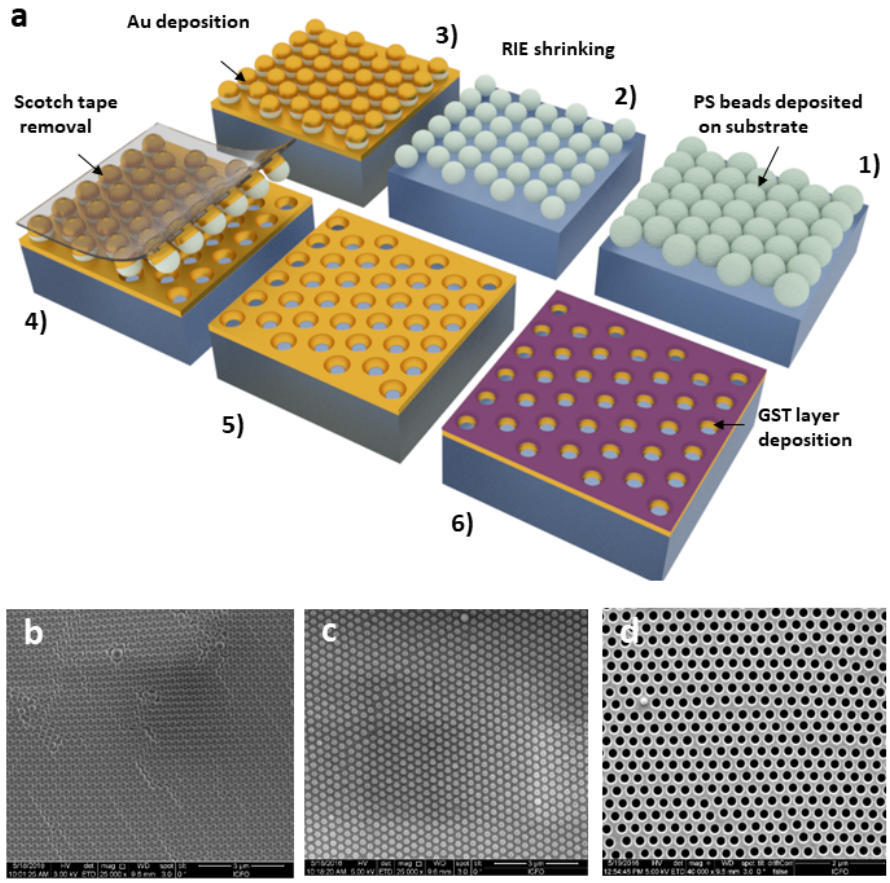

Figure 3.2: Nanosphere lithography steps used to fabricate the hole array in metal film. (a) Schematic representation of the fabrication steps (order is as numbered). (b) to (d) SEM images for: (b) close packed array of polystyrene beads, (c) PB's after RIE shrinking and (d) nanohole array after removal of PBs.

The water was contained in a small box where the SiO_2 substrate had been previously immersed. After a few minutes, the water surface was fully covered by a polycrystalline monolayer of hexagonally packed PS beads and, upon removal of the distilled water, the monolayer was deposited on top of the substrate. Then the PS beads were shrunk down to a diameter of 250 nm by reactive ion

etching (RIE) using O_2 plasma for 4'15" at 100 W. A 5 nm Ti adhesion layer and a 40 nm Au layer were then thermally evaporated on top. This was followed by the removal of the PS beads with scotch tape before depositing the 20 nm GST layer by RF co-sputtering(see Figure 3.2(a) for a schematic representation of this process). The SEM images of the sample at different steps of the fabrication process are given in Figures 3.2(b)- (d).

3.2.2 Transmission measurements

Transmission measurements were performed at normal incidence for wavelengths between 300 and 2400 nm in a commercial spectrophotometer using a wavelength step of 5 nm and a rectangular beam of 3×8 mm^2.

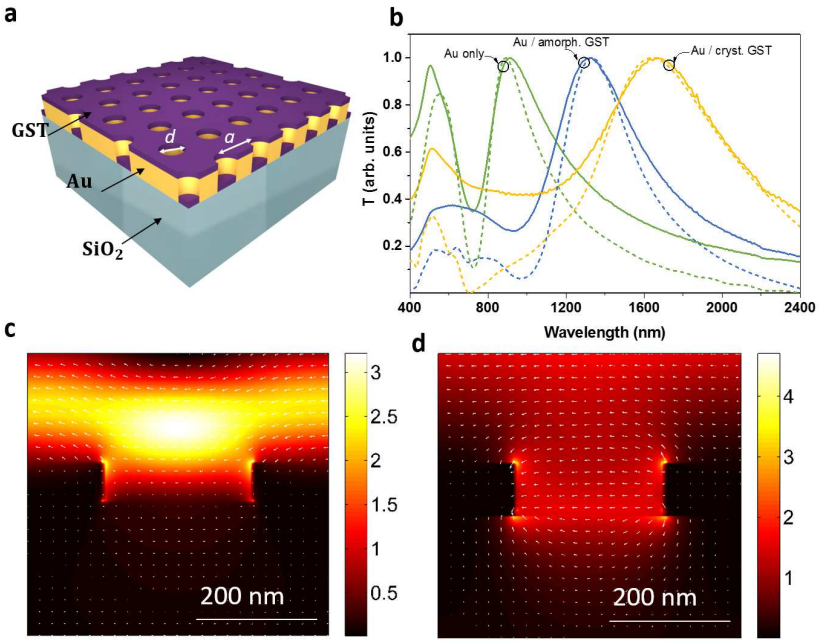

Figure 3.3: (a) Schematic of the NH array with GST inside the holes, (b) Transmission spectra for Au only (green curves), Au with amorphous GST (blue curves) and Au with crystalline GST (orange curves). The dashed curves are corresponding transmission spectra obtained from FDTD numerical simulation. Near field distributions around the hole for (c) off-resonance and (d) resonance wavelengths, respectively.

Figure 3.3(b) shows the transmission spectrum of the device both for the amorphous (blue curve) and the crystalline (orange curve) GST. The transmission of an Au NH array without GST is also shown as a reference (green curve). A peak in transmission associated with EOT can be clearly seen in all cases. The transition between amorphous and crystalline GST was triggered by heating the sample on a hot plate at 200 ^{o}C. Heating for about 1 minute was sufficient to completely crystallize the film, and no further changes in the spectrum were observed after subsequent thermal treatments. After crystallisation, the initial resonance wavelength λ^{a}_{res} = 1330 nm is redshifted by 385 nm (λ^{c}_{res} = 1715 nm) due to the change in the optical constants of the GST. This was confirmed by FDTD simulations of the same structure, shown in Figure 3.3(b) as dashed curves. The simulated electric field distribution on- and off- resonance when the GST is in the crystalline phase is shown in Figures 3.3(c) and (d). The electric field distribution supports the idea that the GST modifies the SPPs in the NH array.

3.2.3 Ultrafast response of the NH array

This device was also used to investigate changes in EOT resonances via optical pumping associated with the ultrafast and reversible dynamics of the resonant bond polarisability. It is known that for pump fluences below the threshold required to reamorphise, GST is capable of transiently and rapidly acquiring values of the dielectric function close to those of the amorphous state without completing the phase-transition [7]. Moreover this effect takes place in the ultrafast timescale (ps) and is reversible.

For this purpose, a pump-probe experiment was performed. Starting with crystalline GST, 35 fs pump pulses at 800 nm with a fluence of 5 mJ·cm^{-2} were used to pump the sample with a repetition rate of 80 Hz. The reduced repetition rate was needed in order to avoid cumulative heating of the sample, which could lead to reamorphisation of the GST film. Then, infrared pulses with a duration of 60 fs, generated in an optical parametric amplifier, measured the transmission of the sample at different time delays and for wavelengths between 1150 and 2150 nm in 100 nm spectral steps. The transmitted light was collected as a function of probe delay using a photodiode and lock-in detection. The time-resolved evolution of the transmitted spectrum during the initial 3 ps is shown in Figure 3.4.

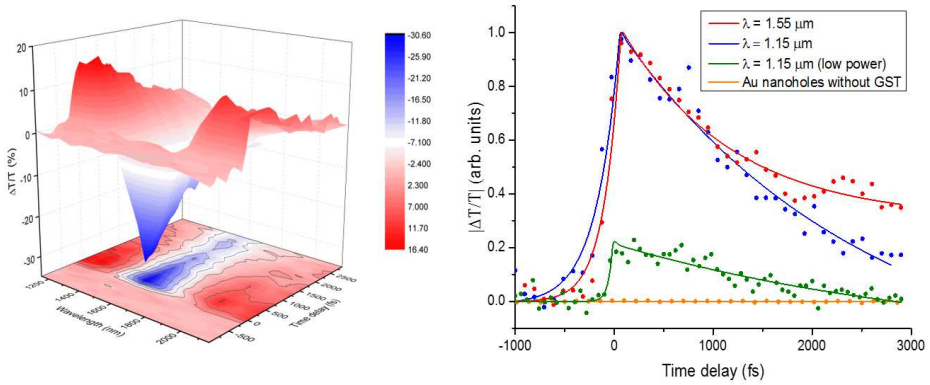

Figure 3.4: (a) Time response of the NH array between λ = 1150 and 2100 nm during the initial 3 ps. (b) Normalised time response at λ = 1550 nm (red circles) and λ = 1150 nm (blue circles), using a pump fluence of 5 mJ·cm^{-2}. For lower pump fluences (F = 1.5 mJ·cm^{-2}, green circles), the sample shows the same behaviour with a smaller modulation. The time response of a bare Au NH array is also shown at λ = 1150 nm (orange circles).

In order to verify that this response is due to the GST, we also performed the same pump-probe experiment using a bare Au NH array, confirming that pumping the bare Au sample does not modify the transmission, as shown in Figure 3.4(b) (orange circles). At telecom wavelengths the sample containing GST shows a decrease in transmission due to the ultrafast change in the dielectric function of the GST. The modulation is fast, reaching a peak value in 100 fs (resolution limited) and recovering after a few ps. Furthermore, the magnitude of the modulation is already $>$ 30 % for modest excitation power.

The origin of this modulation is a transient change in the dielectric function in the ps timescale [7]. In this case, it has been shown that the dielectric function achieves values which are close to, but not equal to, those of the stable amorphous phase. Thus, a new resonant feature arises in this regime which does not need to be the same as in the static case. This can be clearly seen, for instance, at λ = 1550 nm, where the change is positive in the static case and negative in the ultrafast regime. One would need a complete characterisation of the dielectric function of the sample in the IR region probed here in order to give a definitive statement about the origin of the positive signals appearing at other wavelengths.

Most likely, these signals arise from a combination of the change in the dielectric function, a transient increase in carriers induced by the pump pulse, phonon contributions and the effects of nanostructuring [9].

3.3 Au NH array without GST in the holes

After investigation of the first device, a second was designed and fabricated, consisting of an Au NH array with the same geometry but without GST inside the holes. The fabrication procedure was identical except that, in this case, the PS beads were removed after deposition of the GST layer. The experimental transmission spectrum for the amorphous and crystalline GST is shown in Figure 3.5(a).

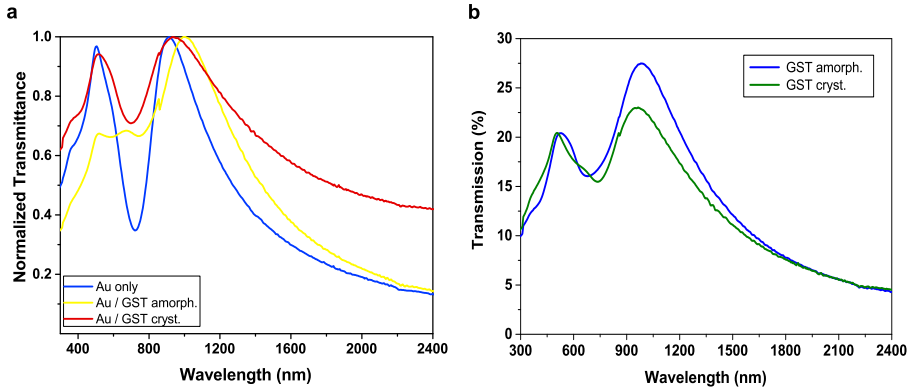

Figure 3.5: (a) Experimental transmission spectrum of the NH array without GST (blue curve), with amorphous (yellow curve) and crystalline (red curve) GST when the GST is only present on top of the Au surface. (b) Real scale transmission of the structure for amorphous GST (blue curve) and after crystallisation by applying an electrical current (green curve).

In this sample, the amorphous to crystalline phase transition, which was again triggered by heating the sample on a hot plate at 200 ^{o}C for 1 minute, produces a resonance wavelength blueshift of 35 nm. The transmission of the NH array slightly decreases from 28 % to 24 %.

Moreover, this sample was also used to demonstrate electrical tuning of the optical transmission by electrically triggering a phase transition in the GST layer.

Using two lateral 40 nm thick Au films as planar contact electrodes and applying a DC current (V_c = 3.5 V; I_c = 1.5 A), the GST layer crystallised in approximately 20 s due to Joule heating of the Au film underneath the GST, which increased its temperature above the crystallisation temperature. Subsequent application of the same DC current did not change the transmission furthermore, indicating that the GST layer had been completely crystallised. The effect of this electrically triggered phase transition on the transmitted spectrum is shown in Figure 3.5(b). The measurements confirm that this effect is similar to the previous case, producing a blue shift of 35 nm and a decrease in the transmission from 33 % to 26 %.

3.4 Au NH array in an Si_3N_4 membrane

For certain applications, it is desirable to have narrower resonances than for those of the two devices presented previously, whose values are on the order of hundreds of nm, mainly due to the polycrystalline structure of the PS beads used to fabricate them.

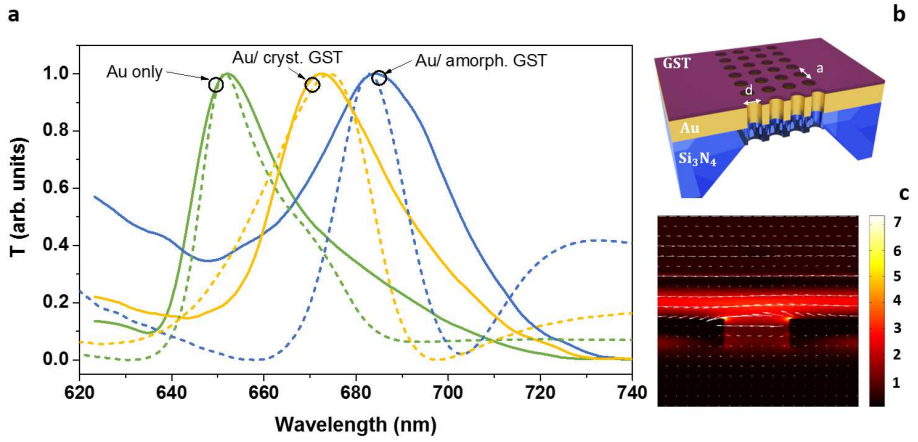

Figure 3.6: (a) Experimental (solid lines) and simulated (dashed curves) normalised transmission of the NH array suspended on a Si_3N_4 membrane both without GST (green curve) and with GST in the amorphous (blue curve) and crystalline (orange curve) phases. (b) Schematic of a NH array on an Si_3N_4 membrane. (c) the near field distribution at resonance.

For this purpose, a third device was investigated, consisting of a periodic NH array perforated in a 100 nm free-standing Si_3N_4 membrane covered with a 125 nm thick Au film and a 10 nm GST film, as shown in Figure 3.6(b). The device was fabricated at EPFL using a combination of deep ultraviolet lithography and RIE, as described in ref. [6]. This method was used to pattern a square lattice of NHs with a period of a = 600 nm and a diameter of d = 200 nm, which displays much sharper resonances in the transmission spectrum. Optical characterisation of this sample was performed via spectroscopic measurements using an unpolarised broadband white light source. Transmitted light from the device was collected by a high-magnification objective lens (100x Nikon objective lens with NA of 0.6 embedded in a Nikon Eclipse-Ti microscope) coupled with an optical fibre and recorded with a Maya 2000Pro spectrometer. The transmission measurements are shown in Figure 3.6(a) as solid lines.

In this case, the wavelength range and the resonance bandwidths are respectively about 20 and 10 times smaller than those of the NH array with GST inside the holes. Crystallisation of this sample induces a blue shift of 13 nm in the resonance wavelength, due to the smaller thickness of the GST layer (10 nm). Again, the measured values were confirmed by FDTD simulations, as shown in Figure 3.6(a) by corresponding dashed lines.

3.5 Physical origin of the change in the transmission spectrum

Although the FDTD simulations are in good agreement with the experiment not much can be inferred from these simulations about the physical origins of the changes upon transitions between amorphous and crystalline phases. One can gain further insight into the effect of a GST phase transition on the EOT resonances through a qualitative description of the sample using a semi-analytical model that describes the interaction of light with the nanostructured surface following the discussion line originally presented by [16]. For diameters and periods smaller than the wavelength, light transmission through NH arrays in metallic films can be modelled in terms of equivalent induced electric ($\mathbf{p}_1$, $\mathbf{p}_2$) and magnetic ($\mathbf{m}_1$, $\mathbf{m}_2$) dipoles on each side of the film as depicted in Figure 3.7(a) [16, 17].

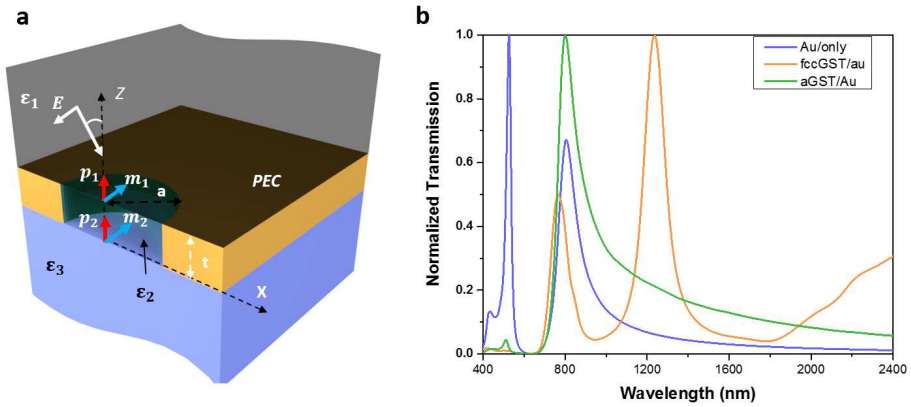

Figure 3.7: (a) Schematic for induced electric and magnetic dipole moments of hole apertures drilled in PEC film. (b) Analytically calculated transmission curves for hole array with period 470nm, film thickness 45nm and hole aperture diameter 250nm.

To simplify the modelling, we assume that the holes are drilled in a perfect electric conductor (PEC) film instead of a real metal film. This will have little effect on the optical properties as long as the skin depth for the frequency range of interest is small compared to the hole diameter and the thickness of the film. Moreover, one can introduce corrections due to finiteness of the skin depth, later, by properly normalising the polarisabilities of the hole obtained within this model. With this in mind we can write the following set of coupled equations for induced electric and magnetic dipole moments on the upper and lower apertures:

$$\begin{aligned}
\mathbf{p}_1 &= \alpha_{ee}^{\uparrow\uparrow}(\mathbf{E}^{inc} + G_1\mathbf{p}_1 + H_1\mathbf{m}_1) + \alpha_{ee}^{\uparrow\downarrow}(G_2\mathbf{p}_2 + H_2\mathbf{m}_2),\\
\mathbf{m}_1 &= \alpha_{mm}^{\uparrow\uparrow}(\mathbf{H}^{inc} - H_1\mathbf{p}^1 + G^1\mathbf{m}_1) + \alpha_{mm}^{\uparrow\downarrow}(-H_2\mathbf{p}_2 + G_2\mathbf{m}_2),\\
\mathbf{p}_2 &= \alpha_{ee}^{\downarrow\uparrow}(G_1\mathbf{p}_1 + H_1\mathbf{m}_1) + \alpha_{ee}^{\downarrow\downarrow}(G_2\mathbf{p}_2 + H_2\mathbf{m}_2),\\
\mathbf{m}_2 &= \alpha_{mm}^{\downarrow\uparrow}(-H_1\mathbf{p}_1 + G_1\mathbf{m}_1) + \alpha_{mm}^{\downarrow\downarrow}(-H_2\mathbf{p}_2 + G_2\mathbf{m}_2)\,.
\end{aligned} \tag{3.1}$$

where G_1, H_1 and G_2, H_2 are the total lattice sums (2.32) at the upper and lower apertures of the hole, respectively. The arrows in the superscripts of the polarisability tensors indicate whether it is for the top (up arrow) or the bottom (down arrow) aperture of the hole. The second arrow in the pair, indicates the direction of the incidence wave (if it is from upper side or lower side of the

hole). The PEC boundary conditions imply that the incident field can excite only perpendicular electric and parallel magnetic dipole moments on the aperture of the hole. Thus, we can assume that the electric $\alpha_{zz}^{ee} = \alpha_e$ and magnetic $\alpha_{yy}^{mm} = \alpha_m$ components are the only ones that are non-vanishing. This allows us to reduce the equations above to the following 4x4 matrix equation:

$$\begin{bmatrix} 1-\alpha_e^{\uparrow\uparrow}G_{1,zz} & -\alpha_e^{\uparrow\uparrow}H_{1,zy} & -\alpha_e^{\uparrow\downarrow}G_{2,zz} & -\alpha_e^{\uparrow\downarrow}H_{2,zy} \\ \alpha_m^{\uparrow\uparrow}H_{1,yz} & 1-\alpha_m^{\uparrow\uparrow}G_{1,yy} & \alpha_m^{\uparrow\downarrow}H_{2,yz} & -\alpha_m^{\uparrow\downarrow}G_{2,yy} \\ -\alpha_e^{\downarrow\uparrow}G_{1,zz} & -\alpha_e^{\downarrow\uparrow}H_{1,zy} & 1-\alpha_e^{\downarrow\downarrow}G_{2,zz} & -\alpha_e^{\downarrow\downarrow}H_{2,zy} \\ \alpha_m^{\downarrow\uparrow}H_{1,yz} & -\alpha_m^{\downarrow\uparrow}G_{1,yy} & -\alpha_m^{\downarrow\downarrow}H_{2,yz} & 1-\alpha_m^{\downarrow\downarrow}G_{2,yy} \end{bmatrix} \begin{bmatrix} p_{1z} \\ m_{1y} \\ p_{2z} \\ m_{2y} \end{bmatrix} = \begin{bmatrix} 0 \\ \alpha_m^{\uparrow\uparrow}E_x^{inc} \\ 0 \\ 0 \end{bmatrix}. \tag{3.2}$$

The transmitted fields can be found afterwards as a superposition of the radiated fields at the bottom interface of each hole. After writing down this superposition in the spectral form as we have done in the theory section, and taking the far field limit, we arrive at the transmission coefficient of the array, being:

$$t = \frac{2\pi i k_3}{A}(1 - r_{32})m_y^d\,. \tag{3.3}$$

Both the magnetic polarisabilities and lattice sums depend on the material and geometrical parameters and are sensitive to the presence and optical properties of the GST. The difference in the magnitude and direction of the shifts between the first device (redshift) and the other two (blueshift) is, therefore due to the presence of GST inside the holes. The position of the resonance wavelength is defined by a combined effect of the change in the polarisability of the holes and the change in the interaction between them. In the first device, the polarisability increases when the GST crystallises, thus redshifting the resonance position, and this effect surpasses the small blueshift due to the change in the interaction terms. This is not the case for the other two devices, where the combined effect leads to a blueshift due to a much smaller change in the polarizability and the lack of compensating the blueshift caused by interaction.

We have performed the analytical calculations for a periodic array of holes drilled in PEC film based on formula (3.3) and the results are plotted in Figure 3.7(b), We can see that the model qualitatively captures the effects of the resonance shifts but quantitatively is still a long way off the experiments. These differences are due to the analytical model [17] of the polarizabilities used in the calculation, which are not completely accuratel. Better fits with experiments can

be achieved if one uses properly simulated polarisabilities for the holes using numerical methods.

3.6 Conclusions

In this chapter, we have demonstrated optical tuning of resonant NH arrays patterned in Au films using GST. The high contrast in the optical properties of GST enables thermal tuning of the resonant response with spectral shifts as large as 385 nm and modulation depths greater than 60%, larger than those previously reported for other designs. Additionally, in one of the samples we have shown that electrical tuning can also be achieved using Au electrodes to crystallise the GST, obtaining results similar to the thermal case. Moreover, for the sample exhibiting the largest shift and modulation, our work shows that the tuning can also be optically induced without the GST undergoing any phase transition, thus extending the lifetime of the device. The resulting optically induced modulation is still large (30%) and occurs over an ultrafast timescale in the ps domain. We have also shown that this effect can be exploited in the visible regime by designing a resonant nanostructure with sharper resonances and larger Q-factors using e-beam lithography. This, opens up the possibility of using these devices in different applications, such as biosensors [18] or plasmonic tuning [19]. With proper scaling, the proposed designs could be extended to the mid-infrared, as GST also exhibits large changes in the optical properties in this regime. Finally, the low-cost nanofabrication methods used in this work [20, 21] for patterning nanostructures incorporating PCMs hold great potential as the basis to manufacture ultrafast and tunable optical devices operating over a wide spectral range.

Bibliography

[1] W. L. Barnes, W. A. Murray, J. Dintinger, E. Devaux, and T. Ebbesen, "Surface plasmon polaritons and their role in the enhanced transmission of light through periodic arrays of subwavelength holes in a metal film," *Physical review letters*, vol. 92, no. 10, p. 107401, 2004.

[2] U. Fano, "Some theoretical considerations on anomalous diffraction gratings," *Physical Review*, vol. 50, no. 6, p. 573, 1936.

[3] H. Ghaemi, T. Thio, D. Grupp, T. W. Ebbesen, and H. Lezec, "Surface plasmons enhance optical transmission through subwavelength holes," *Physical review B*, vol. 58, no. 11, p. 6779, 1998.

[4] F. J. García de Abajo, "Colloquium: Light scattering by particle and hole arrays," *Reviews of Modern Physics*, vol. 79, no. 4, p. 1267, 2007.

[5] D. Pacifici, H. J. Lezec, and H. A. Atwater, "All-optical modulation by plasmonic excitation of cdse quantum dots," *Nature photonics*, vol. 1, no. 7, pp. 402–406, 2007.

[6] A. E. Cetin, A. Mertiri, M. Huang, S. Erramilli, and H. Altug, "Thermal tuning of surface plasmon polaritons using liquid crystals," *Advanced Optical Materials*, vol. 1, no. 12, pp. 915–920, 2013.

[7] L. Waldecker, T. A. Miller, M. Rudé, R. Bertoni, J. Osmond, V. Pruneri, R. E. Simpson, R. Ernstorfer, and S. Wall, "Time-domain separation of optical properties from structural transitions in resonantly bonded materials," *Nature materials*, vol. 14, no. 10, pp. 991–995, 2015.

[8] D. C. H. Lam, *Phase Change Materials: Science and Applications*, M. W. Simone Raoux, Ed. Springer US, 2009.

[9] T. A. Miller, M. Rudé, V. Pruneri, and S. Wall, "Ultrafast optical response of the amorphous and crystalline states of the phase change material ge 2 sb 2 te 5," *Physical Review B*, vol. 94, no. 2, p. 024301, 2016.

[10] M. Wuttig and N. Yamada, "Phase-change materials for rewriteable data storage," *Nature materials*, vol. 6, no. 11, pp. 824–832, 2007.

[11] M. Wuttig, "Phase-change materials: Towards a universal memory?" *Nature materials*, vol. 4, no. 4, pp. 265–266, 2005.

[12] C. Rios, P. Hosseini, C. D. Wright, H. Bhaskaran, and W. H. Pernice, "On-chip photonic memory elements employing phase-change materials," *Advanced Materials*, vol. 26, no. 9, pp. 1372–1377, 2014.

[13] M. Rudé, J. Pello, R. E. Simpson, J. Osmond, G. Roelkens, J. J. van der Tol, and V. Pruneri, "Optical switching at 1.55 μ m in silicon racetrack resonators using phase change materials," *Applied Physics Letters*, vol. 103, no. 14, p. 141119, 2013.

[14] A.-K. U. Michel, P. Zalden, D. N. Chigrin, M. Wuttig, A. M. Lindenberg, and T. Taubner, "Reversible optical switching of infrared antenna resonances with ultrathin phase-change layers using femtosecond laser pulses," *ACS Photonics*, vol. 1, no. 9, pp. 833–839, 2014.

[15] P. Hosseini, C. D. Wright, and H. Bhaskaran, "An optoelectronic framework enabled by low-dimensional phase-change films," *Nature*, vol. 511, no. 7508, pp. 206–211, 2014.

[16] F. J. García de Abajo, J. Sáenz, I. Campillo, and J. Dolado, "Site and lattice resonances in metallic hole arrays," *Optics express*, vol. 14, no. 1, pp. 7–18, 2006.

[17] N. Rotenberg, T. Krijger, B. le Feber, M. Spasenović, F. J. García de Abajo, and L. Kuipers, "Magnetic and electric response of single subwavelength holes," *Physical Review B*, vol. 88, no. 24, p. 241408, 2013.

[18] S. Lal, S. Link, and N. J. Halas, "Nano-optics from sensing to waveguiding," *Nature photonics*, vol. 1, no. 11, pp. 641–648, 2007.

[19] M. A. Kats, R. Blanchard, P. Genevet, Z. Yang, M. M. Qazilbash, D. Basov, S. Ramanathan, and F. Capasso, "Thermal tuning of mid-infrared plasmonic antenna arrays using a phase change material," *Optics letters*, vol. 38, no. 3, pp. 368–370, 2013.

[20] P. Patoka and M. Giersig, "Self-assembly of latex particles for the creation of nanostructures with tunable plasmonic properties," *Journal of Materials Chemistry*, vol. 21, no. 42, pp. 16 783–16 796, 2011.

[21] S. Aksu, A. E. Cetin, R. Adato, and H. Altug, "Lithography: Plasmonically enhanced vibrational biospectroscopy using low-cost infrared antenna arrays by nanostencil lithography (advanced optical materials 11/2013)," *Advanced Optical Materials*, vol. 1, no. 11, pp. 780–780, 2013.

Chapter 4

Tunable perfect absorbers with GST layers

4.1 Introduction

Controlling the spectral transmission, reflection, and absorption properties of optical structures is of great interest for many applications in photonics. In particular, perfect absorbers over a wide frequency (wavelength) range are desirable for thinfilm thermal emitters, thermo-solar cells, photodetectors and smart windows. To date, several mechanisms have been proposed to achieve nearly 100% absorption in various frequency ranges of the electromagnetic spectrum, from microwaves to the near infrared (NIR) and visible. One of the first demonstrations of a structure that could absorb with nearly 100% efficiency was proposed by Landy et al. in 2008 [1], where metamaterial resonator arrays were used to achieve narrowband and highly resonant absorption of GHz and THz waves. The narrowband characteristic of the resonances can be an advantage when absorbers with a high quality factor are required and wavelength selectivity is desirable, while there are also many applications that need broadband absorption. To this end, great efforts have been made during the last decade, for instance by mixing multiple resonances in a many-fold resonator, which can lead to, for example, dual band [2] or multiband [3–9] resonant absorption. Unfortunately, fabrication of these structures requires sophisticated techniques such as micro- or nano-lithography, severely limiting their scalability and increasing the cost of the absorber.

One promising lithography-free approach is the use of absorbers that take advantage of the strong interference effects arising in few layer heterostructures. Several proposals have demonstrated perfect absorption in metal-dielectric-metal Fabry-Pérot-like structures, both in the narrowband [10] and broadband regimes [8, 11]. In these structures, a dielectric layer is placed between a bottom metallic mirror and a top semi-transparent mirror, forming an optical cavity where the light is confined and gradually absorbed by the metallic layers. Other configurations with similar designs but using periodic [12,13] or random arrays [14,15] of nanoparticles as a top mirror layer have also been experimentally demonstrated. In all these structures, the light power was converted into heat due to absorption in the metallic layers or in the metallic particles. However, after conversion of light into heat, it cannot be exploited by photodetectors or photovoltaic cells. In this case, light should be absorbed by the active semiconductor layer, where the creation of electron-hole pairs takes place. High absorption in thin semiconductor layers over a broad range of wavelengths [16, 17] has been demonstrated using a few nm thick Ge layer deposited on the surface of an Au mirror. In this case, the absorption enhancement is a result of strong interference effects due to the phase accumulation when light passes through this absorbing layer. This causes destructive interference on the top surface of the structure and leads to reflection cancellation, thus enhancing the absorption. This reflection suppression mechanism is similar to that taking place in $\lambda/4$ thick dielectric layers, where a π phase shift occurs between primary and partially reflected light beams. The only difference here is that the π phase shifts can be achieved with much thinner layers due to stronger phase accumulation in the absorbing layer. Recently, tunable perfect absorbers have also been demonstrated using patterned graphene [18, 19] and dye molecules [20], as well as using the strong optical interference effects in phase change materials [21]. In recent years, two of the most common phase change materials, VO_2 [22] and $Ge_2Sb_2Te_5$ (GST), have been shown to be promising candidates in the design of reconfigurable optical devices [23,23–25]. We have seen in chapter 3 how one can combine GST with plasmonic structures to tune the resonance in the device. GST has also been proposed as a suitable material for tunable perfect absorber designs both in the narrowband mode [26] and in the broadband mode [27–30], for instance by depositing metallic nanoantenna arrays on top of the layers or by nanopatterning it. However, as noted above, nanopatterning requires expensive techniques, and, therefore, can be challenging and expensive for large scale applications.

In this chapter, we discuss a lithography-free few-layer perfect absorber design based on a combination of GST and readily available metallic and dielectric materials. More specifically, we demonstrate two perfect absorber designs: a broadband perfect absorber in the visible and a narrowband resonant absorber in the NIR. GST plays a crucial role in both achieving a large absorption and in enabling a tunable response by phase transition. Besides being easy to fabricate and inexpensive, the layered design allows a wide range of possible combinations of metals and dielectrics with GST.

4.2 Sample fabrication

The broadband perfect absorber samples were fabricated using RF sputtering and electron beam assisted evaporation techniques. For all absorber designs presented here, the sample fabrication began by depositing the bottom mirror. We used nickel and gold as a mirror layer. Both the Ni and Au mirrors were deposited on top of fused silica substrates using an electron beam assisted evaporation method. In the case of the Au mirror, an initial 3 nm Ti layer had been previously deposited by the same method, in order to enhance the adhesion of the Au film with the silica substrate. The SiO_2 layers were deposited using an atomic layer deposition (ALD) system. The GST layer deposition was carried out using RF co-sputtering from two stoichiometric targets of GeTe and Sb_2Te_3 at 3.75 mT background pressure and 10 sccm Ar flow. The GST deposition rate was checked and carefully controlled by depositing samples of different thicknesses and measuring their thicknesses in an atomic force microscope (AFM). We used a rotatable sample holder to maintain the thickness uniformity over the whole area of the samples. In the case of the narrowband absorber, the first three layers were deposited using the same procedure, changing only the deposition times to get the appropriate thicknesses, and the top Au/Ni layer was deposited again using electron beam assisted evaporation.

4.3 Optical characterization

Angular-dependent reflection measurements of the samples were obtained using a commercial UV/vis/NIR spectrophotometer (Lambda900, Perkin Elmer) with a wavelength range between λ = 300 nm and λ = 3300 nm, using steps

of 5 nm. All simulations were performed using a transfer matrix method implemented in a python environment. Additional simulations were carried out using a genetic algorithm written in Matlab to generate different structures that show strong absorption. The fact that different combinations of metal-dielectric or semiconductor-dielectric layers can have similar performance in terms of absorption confirms that structures based on metal dielectric layers are well suited for this kind of applications.

4.4 Broadband absorber

A schematic of the broadband perfect absorber in the visible range is shown in Figure 4.1(a). It is a simple 4 layers structure deposited on a fused silica substrate. A 100 nm thick metal layer on the bottom acts as a reflector in our structure, followed by a thin (20nm) SiO_2 spacer layer which separates the 13 nm GST layer from the mirror. Another 60 nm thick SiO_2 layer is on top of GST, acting as an index-matching layer between the air and the rest of the structure, and, at the same time, protecting the GST film from oxidation.

4.4.1 Experimental results

The thickness of each layer was optimised to acquire maximum absorption in the visible range using simulations based on a transfer matrix algorithm. This was achieved by fixing the thicknesses of the mirror and GST layers and then calculating the average absorption over the visible range versus the thicknesses of the top and spacer SiO_2 layers (Figure4.1(b)). Moreover, we fabricated samples both with Au and the cheaper alternative Ni as mirror layers. Both of these have similar absorption spectra with a slightly broader response in the latter case. This can be explained by the higher intrinsic losses of Ni compared to Au. The experimental absorption curves for the sample with the Ni mirror are given in Figures 4.1(c) and (d) for the amorphous and crystalline GST phases, respectively. Both samples show nearly 100% absorption in the visible range when GST is in the amorphous phase, remaining above 80% up to 900 nm. Upon a phase transition from the amorphous to the crystalline phase, a 20% reduction in absorption is observed uniformly over the entire band (Figures 4.1(d)). The changes were more pronounced for the reflection, which varied from 0% to 20%, making the effect clearly visible to the naked eye (insets of Figures 4.1(c) and

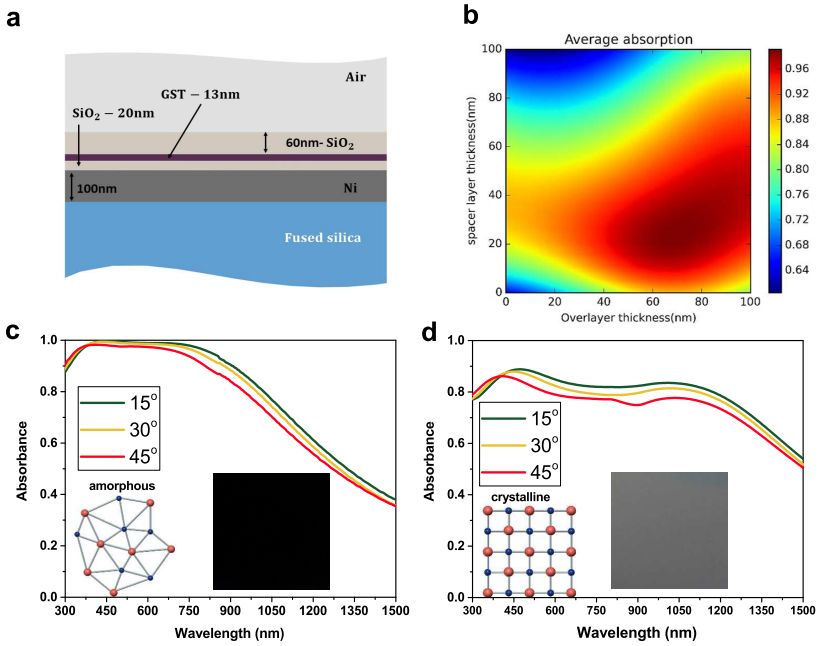

Figure 4.1: (a) Schematic representation of the broadband absorber with Ni mirror. (b) Spacer and overlayer thicknesses dependent, angle and wavelength averaged absorption. Experimental absorption curves for three different incidence angles for amorphous (c) and crystalline (d) phases, respectively. (c), (d) Insets: Real images of the corresponding fabricated samples in amorphous and crystalline phases.

(d). Similar results are obtained using an Au mirror (see Figure 4.2).

4.4.2 Theoretical analysis

The absorption mechanism can be attributed to strong absorption effects in the ultrathin semiconductor layers associated with interference between multiple reflected light beams [16,31]. Here, due to the high refractive index of GST at these wavelengths, the light beams accumulate strong phase shifts upon each passage through them and subsequent reflection from the metallic mirror surface. These partial beams interfere destructively with the primary reflected beam on the top surface of the GST layer if the relative phase difference is equal to π. It is worth pointing out that the π shift difference is not the only condition required in order

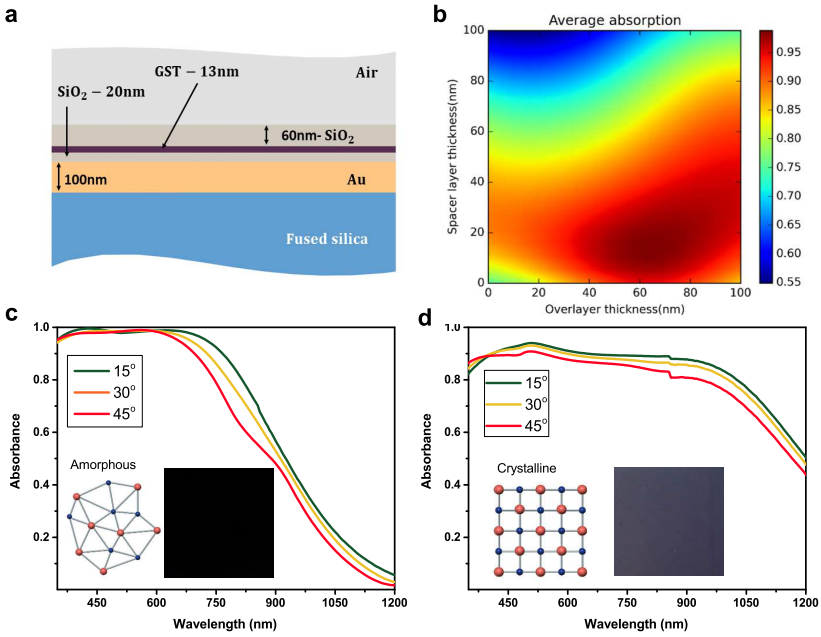

Figure 4.2: (a) Schematic of the broadband absorber with gold mirror. (b) Colour map plot of the wavelength-averaged absorption for different thicknesses of SiO_2 overlayer and spacer-layer. Experimental absorbance curves for amorphous (c) and crystalline (d) phases of the GST for different angles of incidence. (c), (d) Insets: Schematic representations and real picture of the GST sample respectively for amorphous and crystalline phases.

to achieve zero reflection in the device. The sum of the reflected beams' amplitudes must also be close to the amplitude of the primary beam. However, this may not be satisfied completely in the case of very absorptive active layers, as the amplitude of each partial wave will be very small due to attenuation upon passage. The additional, top index-matching layer reduces the reflection and intensity of the primary beam at the first GST interface. In this way, one can easily achieve complete destructive interference.

Using a homemade transfer matrix code, we performed simulations to find the thickness of the index-matching SiO_2 layer for a given GST layer thickness that maximizes the average absorption over the whole visible range. The resulting colour map plot is shown in Figure 4.1(b), from which one can see that

there exists a range of parameters that enhance the absorption. One of the main advantages of the proposed structure with thin absorbing layers is its omnidirectionality, i.e. the absorption remains high up to large angles of incidence. This is due to the fact that the structure is composed of very thin layers and that the internal angles of the refracted beams are small because of the high refractive index of the GST, meaning that large angles are needed to move away from the destructive interference condition (see Figure 4.3).

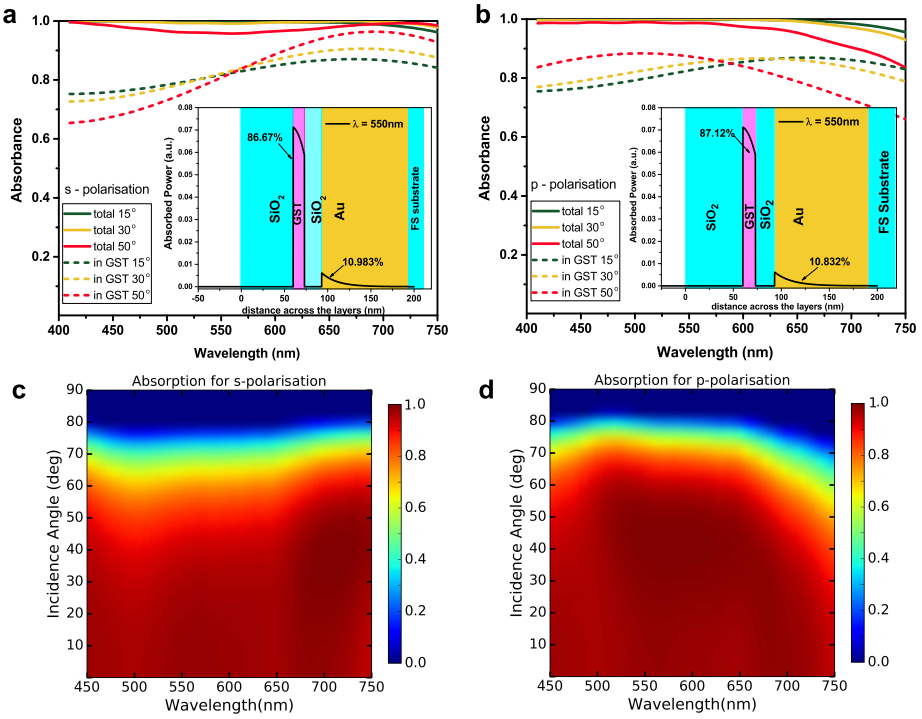

Figure 4.3: (a) Comparison of the total absorption and the absorption in GST layer for different incidence angles in the case of s-polarised incidence light. (b) Same comparison in the case of p-polarisation. (a), (b) Insets: Angle and wavelength dependent absorption for s and p-polarised incident lights.

Figure 4.3(a) and (b) show plots of the theoretical absorption as a function of the incidence angle for p- and s- polarisations, respectively. Figures 4.3(c) and (d) are the corresponding colour map plots of the absorption as a function

of the wavelength and the incidence angle. The absorption remains high up to large incidence angles of about 70o. The insets of Figure 4.3(a) and (b) show the calculated absorbed power distributions. It is interesting to note that most of the light (about 80%) is absorbed in the GST layer, making the proposed structure particularly suitable for photovoltaic and photodetection applications where strong absorption in the semiconductor layer is required.

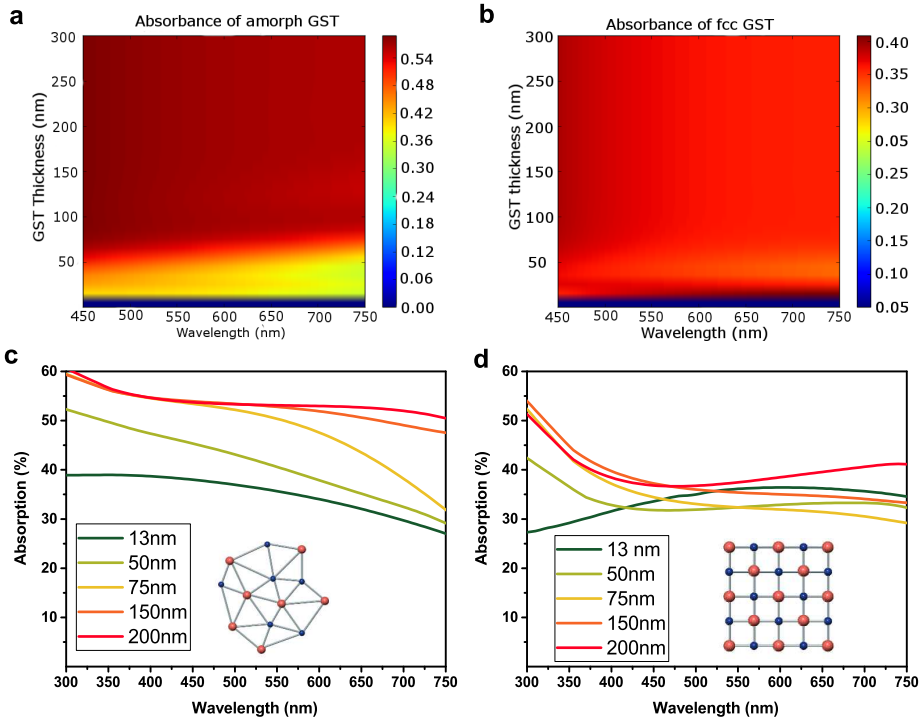

Figure 4.4: (a), (b) Simulated absorption of bare GST of different thicknesses on top of a fused silica substrate in the amorphous and crystalline phases, respectively. (c), (d) Experimental absorption curves for the same films deposited on a fused silica substrate.

In order to better quantify the potential of our design, we compared these results with the absorption of bare GST layers with different thicknesses on fused silica for both the crystalline and the amorphous phases as given in Figures 4.4(a) and 4.4(b). In this case, the absorption of bare GST saturates for thicknesses above 75 nm and, thus, it can never exceed 60% (amorphous) and 40% (crys-

talline). This confirms the crucial role of the SiO_2 layer and interference effects in enhancing the overall absorption. These numerical simulations are also confirmed by measurements of the GST films deposited under the same conditions (Figures 4.4(c), (d)).

4.5 Resonant absorber

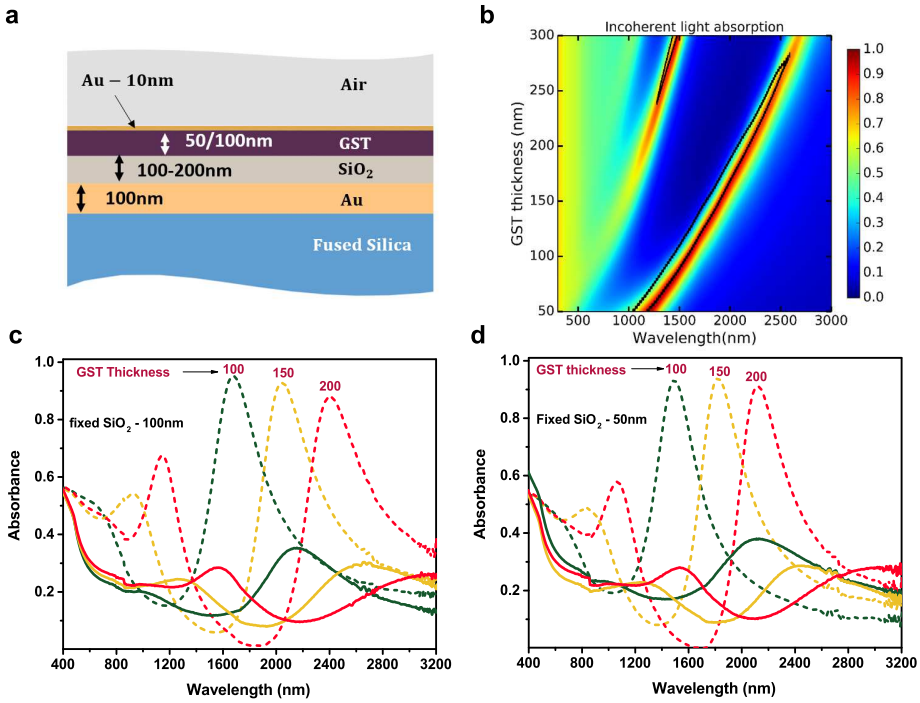

Figure 4.5: (a) Schematic of the narrowband absorber with Au mirrors. (b) Colour map plot of the simulation results for device absorption for 100nm thick SiO_2 layer and GST thicknesses in the range of 50-300nm. The black contour line represents the contour of the region where the phase and amplitude balance equations are satisfied. (c) Experimental absorption curves for unpolarised light for 50 nm SiO_2 spacer layer, with amorphous and crystalline GST layers. (d) Absorption of the same structure with a thicker SiO_2 spacer layer (100 nm).

Although the absorption efficiency and the bandwidth of the broadband absorber device in the visible is very high and a considerable amount of contrast can be achieved by changing the phase of the GST layer from amorphous to crystalline, an even stronger contrast (tuning) can be demonstrated in the NIR. This is because in the visible range both amorphous and crystalline GST are highly absorptive (see refractive indices of GST in Figure 3.1), limiting the absorption contrast upon transition from one state to another. On the contrary, in the NIR range the absorption of amorphous GST becomes negligible although this is not the case for crystalline GST. This leads to a stronger tuning, which can be achieved by a resonant absorber design. This, similarly to the visible counterpart, consists of a few layers. Figure 4.5 a) shows a schematic of the second structure proposed in this work. It consists of 4-layers with a configuration similar to that of the broadband case but with a 10 nm Au layer replacing the top SiO_2 layer. We considered two thicknesses for the SiO_2 spacer layer, which is another parameter providing design flexibility and optimisation. For each thickness of the SiO_2 layer (50 and 100 nm) we investigated samples with 100 nm, 150 nm and 200 nm thick GST layers.

4.5.1 Theoretical discussion

We have performed parametric sweep simulations demonstrating the dependence of the resonant wavelength on the thickness change for both the GST and SiO_2 layers. One of these parametric sweep plots is shown in Figure 4.5(b) for a given SiO_2 layer thickness (100nm) and varying GST layer thicknesses. It is evident that for each GST layer thickness there exists a resonant wavelength at which nearly 100% absorption occurs, thus allowing one to design a perfect absorber for any desired wavelength by simply choosing the appropriate thicknesses. The experimental absorption curves for the different thicknesses of the GST and SiO_2 layers are shown in Figures 4.5(c) and (d). Contrary to the broadband nature of the first structure in the visible, this second structure shows resonant absorption in the NIR region with very high absorption efficiencies above 80% at the resonance wavelength in all cases. This experiment is also performed using Ni mirrors, showing similar narrowband behaviour (see Figure 4.6). When the GST is crystallised, these resonances are strongly reduced (down to 5%) and red shifted (Figures 4.5(c) and (d)). This is due to an increase in both the refractive index and the absorption coefficient in the NIR region of the GST upon crystallisation, which breaks the conditions for Fabry-Pérot resonances that were present in the

amorphous phase. These changes are more evident if one looks at the reflection spectra (R=1-A), which shows how the structure changes from a state of almost zero reflection to a state with high reflection (see Figure 3.1). Although it will

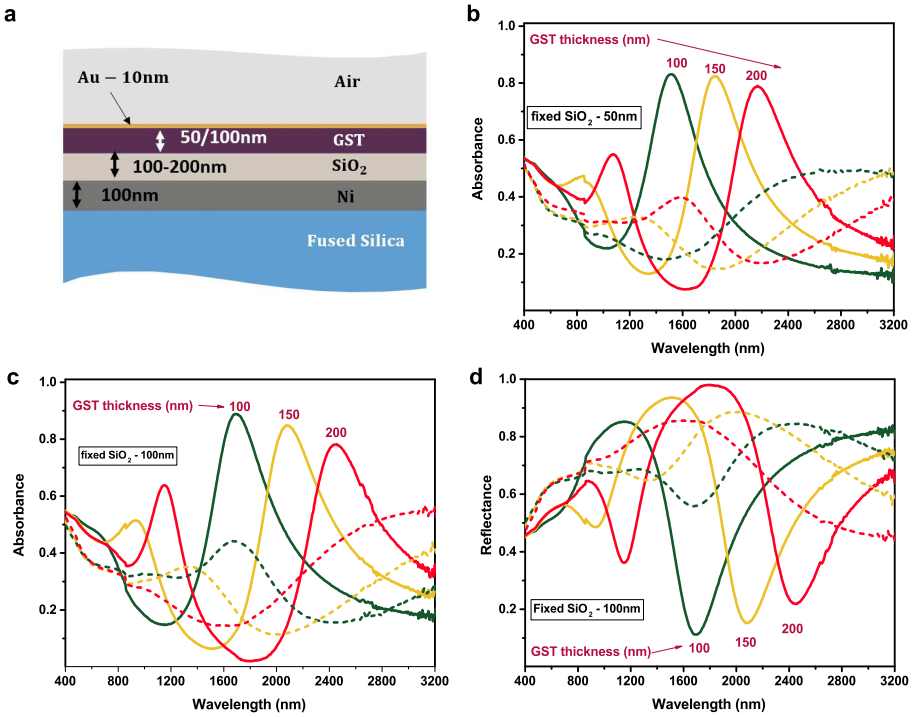

Figure 4.6: (a) Schematic of the narrowband absorber with Ni mirror. (b) Colour map plot of the simulation results for device absorption for 100nm thick SiO_2 layer and GST thicknesses in the range of 50-300nm. The black contour line represents the contour of the region where the phase and amplitude balance equations are satisfied. (c) Experimental absorption curves for unpolarised light for 50 nm SiO_2 spacer layer, with amorphous and crystalline GST layers. (d) Absorption of the same structure with a thicker SiO_2 spacer layer (100 nm).

be shown below that the absorption mechanisms are different to the broadband case, the light trapping and Fabry-Pérot resonances are again attributed to reflection cancellation on the top surface of the structure. This can be easily demonstrated using the generalised Fresnel equation for the reflection of the multilayer structure which is given by [32]:

$$r_{j/m} \equiv r_{j/k/m} = r_{j/k} + \frac{t_{j/k} t_{k/j} r_{k/m} e^{2i\beta_k d_k}}{1 - r_{k/j} r_{k/m} e^{2i\beta_k d_k}}\,, \tag{4.1}$$

where $r_{j/m}$ is the reflection coefficient for a stack starting at layer j and ending at layer m, and k identifies any intermediate layer; $\beta_i = (k_i^2 - q^2)^{1/2}$ and $q = \omega \sin\theta / c$ are the perpendicular and the parallel components of the wave vector in the layer i, respectively, with dielectric permittivity ε_i, magnetic permeability μ_i and thickness d_i. $k_i = n_i \omega / c$, where $n_i = (\varepsilon_i \mu_i)^{1/2}$ is the refractive index of the layer, and ω and c are the frequency and the speed of the light in vacuum, respectively. For a resonant absorber structure we can write:

$$r_{0/5} = r_{01} + \frac{t_{01} t_{10} r_{1/5} e^{2i\beta_1 d_1}}{1 - r_{10} r_{1/5} e^{2i\beta_1 d_1}}\,, \tag{4.2}$$

which accounts for total reflection on the top surface (layer number 1 is considered the intermediate layer between mediums number 0 and 5- air and glass substrate respectively). Here, $r_{1/5}$ is the total reflection coefficient of the layers from one to five, and the interface reflection and transmission coefficients between any adjacent layers are:

$$r_{ij} = \frac{\beta_i - \gamma_{ij}\beta_j}{\beta_i + \gamma_{ij}\beta_j}, \qquad t_{ij} = \sqrt{\frac{\gamma_{ij}}{\gamma_{ij}^s}}(1 + r_{ij})\,, \tag{4.3}$$

with $\gamma_{ik}^p = \varepsilon_i / \varepsilon_j$ and $\gamma_{ik}^s = \mu_i / \mu_j$ for p- and s-polarised light, respectively. The reflection cancellation is given by the condition:

$$r_{01} = \frac{t_{01} t_{10} r_{1/5} e^{2i\beta_1 d_1}}{1 - r_{10} r_{1/5} e^{2i\beta_1 d_1}} e^{i\pi}\,. \tag{4.4}$$

Notice that the π phase term is related to the destructive interference condition. In this formula, r_{01} represents the primary reflected beam at the top interface while the multiple reflected beams are merged into a single term on the right hand side of the equation. One can easily verify this by reapplying the generalized Fresnel formula of the multiplayer $r_{1/5}$ and using the geometric series representation of the denominator

$$\frac{1}{1 - r_{10} r_{1/5} e^{2i\beta_1 d_1}} = \sum_{n=0}^{\infty} (r_{10} r_{1/5} e^{2i\beta_1 d_1})^n\,. \tag{4.5}$$

Instead of this general complex expression we can consider two balance equations for amplitudes and phases:

$$|r_{01}| = \frac{\left|t_{01}t_{10}r_{1/5}\right|}{\left|1 - r_{10}r_{1/5}e^{2i\beta_1 d_1}\right|}, \tag{4.6a}$$

$$\arg(r_{01}) = \arg(t_{01}t_{10}r_{1/5}) - \arg(1 - r_{10}r_{1/5}e^{2i\beta_1 d_1}) + 2\beta_1 d_1 + \pi\,, \tag{4.6b}$$

which should be satisfied simultaneously in order to cancel the reflection on the top surface.In Figure 4.5(b), we have plotted the region of the parameter space where these two equations are satisfied simultaneously (region inside the black contour). As one can see, both the maximal absorption regions and the balance equation regions coincide. This shows that the described cancellation mechanism is responsible for the light trapping and enhancement of absorption. As in the case of the broadband absorber, the absorption does not change significantly up to very large angles of incidence in this case either, confirming the role played by the high refractive index values of the GST in reducing the effects that one would expect when increasing the layer thickness. This can be seen in Figure 4.7, where the experimental absorption curves for different samples are shown for different angles of incidence. It is worth noting that despite having a similar architecture, the broadband and resonant absorbers mechanisms are different. As we have discussed above, in the former case, the absorption is associated with destructive interference between reflected beams, with most of the light absorbed in the GST layer. In the amorphous phase, the GST is very absorbing in the visible while it is very transparent in the NIR. On the contrary, in the crystalline phase it becomes more absorbing when one goes from the visible to the NIR (see Figure 3.1). In this case, the structure is a resonant (Fabry-Pérot like) and the absorption occurs mostly in the top and bottom metal layers. Since the quality factor of the resonances in the Fabry-Pérot like structures depends on that of the cavity (mirrors), we used Au for both the top and bottom mirrors because it is less absorptive than Ni. This provided narrower resonances in the near NIR. Ni mirrors were preferable in the visible as their absorption was not critical and they are less expensive than Au mirrors.

We calculated the spatial distribution of the normalised absorbed power within the sample at three different wavelengths (Figure 4.8(b), (c) and (d)), corresponding to maximum and minimum absorption points of the wavelength spectrum (Figure 4.8(a)). In the case of maximum absorption (λ=2190nm), most of the power is dissipated into the top Au layer (50.45%). GST absorbs only 37.81 %

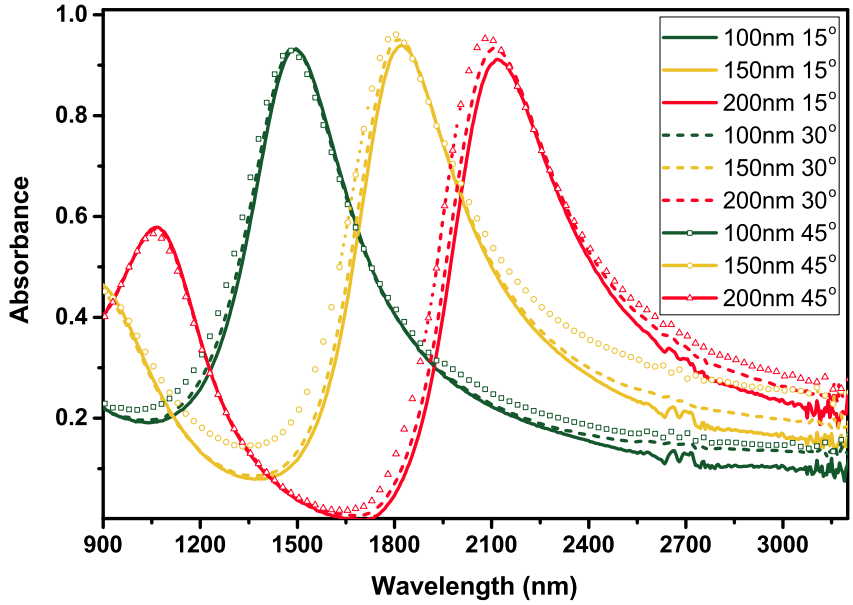

Figure 4.7: Experimental absorption curves for amorphous GST at different angles of incidence. The curves are given for different thicknesses of GST layer(100, 150 and 200 nm) for 100nm thick fixed SiO_2 layer.

of the incident power and the remaining power is absorbed by the Au mirror, confirming that the absorption mechanism is different to that of the broadband case. At the dip wavelength, both the GST and the bottom layers start to absorb slightly. Note that the graphs represent only the fraction of the power absorbed in each layer and not its absolute value. This means that the increase in absorption compared to the case of Figure 4.8(b) is only apparent as one has to consider that the absorption in the GST is negligible at this wavelength (1760 nm). Finally, in the case of the peak at 1160 nm, a relatively higher fraction of the light is absorbed in the GST layer, where the GST has a higher loss.

Finally, a comparison with previous perfect absorber designs reported in literature is shown in Table 4.1. The proposed structure has significant improvements in the visible in terms of absorption bandwidth and angular dependence. The fabrication techniques is another significant advantage over previous metamaterial and plasmonic antenna based absorbing surfaces, as it does not involve

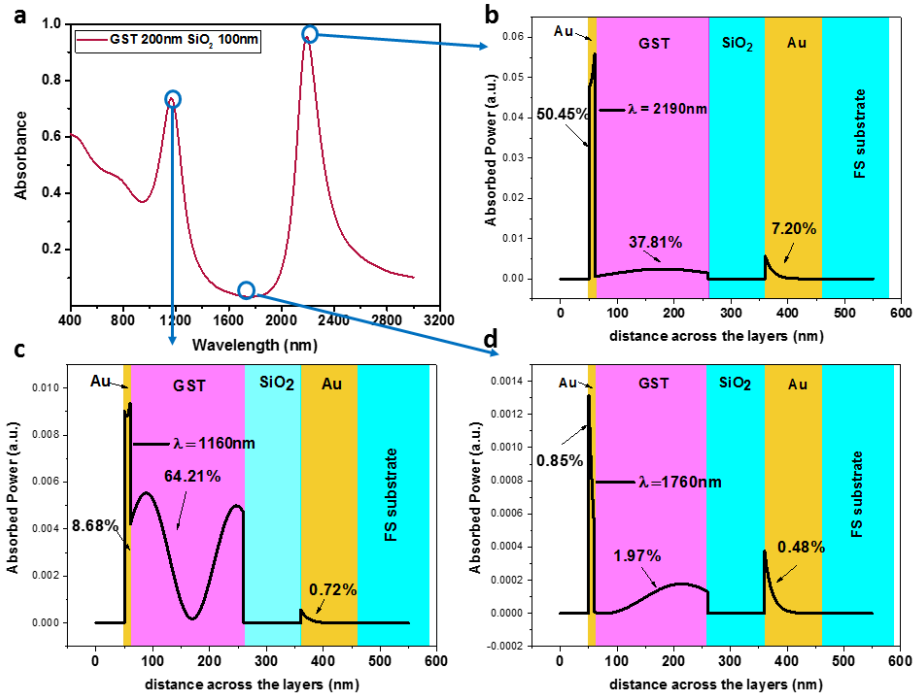

Figure 4.8: (a) Simulated wavelength dependent absorbance for resonant structure with 200 nm thick GST and 100 nm thick SiO_2. (b), (c), (d) Absorption profiles across the multilayer structure at λ=2190 nm, λ=1160 nm and λ=1760 nm respectively.

expensive lithography. Moreover our design using only few-layer structures, can be tailored for broadband or narrow band resonant operation, depending on the wavelength range and the structure design, due to the GST wavelength dependent absorption and refractive index coefficients.

4.6 Conclusions

In conclusion, we have proposed and demonstrated a novel few-layers perfect optical absorbers, incorporating phase change materials to prevent from expensive and time consuming sophisticated lithography procedures. Because of their reliability, wavelength tailoring and optical response switching the proposed structures may be used to offer new functionalities, while simplicity of the deposition

References	Wavelength range (um)	Polarization independence	Wide angle	Total abs.	Abs. in active layer	Lithography free	Dynamic Tunability
our absorber	0.3 - 0.8 NIR-resonant	yes	yes	$\approx 100\%$	up to 85% in vis and 95% in NIR	yes	yes
[16]	2-10	–	–	20-80%	–	no	yes
[26]	2.5-4	yes	yes	90%	–	no	yes
[28]	0.61-0.87	yes	yes	>95%	–	no	yes
[29]	1-3	no	–	$\approx 100\%$	–	no	yes
[33]	0.35-0.55	no	yes	$\approx 100\%$	–	yes	no
[15]	1.3-2.1	yes	no	$\approx 100\%$	–	no	no
[34]	0.4-1	yes	no	$\approx 100\%$	20-80%	yes	no
[35]	0.3 -0.8	–	–	80% to >95%	–	yes	no
[14]	0.4-0.75	no	yes	>95$	–	yes	no
[8]	visible--resonant	no	no	$90 - 95\%$	no	yes	no

Table 4.1: Table of comparison of our absorber to absorbers from literature

process makes such structures suitable for photovoltaic and photodetector technologies.

Bibliography

[1] N. Landy, S. Sajuyigbe, J. Mock, D. Smith, and W. Padilla, "Perfect metamaterial absorber," *Physical review letters*, vol. 100, no. 20, p. 207402, 2008.

[2] X. Xiong, S.-C. Jiang, Y.-H. Hu, R.-W. Peng, and M. Wang, "Structured metal film as a perfect absorber," *Advanced Materials*, vol. 25, no. 29, pp. 3994–4000, 2013.

[3] R. Feng, W. Ding, L. Liu, L. Chen, J. Qiu, and G. Chen, "Dual-band infrared perfect absorber based on asymmetric t-shaped plasmonic array," *Optics express*, vol. 22, no. 102, pp. A335–A343, 2014.

[4] J. Liu, M. Zhu, N. Zhang, H. Zhang, Y. Zhou, S. Sun, N. Yi, S. Gao, Q. Song, and S. Xiao, "Wafer-scale metamaterials for polarization-insensitive and dual-band perfect absorption," *Nanoscale*, vol. 7, no. 45, pp. 18 914–18 917, 2015.

[5] X. Duan, S. Chen, W. Liu, H. Cheng, Z. Li, and J. Tian, "Polarization-insensitive and wide-angle broadband nearly perfect absorber by tunable planar metamaterials in the visible regime," *Journal of Optics*, vol. 16, no. 12, p. 125107, 2014.

[6] J. Rhee, Y. Yoo, K. Kim, Y. Kim, and Y. Lee, "Metamaterial-based perfect absorbers," *Journal of Electromagnetic Waves and Applications*, vol. 28, no. 13, pp. 1541–1580, 2014.

[7] J. Wang, C. Fan, P. Ding, J. He, Y. Cheng, W. Hu, G. Cai, E. Liang, and Q. Xue, "Tunable broad-band perfect absorber by exciting of multiple plas-

mon resonances at optical frequency," *Optics express*, vol. 20, no. 14, pp. 14 871–14 878, 2012.

[8] Z. Li, S. Butun, and K. Aydin, "Large-area, lithography-free super absorbers and color filters at visible frequencies using ultrathin metallic films," *ACS Photonics*, vol. 2, no. 2, pp. 183–188, 2015.

[9] S. Butun and K. Aydin, "Structurally tunable resonant absorption bands in ultrathin broadband plasmonic absorbers," *Optics express*, vol. 22, no. 16, pp. 19 457–19 468, 2014.

[10] Y. Rádi, C. Simovski, and S. Tretyakov, "Thin perfect absorbers for electromagnetic waves: Theory, design, and realizations," *Physical Review Applied*, vol. 3, no. 3, p. 037001, 2015.

[11] H. Deng, Z. Li, L. Stan, D. Rosenmann, D. Czaplewski, J. Gao, and X. Yang, "Broadband perfect absorber based on one ultrathin layer of refractory metal," *Optics Letters*, vol. 40, no. 11, pp. 2592–2595, 2015.

[12] M. Yan, "Metal–insulator–metal light absorber: a continuous structure," *Journal of Optics*, vol. 15, no. 2, p. 025006, 2013.

[13] T. D. Dao, K. Chen, S. Ishii, A. Ohi, T. Nabatame, M. Kitajima, and T. Nagao, "Infrared perfect absorbers fabricated by colloidal mask etching of al–al2o3–al trilayers," *ACS Photonics*, vol. 2, no. 7, pp. 964–970, 2015.

[14] M. K. Hedayati, M. Javaherirahim, B. Mozooni, R. Abdelaziz, A. Tavassolizadeh, V. S. K. Chakravadhanula, V. Zaporojtchenko, T. Strunkus, F. Faupel, and M. Elbahri, "Design of a perfect black absorber at visible frequencies using plasmonic metamaterials," *Advanced Materials*, vol. 23, no. 45, pp. 5410–5414, 2011.

[15] Z. Liu, X. Liu, S. Huang, P. Pan, J. Chen, G. Liu, and G. Gu, "Automatically acquired broadband plasmonic-metamaterial black absorber during the metallic film-formation," *ACS applied materials & interfaces*, vol. 7, no. 8, pp. 4962–4968, 2015.

[16] M. A. Kats, D. Sharma, J. Lin, P. Genevet, R. Blanchard, Z. Yang, M. M. Qazilbash, D. Basov, S. Ramanathan, and F. Capasso, "Ultra-thin perfect

absorber employing a tunable phase change material," *Applied Physics Letters*, vol. 101, no. 22, p. 221101, 2012.

[17] M. A. Kats, S. J. Byrnes, R. Blanchard, M. Kolle, P. Genevet, J. Aizenberg, and F. Capasso, "Enhancement of absorption and color contrast in ultra-thin highly absorbing optical coatings," *Applied Physics Letters*, vol. 103, no. 10, p. 101104, 2013.

[18] Z. Fang, Y.-R. Zhen, L. Fan, X. Zhu, and P. Nordlander, "Tunable wide-angle plasmonic perfect absorber at visible frequencies," *Physical Review B*, vol. 85, no. 24, p. 245401, 2012.

[19] X. He, "Tunable terahertz graphene metamaterials," *Carbon*, vol. 82, pp. 229–237, 2015.

[20] M. K. Hedayati, M. Javaheri, A. U. Zillohu, H. J. El-Khozondar, M. S. Bawa'aneh, A. Lavrinenko, F. Faupel, and M. Elbahri, "Photo-driven super absorber as an active metamaterial with a tunable molecular-plasmonic coupling," *Advanced Optical Materials*, vol. 2, no. 8, pp. 705–710, 2014.

[21] P. Hosseini, C. D. Wright, and H. Bhaskaran, "An optoelectronic framework enabled by low-dimensional phase-change films," *Nature*, vol. 511, no. 7508, pp. 206–211, 2014.

[22] M. A. Kats, R. Blanchard, P. Genevet, Z. Yang, M. M. Qazilbash, D. Basov, S. Ramanathan, and F. Capasso, "Thermal tuning of mid-infrared plasmonic antenna arrays using a phase change material," *Optics letters*, vol. 38, no. 3, pp. 368–370, 2013.

[23] M. Rudé, J. Pello, R. E. Simpson, J. Osmond, G. Roelkens, J. J. van der Tol, and V. Pruneri, "Optical switching at 1.55 μm in silicon racetrack resonators using phase change materials," *Applied Physics Letters*, vol. 103, no. 14, p. 141119, 2013.

[24] Y. Chen, T. Kao, B. Ng, X. Li, X. Luo, B. Luk'yanchuk, S. Maier, and M. Hong, "Hybrid phase-change plasmonic crystals for active tuning of lattice resonances," *Optics express*, vol. 21, no. 11, pp. 13 691–13 698, 2013.

[25] M. Rudé, V. Mkhitaryan, A. E. Cetin, T. A. Miller, A. Carrilero, S. Wall, F. de Abajo, H. Altug, and V. Pruneri, "Ultrafast broadband tuning of resonant optical nanostructures using phase change materials," *arXiv preprint arXiv:1506.03739*, 2015.

[26] A. Tittl, A.-K. U. Michel, M. Schaferling, X. Yin, B. Gholipour, L. Cui, M. Wuttig, T. Taubner, F. Neubrech, and H. Giessen, "A switchable mid-infrared plasmonic perfect absorber with multispectral thermal imaging capability," *Advanced Materials*, vol. 27, no. 31, pp. 4597–4603, 2015.

[27] T. Cao, C. Wei, R. E. Simpson, L. Zhang, and M. J. Cryan, "Rapid phase transition of a phase-change metamaterial perfect absorber," *Optical Materials Express*, vol. 3, no. 8, pp. 1101–1110, 2013.

[28] T. Cao, C.-w. Wei, R. E. Simpson, L. Zhang, and M. J. Cryan, "Broadband polarization-independent perfect absorber using a phase-change metamaterial at visible frequencies," *Scientific reports*, vol. 4, 2014.

[29] Y. Chen, X. Li, X. Luo, S. A. Maier, and M. Hong, "Tunable near-infrared plasmonic perfect absorber based on phase-change materials," *Photonics Research*, vol. 3, no. 3, pp. 54–57, 2015.

[30] Y. Cui, J. Xu, K. H. Fung, Y. Jin, A. Kumar, S. He, and N. X. Fang, "A thin film broadband absorber based on multi-sized nanoantennas," *Applied Physics Letters*, vol. 99, no. 25, p. 253101, 2011.

[31] M. A. Kats, R. Blanchard, P. Genevet, and F. Capasso, "Nanometre optical coatings based on strong interference effects in highly absorbing media," *Nature materials*, vol. 12, no. 1, pp. 20–24, 2013.

[32] M.-S. Tomaš, "Recursion relations for generalized fresnel coefficients: Casimir force in a planar cavity," *Physical Review A*, vol. 81, no. 4, p. 044104, 2010.

[33] M. Hedayati, A. Zillohu, T. Strunskus, F. Faupel, and M. Elbahri, "Plasmonic tunable metamaterial absorber as ultraviolet protection film," *Applied Physics Letters*, vol. 104, no. 4, p. 041103, 2014.

[34] H. Song, L. Guo, Z. Liu, K. Liu, X. Zeng, D. Ji, N. Zhang, H. Hu, S. Jiang, and Q. Gan, "Nanocavity enhancement for ultra-thin film optical absorber," *Advanced Materials*, vol. 26, no. 17, pp. 2737–2743, 2014.

[35] M. K. Hedayati, F. Faupel, and M. Elbahri, "Tunable broadband plasmonic perfect absorber at visible frequency," *Applied Physics A*, vol. 109, no. 4, pp. 769–773, 2012.

Chapter 5

Transparent electrodes with multilayer thin films

5.1 Introduction

A wide range of electronic and optoelectronic devices require transparent conductors (TCs) to function. These include, for example, displays, light emitting diodes and photovoltaic cells, where TCs are used to either apply or collect electrical signals without reducing optical transmission (T) [1–5]. An intensive effort has been devoted to the search for TC materials that can replace Indium Tin Oxide (ITO), a wide band gap semiconductor, which is used in most of, if not all, the devices needing TCs today. Despite possessing large T, low electrical sheet resistance (R_s), and high chemical and environmental stability, ITO requires high temperature processing, and has poor mechanical flexibility and a high raw material cost [6].Among the material alternatives, Al-doped ZnO (AZO), carbon nanotubes, metal nanowires, ultrathin metals, conducting polymers and, most recently, graphene have been extensively considered [3, 7–19]. Some of these alternatives can overcome the mechanical fragility, high temperature processing and/or cost of ITO but still suffer from one or more drawbacks, such as poor adhesion, large surface roughness and high optical scattering, and don't always achieve a competitive trade-off between T and R_s [20–24].

Ultrathin metal films (UTMFs) can present very low R_s but their T is low unless antireflection (AR) undercoat and overcoat layers are applied [25, 26]. Though the AR concept in TC is widely known, it has never been investigated

and exploited fully, es- pecially in conjunction with high quality UTMFs. In the absence of scattering, which is the case for the work presented in this paper, the optical loss (OL) that accounts for the reduction in T with respect to the bare substrate (without TC) comes from absorption (A) of the TC material itself and reflection (R) at the interfaces in the TC on the substrate structure.

In this chapter we study in depth the AR properties of a TC structures on glass substrates made of ultrathin Ag with TiO_2 undercoat and AZO overcoat layers and show that, through a proper optimised design, reflection can be strongly suppressed.The OL of the optimised TiO_2/Ag/AZO structure (about 1.6 %) is even lower than that of a single layer graphene (2.3 %) while the figure of merit (FOM) is 4 times larger than that of ITO, thanks to the very high T (greater than 98 %) and low R_s (less than 6 Ω per square). The proposed TC has the highest electro-optical performance (FOM) reported so far, is mechanically flexible, is processed at room temperature and its potential for real applications is demonstrated by showing that it can be used as an efficient transparent shield for radiofrequency and microwave electromagnetic interference (EMI) signals, with 30 dB attenuation up to 18GHz.

5.2 AR-TC electrode

The structure of the proposed multilayer AR-TC is shown in Figure 5.1(a).

5.2.1 Sample fabrication

Double side optically polished UV fused silica glass substrates, with a thickness of 1 mm and an area of 1 inch square were used as substrate. Before TC deposition, the substrates were cleaned in acetone followed by ethanol in ultrasonic bath, each process lasting 10 min. The substrates were then rinsed in deionized (DI) water and dried with nitrogen gas. The entire TC structure was deposited by magnetron sputtering without breaking the vacuum. The sputtering chamber was initially evacuated to a base pressure of $\approx 10^{-7} - 10^{-8}$ Torr. The target-to substrate distance was maintained at 30 cm. The substrate holder was rotating during deposition with a speed of 60 rpm. For improving the adhesion properties of the film to the substrate, low power argon plasma cleaning was performed for 15 minutes inside the sputtering equipment before the TC deposition. Bias power of 40W and pressure of 8mT were used for cleaning in Ar (20 sccm) at-

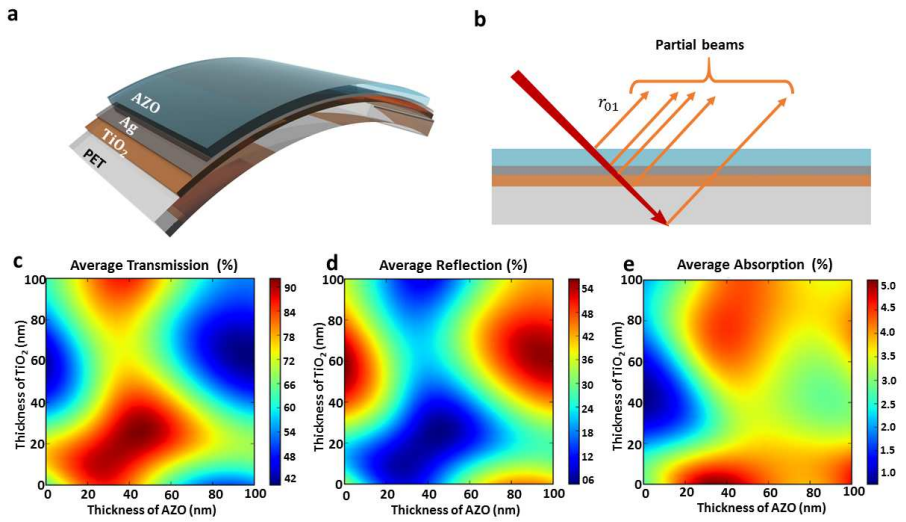

Figure 5.1: (a) structure of Antireflection Transparent Conductor (AR-TC) (b) Conceptual diagram showing multiple reflection contributions leading to destructive interference and AR effect. Simulated transmission (c), reflection (d) and absorption (e) of AR-TC for different TiO_2 and Al doped ZnO (AZO) thicknesses. For all the structures, the Ag film thickness is kept constant at 12 nm. The transmission, reflection and absorption include the substrate contribution, i.e. they refer to the whole TC on substrate structure, and are average values over 400 to 700 nm wavelength range.

mosphere. TiO_2 and Ag were deposited in pure Ar atmosphere while AZO (3% Al doping) was deposited in an Ar/O_2 mixture (with flux ratio of 18:2), all of them at room temperature. An Ag (99.99%) target was used for depositing the Ag films with DC power of 100 W and working pressure of 2 mTorr. The TiO_2 film was deposited in radio frequency (RF) mode (150W RF power) at a pressure of 2 mTorr. The AZO film was deposited in the same condition but with a pressure of 1.4 mTorr. The deposition rate was 0.1, 3.5, and 0.3 Å/sec for TiO_2, Ag, and AZO, respectively.

5.2.2 Device characterisation

The electrical properties of the films were measured using four-point method with cascade Microtech 44/7 S 2749 probe station connected to a Keithley 2001

multimeter. Typically, six measurements were performed at different positions and R_s was an average of the corresponding values. Agilent cary5000 UV-Vis-NIR Spectrophotometer with universal measurement accessory (UMA) and polarizer was used for optical transmission measurements. Prior to measurements, the samples were cleaned using a TX® 609 Technicloth® wiper dampened with HPLC grade reagent alcohol. A background scan was performed before each new measurement configuration (i.e. polarization). Transmission and reflection (2-surface) were taken without moving the sample, with the coated surface toward the incident beam, at 6^o, 25^o, 50^o and 70^o, for s and p polarizations. 1st surface reflection was measured with an index matching oil on the back surface of the sample to a 3390 black glass. In this way the second (back) surface reflection was completely suppressed. Flexibility tests were performed using a two-point bend testing setup connected to a motor driven by an electronic controller allowing the arm to move back and forth along the horizontal direction. AR-TC deposited onto Poly Ethylene Terephthalate (PET) polymeric substrates and subjected it to continuous bending. R_s was measured while the bending radii was in the range 10 to 3mm.

5.2.3 Experiments and discussion

For the experiments and simulations, we deposited the AR-TC structure on a fused silica substrate, but the work can be extended to other transparent substrates with a similar refractive index, including other glasses and polymers. From the metals, we chose Ag as it has among the highest electrical conductivity and lowest absorption loss. However, it has a high reflection and tends to grow in an island form at small thicknesses. Previous works have shown that proper seed layers favour nucleation of Ag films, which became continuous for thicknesses much lower than those directly deposited on the substrate's surface [27]. Oxide undercoat and overcoat layers can reduce the reflection of Ag [28]. TiO_2 is an ideal undercoat material as it has a high refractive index (high AR effect), chemical stability and nucleation seeding properties, and it promotes strong film adhesion to the substrate. AZO has been used as an overcoat layer because of its relatively low refractive index and the fact that its low conductivity ensures electrical contact between the Ag film and other materials, which is essential for the functionality of several devices incorporating the AR-TC. The AR effect in a multilayer structure relies on destructive interference between light reflected at the different interfaces. This can be understood following similar lines of consid-

eration to the ones for the multilayer perfect absorber (see Equations (4.1), (4.2) and (4.6)) which lead to amplitude and phase balance equations, given by [29]:

$$|r_{01}| = \frac{\left|t_{01}t_{10}r_{1/5}\right|}{\left|1 - r_{10}r_{1/5}e^{2i\beta_1 d_1}\right|}, \tag{5.1a}$$

$$\arg(r_{01}) = \arg(t_{01}t_{10}r_{1/5}) - \arg(1 - r_{10}r_{1/5}e^{2i\beta_1 d_1}) + 2\beta_1 d_1 + \pi\,. \tag{5.1b}$$

Maximum AR corresponds to minimum R, which can be obtained through optimisation of the film's thicknesses as, in our case, the materials are predefined. To determine the optimum thickness of each layer, the Transfer Matrix Method (TMM) was used. The TMM automatically takes into account multiple reflections of a multi-layer structure and determines the optical response of the system including the entire structure's transmission and reflection, together with absorption in each layer. In our experiments, the thickness of Ag was kept constant at a thickness (12 nm) that provides low R_s (less than 6 Ω per square), while the TiO_2 and AZO thicknesses were varied to find the optimal combination for minimum R. Figure 5.1(c), (d) and (e) show the optical simulation results with clear dependence of T, R and A on the TiO_2 and AZO thicknesses. Note that the simulated parameters include the substrate's contribution, i.e. they refer to the entire multilayer TC on the substrate structure. This means that in the case of complete AR, the simulated R would not tend to zero, but, instead, the value corresponding to the back side substrate-air interface (about 3.5%). Simulation results point out that maximum T and minimum R should be obtained for TiO_2 and AZO thicknesses in the range of 20-30nm and 30-50nm, respectively. Similar trends can be observed for Corning Eagle XG glass and Poly Ethylene Terephthalate (PET) polymer substrates which have a refractive index different from fused silica as it can be seen in Figure 5.2. Figure 5.3(a) and (b) show the experimental results of T_{AVE} and R_{AVE}, average values of T and R, respectively, over the visible wavelength range (400-700 nm), for varying thicknesses of TiO_2 and AZO. There is a strong agreement with the simulation. The optimum structures were TiO_2 (25nm)/Ag (12nm)/AZO (40nm) and TiO_2 (20nm)/Ag (12nm)/AZO (45nm), named AR-TC1 and AR-TC2, respectively (we have indicated in parenthesis the layer's thicknesses). Figure 5.3(c) and (d) show the measured wavelength dependent T and R spectra of AR-TC1 and AR-TC2, respectively, compared with bare fused SiO_2 substrate, commercial ITO (approximately 135nm thick) and single layer graphene on fused silica. T_{AVE} for the investigated AR-TC structures was as high as 91.6%, about 5%

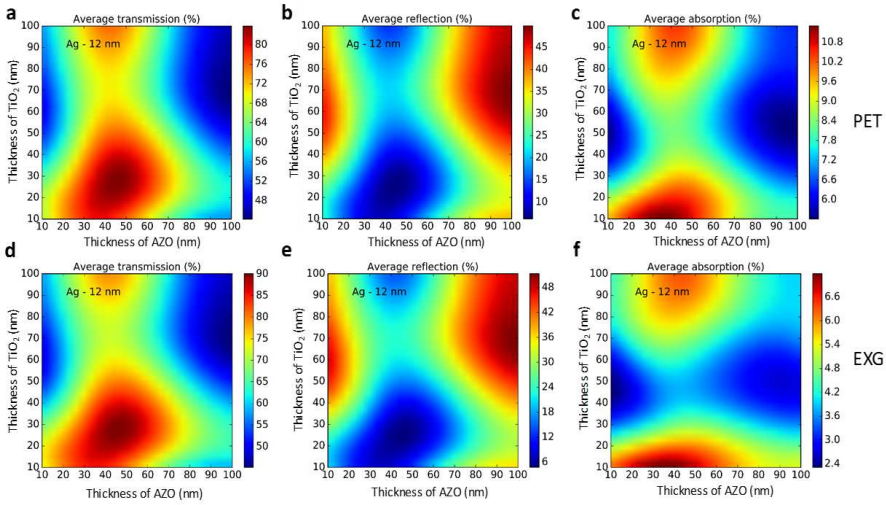

Figure 5.2: Simulated transmission (a), (d), reflection (b), (e) and absorption (c), (f) of AR-TC for different TiO_2 and Al doped ZnO (AZO) thicknesses for Poly Ethylene Terephthalate (PET) polymer and Corning Eagle XG glass substrates. For all the structures, the Ag film thickness is kept constant at 12 nm. The transmission, reflection and absorption include the substrate contribution, i.e. they refer to the whole TC on substrate structure, and are average values over 400 to 700 nm wavelength range.

greater than that of ITO (86.7%) and very close (about 1.6%) to that of the bare fused silica substrate (93.5%). Note that Figure 5.3(d) includes measurements of double sided R. In order to verify the AR quality of the proposed AR-TC, we have also measured single sided R. The Inset in Figure 5.4(b) illustrates the method of measuring it. The back R from the substrates-air interface has been suppressed by adding an absorbing substrate (black glass), index matched to the sample through an appropriate oil. The residual R from the AR-TC, with an average value of about 1% in the 400-700 nm wavelength range, is low compared to both the uncoated substrate surface (3.5%) and ITO coated surface (5%). This strong AR effect increases the value of T and reduce the OL for AR-TC compared to bare substrate to less about 1.6%, i.e. even lower than that of a single layer graphene. For a more complete assessment of the AR properties, we simulated (Figure 5.4(a)) and measured (Figure 5.4(b)) single sided R for the AR-TC1 at different angles of incidence. Figure 5.4(c) and (d) show the results for AR-

Substrate Material	Refractive index	Substrate Transmission T (%)	Total Transmission T_{TOT}	TC Transmission T_{TC}(%)	Optical Loss,OL(%)
Fused Silica	1.46	93.16	91.6	98.33	1.56
Corning Eagle XG	1.51	91.08	89.23	97.97	1.85
PET	1.65 + 1.49e-5i	85.6	82.43	96.30	3.17

Table 5.1: The reported values for all the transmission and optical loss are averaged over the visible range (400-700nm). Note that the total transmission in the table, T_{TOT}, includes both the TC (T_{TC}) and substrate (T_S). In fact we measured independently T_{TOT} (substrate with TC) and T_S (only substrate without TC) and calculated T_{TC} = T_{TOT}/T_S. The optical loss, OL, is calculated as OL = T_{TOT} - T_S. Structures for PET and EXG were not fully optimised. PET was also highly reflective (high refractive index) and slightly absorbing.

TC2 and commercial ITO samples, respectively. The superior AR behaviour of the proposed AR-TC structure is maintained up to large angles (50^o). Note that preliminary experiments performed on Corning Eagle XG and PET substrates with same layers as AR-TC1 on fused silica indicate that even for these materials optical loss is already very low and transmission of TC very high as one can see it from Table 5.1, despite the fact that the structures were not optimised.

5.3 Electrical and mechanical properties

5.3.1 Electrical properties

The R_s of all the AR-TC structures was around 5.75 Ω per square, less than half the value of the reference commercial ITO (14.01 Ω per square). This result was almost entirely due to the Ag layer. From an electrical point of view, the thicker the Ag layer, the lower the R_s. From an optical point of view, without the AR undercoat and overcoat layers, the thicker the Ag layer, the larger the R and A, i.e. the OL. However, the use of AR layers helps to contain the increase in R as the layer gets thicker. There is, thus, an optimum trade-off for the Ag thickness, which was 12 nm in our case. The RMS surface roughness of the Ag film was measured to be 2.2 nm, much smaller than when directly deposited on the fused silica substrate (6.5 nm). This confirms the importance of the undercoat TiO_2 layer in achieving a very continuous and smooth Ag film, which ensures high electrical and optical performance of the TC structures. For better comparing our AR-TC with ITO, graphene and other TCs in the literature, we used a widely

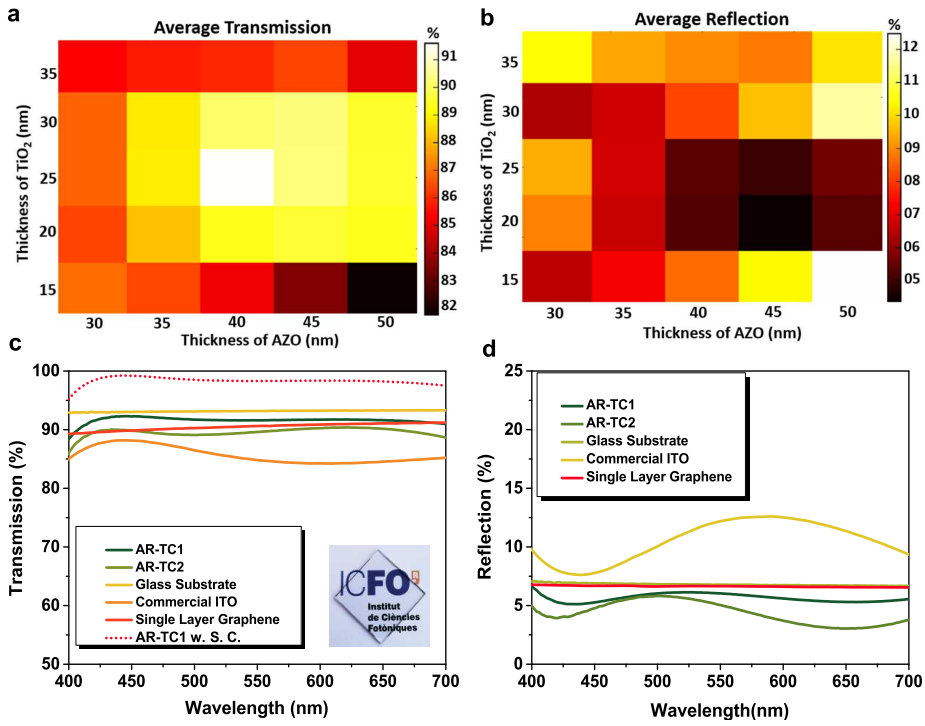

Figure 5.3: Experimental average values of transmission (a) (T_{AVE}) and reflection (b) (R_{AVE}) over the visible wavelength range (400-700 nm) of the proposed AR-TC, for varying thickness of TiO_2 and AZO (25 different samples were prepared and measured. Each square corresponds to a sample with the oxide thickness indicated). Wavelength dependent transmission (c) and reflection (d) of optimal AR-TC (AR-TC1 and AR-TC2) compared with bare fused SiO2 substrate, single layer graphene and commercial ITO. Measured values include substrate contribution and two side reflections. The dashed line in (c) corresponds to the transmission of AR-TC1 without the substrate contribution, i.e. the ratio between the AR-TC1 transmission and glass substrate transmission (continuous curves). The average TC transmission is calculated to be 98.33%.

accepted Figure of Merit (FoM= σ_{DC}/σ_{OP}) that is the ratio between direct current (DC) conductivity (σ_{DC}) and optical conductivity (σ_{OP}) which are related to T and R_s [30] as

$$T = \left(1 + \frac{188.5}{R_s}\frac{\sigma_{OP}}{\sigma_{DC}}\right)^{-2}. \tag{5.2}$$

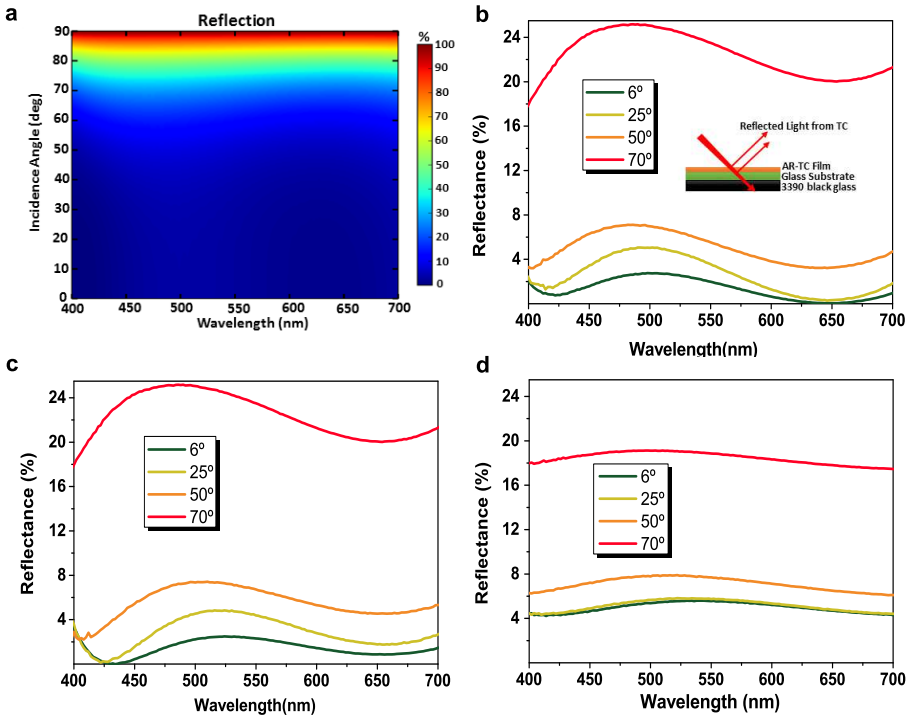

Figure 5.4: (a) Simulated angle dependent R of AR-TC 1 for varying angle of incidence. Experimental angle dependent one surface R of (b) AR-TC 1, (c) AR-TC 2 and (d) commercial ITO for incidence angles of 60, 250, 500, and 700. Inset of (b) scheme of one side reflection measurement obtained by index matching a completely absorbing material (black glass) to the back surface.

Or

$$\frac{\sigma_{DC}}{\sigma_{OP}} = \frac{188.5}{R_s(T^{-1/2}-1)}\,. \tag{5.3}$$

Note that in our estimates we considered T as the average value over the visible wavelength range (400-700nm) of the entire TC on substrate structure. Our AR-TC exhibits σ_{DC}/σ_{OP} of 730, 4 times greater than the reference commercial ITO (180) and 95 times greater than single layer graphene with relatively high doping (R_s=325 Ω per square). For a more straight comparison with other works in literature, we also used another common FoM, ie) Haacke's [31], given

References	Structure	Transmission(%) at 550 nm	Sheet resistance (Ω sq^{-1})	Haacke FoM ($\times 10^{-3}\Omega^{-1}$).	σ_{DC}/σ_{OP} FoM
our design	TiO_2/Ag/AZO	91.6	5.75	72.3	730.0
[3]	Cu_2O/Cu/Cu_2O mesh	88.1	15.1	18.6	189.0
[28]	TiO_2/Ag/ITO	88.6	6.20	48.5	497.8
[30]	Dip-coated AgNw	89.9	10.2	34.0	339.0
[32]	ZnO/AgNw/AZO/ZnO	87.3	11.3	22.8	237.5
[33]	Graphene–metallic grid hybrid	90.0	20.0	17.4	173.9
[34]	Cu nanowire	90.0	25.0	13.9	139.1
[35]	Polymer–metal hybrid	89.4	10.0	32.0	327.0
[36]	ZTO/Ag/ZTO	83.2	8.80	18.0	222.2
[37]	Capillary printed AgNW	90.4	19.4	18.8	175.1
[38]	Doped single-layer graphene	86.4	325	0.71	7.69
	Commercial ITO	86.6	14.0	16.9	180.1

Table 5.2: Table of comparison of different transparent electrode designs from literature

by

$$\Phi_{TC} = \frac{T^{10}}{R_s}\,. \tag{5.4}$$

Table5.2 shows the two FoMs (σ_{DC}/σ_{OP} and Φ_{TC}) of different TCs having high transmission reported in the literature [32–38], which is re-calculated for transmission at 550nm and includes substrate's contribution.

5.3.2 Mechanical flexibility

Mechanical flexibility is an important attribute of TCs for two main reasons. Flexible and foldable electronic/optoelectronic devices undergo strong curvature effects while low cost production requires roll-to-roll processing of large substrates coated with TCs [39]. To demonstrate the flexibility of our AR-TC, we deposited it onto Poly Ethylene Terephthalate (PET) polymeric substrates and subjected it to continuous bending. In addition, an ITO coated PET was also tested. R_s was measured at various bending radii, from 10 to 3mm. Figure 5.5(a) shows the mechanical flexibility results of the proposed AR-TC compared with the ITO. The AR-TC shows excellent flexibility due to the mechanical ductility of the Ag film while the ITO breaks due to its fragility. The corresponding change in Rs for the AR-TC structures is about 12.7% after 1000 cycles of bending with the radius of curvature between 10 and 3 mm. On the other hand, the R_s of the ITO increases by 1120% even for an order of magnitude smaller number of cycles (100).

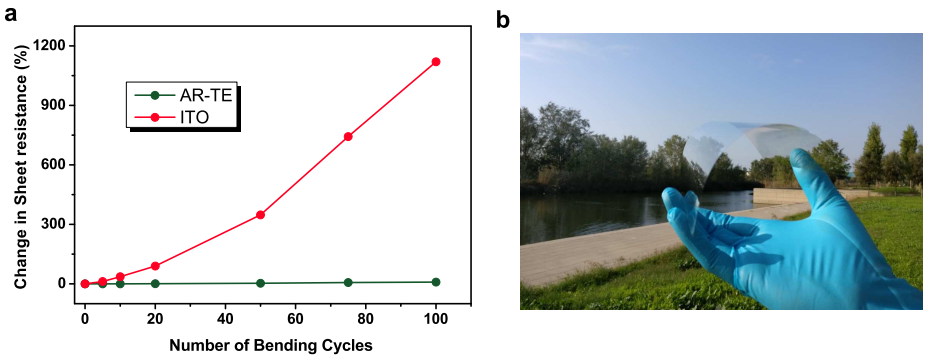

Figure 5.5: (a) Change in sheet resistance of AR-TC after bending as a function of bending cycle compared with conventional ITO. Maximum and minimum bending radii are 10 and 3 mm, respectively. (b) Real photo of bent electrode

5.4 Performance in EMI shielding applications

To assess the application potential of developed AR-TCs, we have focused on transparent EMI shielding, particularly important for display and imaging cameras. An example is the possibility to realise invisible windows that attenuate microwaves and transmit visible light. For such a window, not only are the high visible optical transmission and very low electrical resistance (high shielding effect) important, but equally crucial to achieving invisibility is the very low reflection that we have demonstrated.

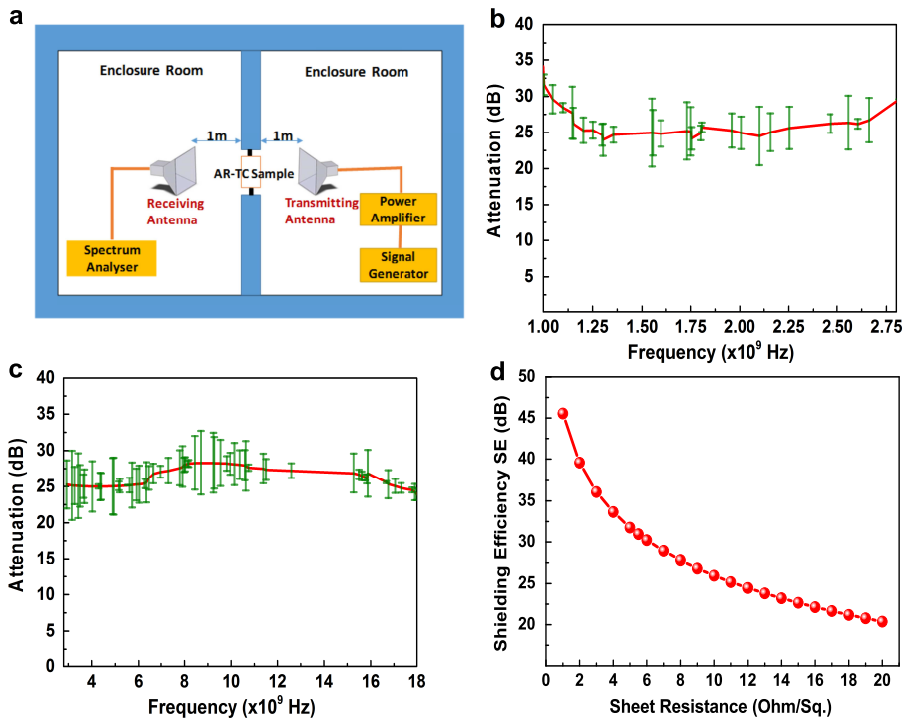

Figure 5.6: (a) Scheme of EMI shielding efficiency (SE) measurement setup with enclosure, transmitting and receiving antenna. (b), (c) SE (attenuation) for AR-TC with R_s of about 7 Ω per square in the frequency range 1GHz-2.8 GHz (b) and 2.8GHz- 18GHz (c), respectively. The error bars represent the difference between measured data and their average calculated using Fast Fourier Transform filtering. (d) SE as a function of sheet resistance R_s.

The EMI shielding efficiency (SE) quantifies the conductive coating's attenuation of electromagnetic radiation and is expressed by the ratio in decibels (dB) between the incident power (P_i) and transmitted power (P_t) $SE(dB) = 10Log(P_i/P_t)$. For example, an SE of 30dB means that the conductive coating attenuates 99.9% of the incident power. The SE of the TC structures was measured in a shielded room enclosure, so that errors due to external signals were minimized. For the measurements, a 7x7 cm AR-TC sample with R_s of about 7 Ω per square was prepared and properly located in an aluminium frame. Figure 5.6(a) shows the measurement set up. A reference measurement with Al

frame (without AR-TC) was carried out to be able to evaluate the SE of the AR-TC coated glass window only. Most of the studies of EMI shielding in literature have been carried out in the X-band (8.2 to 12.4GHz) as defence tracking, telephone microwave relay systems, weather radar, satellite communication, and TV picture transmission work in this spectral region [40]. However, extending the frequency range is often of interest, for example for modern household appliances, microwave heating, mobile phones, wireless communication equipment, and satellite navigation. The EMI shielding in our work was evaluated with Horn antenna from 1GHz-18GHz.

Figure 5.6(b) and (c) show the average SE of AR-TC from 1 GHz-2.8 GHz and 2.8 GHz- 18 GHz, respectively. It is evident from these figures that the AR-TC provides an efficient shielding in higher frequencies. An average 26.2 dB SE was measured with peak values well exceeding 33 dB. Importantly, in the widely used X band, the proposed AR-TC shows a high average SE (27.7dB). SE would be even higher for the lowest R_s samples demonstrated in this work. This is depicted in Figure 5.6(d), according to the relation:

$$SE(dB) = 20log_{10}\left(1 + \frac{Z_0}{2R_s}\right). \tag{5.5}$$

where Z_0 is the free space impedance (377 Ω) [41]. For the AR-TC structure with R_s of 5.75 Ω per square, an SE of 30.8 dB is expected. To the best of our knowledge, this is the highest SE reported for a TC with T including a substrate larger than 90%. For comparison, state-of-the-art EMI shielding with ITO provides an SE of about 25 dB with T lower than 87%. The SE of other TCs, such as carbon nanotube, graphene and conductive polymers are even lower (less than 25 dB) [42, 43]. Metal mesh can provide higher SE at the expense of transparency (visibility), as it typically has significant scattering (haze). It also presents high reflectivity, contrary to the proposed AR-TC structures.

5.5 Conclusions

Our work exploits fully the antireflection effect in optimised ultrathin metal film based transparent conductors. Through simulation and experiments, we have shown that destructive interference in a multilayer transparent conductor structure can lead to optical transmission greater than 98% in the visible, whilst still keeping very high electrical conductivity (low electrical sheet resistance of 5.75

Ω per square). The resulting optical loss is even lower than for single layer graphene and the record figure of merit is four times larger than for commercially available ITO. In addition, the proposed structure is mechanically flexible and room temperature deposited, and its performance has been tested in EMI shielding with high attenuation.

Bibliography

[1] T. Sekitani, H. Nakajima, H. Maeda, T. Fukushima, T. Aida, K. Hata, and T. Someya, "Stretchable active-matrix organic light-emitting diode display using printable elastic conductors." *Nature materials*, vol. 8, no. 6, pp. 494–499, 2009.

[2] M. S. Lee, K. Lee, S. Y. Kim, H. Lee, J. Park, K. H. Choi, H. K. Kim, D. G. Kim, D. Y. Lee, S. Nam, and J. U. Park, "High-performance, transparent, and stretchable electrodes using graphene-metal nanowire hybrid structures," *Nano Letters*, vol. 13, no. 6, pp. 2814–2821, 2013.

[3] D.-J. Kim, H.-J. Kim, K.-W. Seo, K.-H. Kim, T.-W. Kim, and H.-K. Kim, "Indium-free, highly transparent, flexible Cu2O/Cu/Cu2O mesh electrodes for flexible touch screen panels," *Scientific Reports*, vol. 5, p. 16838, nov 2015.

[4] S. Hong, H. Lee, J. Lee, J. Kwon, S. Han, Y. D. Suh, H. Cho, J. Shin, J. Yeo, and S. H. Ko, "Highly Stretchable and Transparent Metal Nanowire Heater for Wearable Electronics Applications," *Advanced Materials*, vol. 27, no. 32, pp. 4744–4751, 2015.

[5] G. Zhao, W. Wang, T.-S. Bae, S.-G. Lee, C. Mun, S. Lee, H. Yu, G.-H. Lee, M. Song, and J. Yun, "Stable ultrathin partially oxidized copper film electrode for highly efficient flexible solar cells," *Nature Communications*, vol. 6, p. 8830, 2015.

[6] S. K. Park, J. I. Han, D. G. Moon, and W. K. Kim, "Mechanical stability of externally deformed indium-tin-oxide films on polymer substrates," *Japanese Journal of Applied Physics, Part 1: Regular Papers and Short Notes and Review Papers*, vol. 42, no. 2 A, pp. 623–629, 2003.

[7] D. S. Ghosh, L. Martinez, S. Giurgola, P. Vergani, and V. Pruneri, "Widely transparent electrodes based on ultrathin metals." *Optics letters*, vol. 34, no. 3, pp. 325–327, 2009.

[8] N. Formica, P. Mantilla-Perez, D. S. Ghosh, D. Janner, T. L. Chen, M. Huang, S. Garner, J. Martorell, and V. Pruneri, "An indium tin oxide-free polymer solar cell on flexible glass," *ACS Applied Materials and Interfaces*, vol. 7, no. 8, pp. 4541–4548, 2015.

[9] Q. Xu, T. Song, W. Cui, Y. Liu, W. Xu, S. T. Lee, and B. Sun, "Solution-processed highly conductive pedot:pss/AgNE/GO transparent film for efficient organic-Si hybrid solar cells," *ACS Applied Materials and Interfaces*, vol. 7, no. 5, pp. 3272–3279, 2015.

[10] C. Preston, Z. Fang, J. Murray, H. Zhu, J. Dai, J. N. Munday, and L. Hu, "Silver nanowire transparent conducting paper-based electrode with high optical haze," *J. Mater. Chem. C*, vol. 2, no. 7, pp. 1248–1254, 2014.

[11] T. Kim, Y. W. Kim, H. S. Lee, H. Kim, W. S. Yang, and K. S. Suh, "Uniformly interconnected silver-nanowire networks for transparent film heaters," *Advanced Functional Materials*, vol. 23, no. 10, pp. 1250–1255, 2013.

[12] J. Kim, W. J. da Silva, A. R. Bin Mohd Yusoff, and J. Jang, "Organic devices based on nickel nanowires transparent electrode." *Scientific reports*, vol. 6, p. 19813, 2016.

[13] A. R. Rathmell and B. J. Wiley, "The synthesis and coating of long, thin copper nanowires to make flexible, transparent conducting films on plastic substrates," *Advanced Materials*, vol. 23, no. 41, pp. 4798–4803, 2011.

[14] Z. Wu, Z. Chen, X. Du, J. M. Logan, J. Sippel, M. Nikolou, K. Kamaras, J. R. Reynolds, D. B. Tanner, A. F. Hebard, and A. G. Rinzler, "Transparent, conductive carbon nanotube films." *Science (New York, N.Y.)*, vol. 305, no. 5688, pp. 1273–6, 2004.

[15] A. D. Pasquier, H. E. Unalan, A. Kanwal, S. Miller, and M. Chhowalla, "Conducting and transparent single-wall carbon nanotube electrodes for polymer-fullerene solar cells," *Applied Physics Letters*, vol. 87, no. 20, pp. 1–3, 2005.

[16] C. F. Guo, T. Sun, Q. Liu, Z. Suo, and Z. Ren, "Highly stretchable and transparent nanomesh electrodes made by grain boundary lithography," *Nature Communications*, vol. 5, p. 3121, 2014.

[17] R. Chen, S. R. Das, C. Jeong, M. R. Khan, D. B. Janes, and M. A. Alam, "Co-percolating graphene-wrapped silver nanowire network for high performance, highly stable, transparent conducting electrodes," *Advanced Functional Materials*, vol. 23, no. 41, pp. 5150–5158, 2013.

[18] X. Wan, G. Long, L. Huang, and Y. Chen, "Graphene - A promising material for organic photovoltaic cells," *Advanced Materials*, vol. 23, no. 45, pp. 5342–5358, 2011.

[19] S. Bae, H. Kim, Y. Lee, X. Xu, J.-S. Park, Y. Zheng, J. Balakrishnan, T. Lei, H. Ri Kim, Y. I. Song, Y.-J. Kim, K. S. Kim, B. Özyilmaz, J.-H. Ahn, B. H. Hong, and S. Iijima, "Roll-to-roll production of 30-inch graphene films for transparent electrodes," *Nature Nanotechnology*, vol. 5, no. 8, pp. 574–578, 2010.

[20] X. Y. Zeng, Q. K. Zhang, R. M. Yu, and C. Z. Lu, "A new transparent conductor: Silver nanowire film buried at the surface of a transparent polymer," *Advanced Materials*, vol. 22, no. 40, pp. 4484–4488, 2010.

[21] E. C. Garnett, W. Cai, J. J. Cha, F. Mahmood, S. T. Connor, M. Greyson Christoforo, Y. Cui, M. D. McGehee, and M. L. Brongersma, "Self-limited plasmonic welding of silver nanowire junctions." *Nature materials*, vol. 11, no. 3, pp. 241–9, 2012.

[22] N. P. Sergeant, A. Hadipour, B. Niesen, D. Cheyns, P. Heremans, P. Peumans, and B. P. Rand, "Design of transparent anodes for resonant cavity enhanced light harvesting in organic solar cells," *Advanced Materials*, vol. 24, no. 6, pp. 728–732, 2012.

[23] D. S. Ghosh, T. L. Chen, V. Mkhitaryan, and V. Pruneri, "Ultrathin transparent conductive polyimide foil embedding silver nanowires," *ACS Applied Materials and Interfaces*, vol. 6, no. 23, pp. 20 943–20 948, 2014.

[24] K. Ellmer, "Past achievements and future challenges in the development of optically transparent electrodes," *Nature Photonics*, vol. 6, no. 12, pp. 808–816, 2012.

[25] D. S. Ghosh, T. L. Chen, N. Formica, J. Hwang, I. Bruder, and V. Pruneri, "High figure-of-merit Ag/Al:ZnO nano-thick transparent electrodes for indium-free flexible photovoltaics," *Solar Energy Materials and Solar Cells*, vol. 107, pp. 338–343, 2012.

[26] H.-J. Lee, J.-W. Kang, S.-H. Hong, S.-H. Song, and S.-J. Park, "MgxZn1–xO/Ag/MgxZn1–xO Multilayers As High-Performance Transparent Conductive Electrodes," *ACS Applied Materials & Interfaces*, vol. 8, no. 3, pp. 1565–1570, jan 2016.

[27] N. Formica, D. S. Ghosh, A. Carrilero, T. L. Chen, R. E. Simpson, and V. Pruneri, "Ultrastable and atomically smooth ultrathin silver films grown on a copper seed layer," *ACS Applied Materials and Interfaces*, vol. 5, no. 8, pp. 3048–3053, 2013.

[28] D. S. Ghosh, Q. Liu, P. Mantilla, T. Chen, V. Mkhitaryan, M. Huang, S. Garner, J. Martorell, and V. Pruneri, "Highly flexible transparent electrodes containing ultrathin silver for efficient polymer solar cells," *Advanced functional materials*, vol. 25, no. 47, pp. 7309–7316, 2015.

[29] M. S. Tomaš, "Recursion relations for generalized Fresnel coefficients: Casimir force in a planar cavity," *Physical Review A - Atomic, Molecular, and Optical Physics*, vol. 81, no. 4, 2010.

[30] S. B. Sepulveda-Mora and S. G. Cloutier, "Figures of merit for high-performance transparent electrodes using dip-coated silver nanowire networks," *Journal of Nanomaterials*, vol. 2012, 2012.

[31] G. Haacke, "New figure of merit for transparent conductors," *Journal of Applied Physics*, vol. 47, no. 9, pp. 4086–4089, 1976.

[32] A. Kim, Y. Won, K. Woo, S. Jeong, and J. Moon, "All-solution-processed indium-free transparent composite electrodes based on Ag nanowire and metal oxide for thin-film solar cells," *Advanced Functional Materials*, vol. 24, no. 17, pp. 2462–2471, 2014.

[33] Y. Zhu, Z. Sun, Z. Yan, Z. Jin, and J. M. Tour, "Rational design of hybrid graphene films for high-performance transparent electrodes," *ACS Nano*, vol. 5, no. 8, pp. 6472–6479, 2011.

[34] T. He, A. Xie, D. H. Reneker, and Y. Zhu, "A tough and high-performance transparent electrode from a scalable and transfer-free method," *ACS Nano*, vol. 8, no. 5, pp. 4782–4789, 2014.

[35] H. Kang, S. Jung, S. Jeong, G. Kim, and K. Lee, "Polymer-metal hybrid transparent electrodes for flexible electronics." *Nature communications*, vol. 6, p. 6503, 2015.

[36] T. Winkler, H. Schmidt, H. Flügge, F. Nikolayzik, I. Baumann, S. Schmale, T. Weimann, P. Hinze, H. H. Johannes, T. Rabe, S. Hamwi, T. Riedl, and W. Kowalsky, "Efficient large area semitransparent organic solar cells based on highly transparent and conductive ZTO/Ag/ZTO multilayer top electrodes," *Organic Electronics: physics, materials, applications*, vol. 12, no. 10, pp. 1612–1618, 2011.

[37] S. Kang, T. Kim, S. Cho, Y. Lee, A. Choe, B. Walker, S. J. Ko, J. Y. Kim, and H. Ko, "Capillary printing of highly aligned silver nanowire transparent electrodes for high-performance optoelectronic devices," *Nano Letters*, vol. 15, no. 12, pp. 7933–7942, 2015.

[38] Z. Liu, J. Li, Z.-H. Sun, G. Tai, S.-P. Lau, and F. Yan, "The application of highly doped single-layer graphene as the top electrodes of semitransparent organic solar cells." *ACS nano*, vol. 6, no. 1, pp. 810–8, 2012.

[39] S. R. Forrest, "The path to ubiquitous and low-cost organic electronic appliances on plastic." *Nature*, vol. 428, no. 6986, pp. 911–918, 2004.

[40] D. C. T. S. Geetha, K. K. Satheesh Kumar, Chepuri R. K. Rao, M. Vijayan, "EMI Shielding: Methods and Materials—A Review," *Journal of Applied Polymer Science*, vol. 113, no. 1, pp. 2073–2086, 2009.

[41] N. Colaneri and L. Schacklette, "EMI shielding measurements of conductive polymer blends," *IEEE Transactions on Instrumentation and Measurement*, vol. 41, no. 2, pp. 291–297, 1992.

[42] Z. Chen, C. Xu, C. Ma, W. Ren, and H. M. Cheng, "Lightweight and flexible graphene foam composites for high-performance electromagnetic interference shielding," *Advanced Materials*, vol. 25, no. 9, pp. 1296–1300, 2013.

[43] B. Shen, W. Zhai, and W. Zheng, "Ultrathin flexible graphene film: An excellent thermal conducting material with efficient EMI shielding," *Advanced Functional Materials*, vol. 24, no. 28, pp. 4542–4548, 2014.

Chapter 6

Conclusions and Outlook

A wide range of photonic devices include optical surfaces based on periodic nanostructures and thin dielectric multilayers. The thesis has devised a novel mathematical description to model the interaction of light with these types of surface. This has in turn allowed proposing new designs. In particular, we have investigated hybrid combinations of 2D periodic structures or multilayer thin films with PCMs for enhanced tunability of resonant devices, including an optical tunable filter with ultrafast response, a perfect absorber with large dynamic range and a transparent electrode with record trade-off between electrical resistance and optical transmission.

In Chapter 2, we first introduced a fully analytical, theoretical description for describing the optical properties of 2D periodic arrays of scattering dipoles. We demonstrated, how the presented theory allows one to investigate deeper the physics of scattering from a periodic surface nanostructure, explaining the physical origins of the resonance response, in contrast to fully numerical methods like FEM or FDTD, which normally use time consuming parametric sweep simulations. The proposed theory was used to explain the optical properties of the first device, a tunable optical filter, studied in the thesis, presented in Chapter 3. The optical surface structure consisted in the combination of GST and NH arrays in thin gold films, which exhibit resonances in the transmission spectrum. Upon an amorphous to crystalline phase transition of the GST film covering the NH array, large wavelength shifts (385 nm) and modulation depths (¿ 60 %) of such resonances are demonstrated. The ultrafast response was also investigated using a pump-probe set-up, showing that the resonances can be reversibly modulated

(¿30 %) on the ps timescale, without the need of a phase transition. The origin of this fast modulation is an ultrafast change in the electronic polarisability of the GST upon excitation with short pulses (80 fs). As the absence of a phase transition extends the lifetime of the device, this approach is particularly interesting for applications that require a large number of cycles. Another configuration, with GST only on top of the Au film, was also explored, which showed smaller shifts (35 nm) but could be electrically controlled using Au electrodes. Both of these configurations had broad resonances, of the order of hundreds of nm, whereas, for certain applications, narrower resonances, a few tens of nm are required. Tuning of about 13 nm of these narrower resonances was demonstrated in a third device, fabricated using e-beam lithography on top of an Si_3N_4 membrane.

A perfect absorber based on a few layered thin films, with GST as a functional layer, was described in Chapter 4. The understanding of interference effects in the layered structures allowed designing perfect absorbers of different types, one broadband (in the wavelength range 400-800nm) and another one narrowband (in NIR). Both absorbers had a simple structure made of alternating layers, with the GST layer separated from the mirror by a SiO2 layer and a capping layer on top of GST. The use of the GST as a functional layer allowed us to tune the optical response. We demonstrated about 20% absorption contrast in the broadband case, and complete switching from resonant absorption to total reflection in the NIR upon crystallization of GST. It is worth emphasizing that the thin films structure makes the fabrication very simple and applicable to large scale production, in contrast to absorbers based on metamaterials or other nanostructures requiring complicated and expensive lithography techniques.

Finally, in Chapter 5, we demonstrated an antireflective, transparent electrode design with world record performance. An appropriate control of interference effects in a straightforward substrate/TiO_2/Ag/AZO layered structure could suppress reflection from the top surface, resulting in a high transmission trough the layers. The designed interference effects allowed us to introduce thick layers of silver, providing higher electrical conductivity, still maintain very high level of optical transparency. The demonstrated transparent electrode is a serious competitor to widely used ITO, a brittle, high temperature processed and expensive oxide: (i) it has better figure of merit (product of conductivity and transparency); (ii) it is room temperature processed; (iii) it is mechanically flexible; (iv) it is made of inexpensive raw materials.

The modelling and design tools developed in the Thesis can be applied to

almost any type of optical surface with nanostructures and thin films. On the one hand, they can be used to improve the performance of the devices already demonstrated in the thesis. For example, achieve larger tenability for the narrowband optical filter and perfect absorber and extend the transmission of the multilayer electrode into the infrared wavelength region. On the other hand, new functionalities can be implemented which could lead to disruptive applications. Imagine a screen, like a glass window, that allows laser projection and at the same time is transparent to our eye. This may be achieved by designing a nano-structured optical surface with multiple narrow band scattering centred at the specific red, green and blue wavelengths needed for creating an image, while still leaving all the other wavelengths pass through unaltered.

Appendix A

Lattice sums

Lattice sums calculations are here done in a similar manner as in the reference papers [1,2] for electric dipole lattice sums, which was later generalised by [3] to include magnetic dipole lattice sums. Both of these calculations are based on the methods developed by Ewald [4, 5] and later by Kambe [6, 7] in the context of electron scattering theories. As an example, Pendry applied the methods developed by Kambe for the simulation of low energy electron diffraction (LEED) [8].

The lattice sums are given via formula (2.30), where as we see from (2.22) the generalized GF can be represented as

$$\overleftrightarrow{\mathcal{G}}^0(\mathbf{r}-\mathbf{r}') = \mathcal{D}\big(g(\mathbf{r}-\mathbf{r}')\big)\,. \tag{A.1}$$

Here $\mathcal{D}$ is a differential operator with elements

$$\mathcal{D}_{11} = \mathcal{D}_{22} = (\hat{\mathbf{I}}k^2 + \nabla\otimes\nabla), \quad \mathcal{D}_{12} = -\mathcal{D}_{21} = ik(\hat{\mathbf{I}}\times\nabla)\,. \tag{A.2}$$

This allows us to formally represent the lattice sums as

$$\mathbf{G}^{\neq}(\mathbf{k}_\parallel,\omega) = \lim_{\mathbf{r}\to 0}\left(\mathcal{D}S'(\mathbf{r},\mathbf{k}_\parallel,\omega)\right)\,, \tag{A.3}$$

where

$$S'(\mathbf{r},\mathbf{k}_\parallel,\omega) = \sum_{(m,n)\neq(0,0)} \frac{e^{ik|\mathbf{r}-\mathbf{R}_{mn}|}}{|\mathbf{r}-\mathbf{R}_{mn}|} e^{i\mathbf{k}_\parallel\mathbf{R}_{mn}}. \tag{A.4}$$

Here the singular term $(0,0)$ is omitted. We can add and subtract this term again

to write

$$S'(\mathbf{r},\mathbf{k}_\parallel,\omega)=\sum_{m,n}\frac{e^{ik|\mathbf{r}-\mathbf{R}_{mn}|}}{|\mathbf{r}-\mathbf{R}_{mn}|}e^{i\mathbf{k}_\parallel\mathbf{R}_{mn}}-\frac{e^{ikr}}{r}=S(\mathbf{r},\mathbf{k}_\parallel,\omega)-\frac{e^{ikr}}{r}\,, \quad \text{(A.5)}$$

where

$$S(\mathbf{r},\mathbf{k}_\parallel,\omega)=\sum_{m,n}\frac{e^{ik|\mathbf{r}-\mathbf{R}_{mn}|}}{|\mathbf{r}-\mathbf{R}_{mn}|}e^{i\mathbf{k}_\parallel\mathbf{R}_{mn}}\,. \quad \text{(A.6)}$$

At this point, we can use the Ewald's method to split this sum into two terms one representing the summation over direct lattice vectors and the other over reciprocal lattice vectors, both being exponentially convergent sums. We give next the final expressions for sums and refer the reader to reference [1] for details of the derivations:

$$S'(\mathbf{r},\mathbf{k}_\parallel,\omega)=S_1+S_2+S_s\,, \quad \text{(A.7)}$$

where

$$S_1=\sum_{m,n}e^{i\mathbf{k}_\parallel\mathbf{R}_{mn}}\sum_{s=\pm}\frac{e^{isk|\mathbf{r}-\mathbf{R}_{mn}|}}{2\,|\mathbf{r}-\mathbf{R}_{mn}|}\mathrm{erfc}\left(|\mathbf{r}-\mathbf{R}_{mn}|\,\eta+s\frac{ik}{2\eta}\right), \quad \text{(A.8)}$$

$$S_2=\frac{2\pi i}{A}\sum_{\mathbf{g}}e^{i(\mathbf{g}+\mathbf{k}_\parallel)\mathbf{R}}\sum_{s=\pm}\frac{e^{isk_{zg}z}}{2k_{zg}}\mathrm{erfc}\left(-s\eta\,|z|-\frac{ik_{zg}}{2\eta}\right), \quad \text{(A.9)}$$

$$S_s=-\frac{e^{ikr}}{2r}\mathrm{erfc}\left(-r\eta-\frac{ik}{2\eta}\right)+\frac{e^{-ikr}}{2r}\mathrm{erfc}\left(r\eta-\frac{ik}{2\eta}\right). \quad \text{(A.10)}$$

Finally, one can apply derivatives and take the limit $r\to 0$ to get the lattice sums for the dyadic green functions.

Appendix B

Mie coeficients of spherical particle

In 1908, Gustav Mie published a famous paper on the simulation of the colour effects associated with colloidal gold particles [9]. In his paper he gave a first outline of how to compute light scattering by small spherical particles using Maxwell's electromagnetic theory. The exact solution to scattering of an electromagnetic plane wave by a coated sphere was obtained in terms of an infinite series of partial wave contributions by Aden and Kerker in 1951 [10]. Here we give the main results of the theory and refer the readers to two well-known text books for further details on the computation [11, 12]. The key parameters for these calculations are the Mie Coefficients a_n and b_n, which allows us to compute the amplitudes of the scattered field, and c_n and d_n for the internal field, respectively. For a single spherical particle of radius a, dielectric function ε_p and μ_p in a homogeneous medium with respective permittivity and permeability ε_h

and μ_h, these coefficients are given by:

$$a_n = \frac{\mu_h m^2 j_n(mx)\psi'(x) - \mu_p j_n(x)\psi'(mx)}{\mu_h m^2 j_n(mx)\xi'(x) - \mu_p h_n^{(1)}(x)\psi'(mx)}, \tag{B.1a}$$

$$b_n = \frac{\mu_p j_n(mx)\psi'(x) - \mu_h j_n(x)\psi'(mx)}{\mu_p j_n(mx)\xi'(x) - \mu_h h_n^{(1)}(x)\psi'(mx)}, \tag{B.1b}$$

$$c_n = \frac{\mu_p j_n(x)\xi'(x) - \mu_p h_n^{(1)}(x)\psi'(x)}{\mu_p j_n(mx)\xi'(x) - \mu_h h_n^{(1)}(x)\psi'(mx)}, \tag{B.1c}$$

$$d_n = \frac{\mu_p m j_n(x)\xi'(x) - \mu_p m h_n^{(1)}(x)\psi'(x)}{\mu_h m^2 j_n(mx)\xi'(x) - \mu_p h_n^{(1)}(x)\psi'(mx)}\,. \tag{B.1d}$$

where $m = \sqrt{\varepsilon_p\mu_p}/\sqrt{\varepsilon_h\mu_h}$, $x = ka$ and $k = 2\pi/\lambda$ is the free-space light wavevector. Here, $\psi_n(x) = xj_n(x)$ and $\xi_n(x) = xh_n^{(1)}(x)$ are the so called Ricatti-Bessel functions and the primed ones are the first order derivative of these functions. If now the sphere is coated by a shell of dielectric function ε_c, magnetic permeability μ_c and outer radius b, then the Mie expansion coefficients in the host region can be written again analytically as:

$$a_n = \frac{(\tilde{D}_n/m_2 + n/y)\psi_n(y) - \psi_{n-1}(y)}{(\tilde{D}_n/m_2 + n/y)\xi_n(y) - \xi_{n-1}(y)}, \tag{B.2a}$$

$$b_n = \frac{(m_2\tilde{G}_n + n/y)\psi_n(y) - \psi_{n-1}}{(m_2\tilde{G}_n + n/y)\xi_n(y) - \xi_{n-1}}\,, \tag{B.2b}$$

where

$$\tilde{D}_n = \frac{D_n(m_2y) - A_n\chi_n'(m_2y)/\psi_n(m_2y)}{1 - A_n\chi_n(m_2y)/\psi_n(m_2y)}, \tag{B.3a}$$

$$\tilde{G}_n = \frac{D_n(m_2y) - B_n\chi_n'(m_2y)/\psi_n(m_2y)}{1 - B_n\chi_n(m_2y)/\psi_n(m_2y)}\,, \tag{B.3b}$$

and

$$A_n = \psi_n(m_2x)\frac{mD_n(m_1x) - D_n(m_2x)}{mD_n(m_1x)\chi_n(m_2x) - \chi_n'(m_2x)}\,, \tag{B.4a}$$

$$B_n = \psi_n(m_2x)\frac{D_n(m_1x)/m - D_n(m_2x)}{D_n(m_1x)\chi_n(m_2x)/m - \chi_n'(m_2x)}\,. \tag{B.4b}$$

Here $y = kb$, $m_2 = \sqrt{\varepsilon_c \mu_c}/\sqrt{\varepsilon_h \mu_h}$, $m_1 = \sqrt{\varepsilon_p \mu_p}/\sqrt{\varepsilon_h \mu_h}$ and now $m = m_2/m_1$. Also $\chi(z) = -xy_n(x)$ is the Ricatti-Bessel function of third kind. Incidentally, there have been several proposals for effective numerical calculations of these functions as well as coefficients that help avoiding numerical instabilities (see for example the discussions in [11]).

Bibliography

[1] G. Poppe, C. Wijers, and A. Van Silfhout, "Ir spectroscopy of co physisorbed on nacl (100): Microscopic treatment," *Physical Review B*, vol. 44, no. 15, p. 7917, 1991.

[2] C. Wijers and G. Poppe, "Microscopic treatment of the angular dependence of surface induced optical anisotropy," *Physical Review B*, vol. 46, no. 12, p. 7605, 1992.

[3] P. Lunnemann, I. Sersic, and A. F. Koenderink, "Optical properties of two-dimensional magnetoelectric point scattering lattices," *Physical Review B*, vol. 88, no. 24, p. 245109, 2013.

[4] P. P. Ewald, "Ewald summation," *Ann. Phys.*, vol. 64, pp. 253–371, 1921.

[5] P. Ewald, "Die berechnung optischer und elektrostatischer gitterpotentiale," *Annalen der Physik*, vol. 369, no. 3, pp. 253–287, 1921.

[6] K. Kambe, "Theory of low-energy electron diffraction. i. application of the cellular method of monatomic layers," *Zeitschrift Naturforschung Teil A*, vol. 22, p. 322, 1967.

[7] ——, "Theory if low-energy electron diffraction. 2. cellular method for complex monolayers and multilayers," *Zeitschrift Naturforschung Teil A*, no. 9, p. 1280, 1968.

[8] J. Pendry, *Low Energy Electron Diffraction: the Theoryand its Application to Determination of Surface Structure*. Academic Press, London and New York, 1974.

[9] G. Mie, "Beiträge zur optik trüber medien, speziell kolloidaler metallösungen," *Annalen der physik*, vol. 330, no. 3, pp. 377–445, 1908.

[10] A. L. Aden and M. Kerker, "Scattering of electromagnetic waves from two concentric spheres," *Journal of Applied Physics*, vol. 22, no. 10, pp. 1242–1246, 1951.

[11] C. F. Bohren and D. R. Huffman, *Absorption and scattering of light by small particles*. John Wiley & Sons, 2008.

[12] M. Kerker, *The scattering of light and other electromagnetic radiation: physical chemistry: a series of monographs*. Academic press, 2013, vol. 16.